Fall 2022

Towards Modeling of Induction Welding of Thermoplastic Laminates With a Mixed Finite Element Boundary Element Approach

Florentius Johannes van Zanten

Towards Modeling of Induction Welding of Thermoplastic Laminates With a Mixed Finite Element Boundary Element Approach

by

Florentius Johannes van Zanten

Bachelor of Science
Delft University of Technology, 2015

Master of Science
Delft University of Technology, 2018

Submitted in Partial Fulfillment of the Requirements

for the Degree of Doctor of Philosophy in

Mechanical Engineering

College of Engineering & Computing

University of South Carolina

2022

Accepted by:

Paul Ziehl, Major Professor

Michel van Tooren, Committee Member

Darun Barazanchy, Committee Member

Wout De Backer, Committee Member

Maarten Labordus, Committee Member

Yinchao Chen, Committee Member

Tracey L. Weldon, Vice Provost and Dean of the Graduate School

Acknowledgments

I would like to thank my doctoral committee for their help in the creation of this dissertation. In particular, my appreciation goes to both Dr. van Tooren and Dr. Barazanchy for their supervision. Dr. Chen for his input on the electromagnetic portion of this dissertation, and Mr. Labordus for his practical view on this very theoretical document. I would especially like to thank Dr. De Backer for his plentiful feedback and aid throughout the process, the ice-cream breaks, and the grill and bitterballen nights.

I would like to thank my friends and colleagues for their support and kindness. Dr. Sacco for discussing various theories with me. Dr. Dekker for always looking on the bright side and keeping me grounded. Mr. Spaargaren, whose drive to improve himself and dedication inspires me. I'm grateful to Mr. Mohan for his parallel efforts in both the office and the gym.

I'd like to acknowledge my family for their support. My dad, Hans van Zanten, for his daily reminders that there is more to this world than research and his patience. My brother Joep van Zanten for his discussions on math, his encouragement, and general awesomeness. My wife, Ziamara Wilson, for her patience and for providing drive to see things through.

Finally, I'd like to thank KvE composites, for providing data. This research was partially supported by the National Aeronautics and Space Administration (NASA) under the University Leadership Initiative program; grant number 80NSSC20M0165. Synthetic Design Synthesis of 'Thermoplastic UD Tape based, Fastener-free assemblies' for Urban Air Mobility vehicles; Atoms-to-Aircraft-to-Spacecraft. In addition,

the author would like to acknowledge the support of the SmartState™ Center for Multifunctional Materials and Structures.

Abstract

There is an increased interest in induction welding of carbon fiber reinforced thermoplastic composite laminates within the aerospace industry. Currently, optimal manufacturing process parameters (e.g., current, power, and frequency settings, coil movement speed, etc.) are determined through an experimental trial-and-error approach. To reduce the need for an experimental approach that can determine the manufacturing process parameters, which would be expensive in both time and money, accurate and computationally efficient numerical tools are desired. This research is focused on improving the existing numerical tool, WelDone, in regard to its speed and accuracy.

WelDone utilizes a hybrid element formulation that combines traditional finite element nodal values at the nodes with boundary integral equations at the boundary surfaces of the mesh. The formulation is hybrid, since the magnetic field in the conductive domain is represented with vector elements. The Biot-Savart law is used to determine the magnetic field generated by the induction coil on the boundary of the thermoplastic composite laminate. The magnetic field is related to the magnetic scalar potential through Green's function. The Green's function effectively maps the Dirichlet boundary condition resulting from the Biot-Savart law to a Neumann boundary condition, which is required to solve the weak formulation of Maxwell's equations. 'Dirichlet-to-Neumann' mapping allows the integral over the non-conductive domain, the air between coil and laminate, to be reduced to an integral over the boundary surface of the conductive domain, thereby, eliminating the need to discretize the non-conductive domain and improve computational efficiency.

This dissertation focuses on what is required to model curved panels. To this

end, 8-node hexahedral elements are introduced in the finite element part of the tool. The introduction of an 8-node hexahedral element revealed a numerical instability when applying numerical integration to the aforementioned 'Dirichlet-to-Neumann' mapping. The numerical instability occurred when numerically integrating a double surface integral containing the Green kernel and the normal derivative of the Green kernel. To cope with this numerical instability, the integration was solved, in part, analytically.

This dissertation assesses the accuracy of the model by comparing the results from the model to the results of previous sources, to, the literature, and to results found from commercial software. The individual algorithms and the implemented element are verified. When compared to the commercial software, the heating patterns are similar, however the magnitude of the ohmic losses are not the same between the two models.

For future development, the author recommends verifying the current code with real life experiments before the code is developed in other directions. If speeding up the code is the goal, a faster language can be employed or the development of a different element can be pursued.

Table of Contents

List of Tables

List of Figures

Chapter 1

Introduction

Carbon fiber reinforced thermoplastic composite materials are increasingly used in aerospace applications, which have opened the opportunity to assemble composite structures with fusion welding as opposed to mechanical fasteners and adhesives. Within the realm of fusion welding, multiple methodologies exist, as will be discussed in Chapter 2. This dissertation focuses on induction welding with the objective of increasing the accuracy and computational efficiency of the in-house developed numerical tool, WelDone, while extending its applicability to curved structures.

To successfully meet the objective, this chapter provides an introductory overview of the topics addressed in this dissertation. A brief overview of the difference between thermoset- and thermoplastic resins, and the induction welding process will be given in Section 1.1. The current state of the tool with its limitations is highlighted and the importance of addressing these limitations is discussed in Section 1.2. The research questions and technical challenges associated with this dissertation will be addressed in Section 1.3. In Section 1.4 the significance of these research questions is elaborated upon. Finally, the structure of the remainder of the dissertation will be provided in Section 1.5.

1.1 Background

The aerospace industry requires light-weight structures capable of meeting high standards when it comes to material properties, structural strength, and structural rigidity. With the development of smaller aircraft, which are expected to be operated in

high numbers, a higher production rate is required. To meet these demands, new material systems and manufacturing technologies are investigated and developed. A promising material system to meet the high production rate demand whilst providing the advantages of composite material is carbon fiber reinforced thermoplastic polymer.

Reinforced thermoset polymers are generally used in the form of prepregs (pre-impregnated fibers) in the aerospace industry. The thermoset polymer in the prepreg is partially cured to create a glassy product that is easy to handle during lay-up and has a well-controlled fiber and resin content. The downside is that the resin will continue to cure if not kept at low temperatures and even then the curing will be slowed down, not stopped. This requires cooled transport and storage of prepregs and a limited shelf life. The process of curing is a key aspect of working with thermosets: a cure cycle is needed to get from prepreg to final product, in which polymerization of the thermoset resin is completed to a level that yields chemical stability at the service temperature range. During the curing, polymer chains are extended and cross-linked, resulting in a solid material from an originally low viscosity material with a lower molecular weight. The prepreg material needs to be kept at a low temperature to inhibit the process of polymerization. During or after lay up, the curing process is started. The curing process often takes place in an oven or autoclave, which is a pressurized oven. The autoclave is key in creating high performance composites as the high heat promotes the curing reaction and the pressure introduced by autoclaves can help to reduce voids and create better physical properties than a curing cycle performed in an oven.

The alternatives to thermoset polymers are thermoplastic polymers, among which polyphenylene sulfide (PPS), is often referenced when discussing welding of thermoplastic polymers in aerospace applications. Thermoplastic polymers are glassy or semi-crystalline at room temperature and have a high viscosity at processing tem-

perature with respect to thermoset plastics prior to curing. To shape the material, the thermoplastic needs to be heated above the melting temperature which lowers the viscosity, allowing for shaping of the material. The material is then lowered in temperature at a certain cool-down rate to reform the crystalline structure of the semi-crystalline thermoplastic. Higher degrees of crystallinity increase the mechanical properties.

The differences between these materials in their properties and manufacturing processes provide advantages and disadvantages for both. Thermoset plastics often remain the polymer of choice [6]; however, a shift in research and development of primary structures and assemblies of thermoplastics is developing. To allow for out-of-autoclave processing [7] and thanks to some of the other advantages thermoplastic polymers offer, the effort of further developing thermoplastic primary structures is on the rise. Some of the additional advantages with respect to thermoset prepregs are the near infinite shelf life of thermoplastic polymers; the ease in storage and handling of the thermoplastic polymers, which reduces the cost of manufacturing and Modern advanced thermoplastic polymers, such as Polyaryletherketone (PAEK) and Polyphenylene sulfide (PPS), which also have great temperature and corrosion resistant properties, are more damage tolerant and have a significantly higher mode I interlaminar fracture toughness [8] than their thermoset counterparts. Thermoplastic polymers, unlike their thermoset counterparts, have the ability to be reformed when the thermoplastic is reheated. This opens up the ability to join different structures through fusion welding, and can eliminate the need for mechanical fasteners in structures. Fusion welding is a joining methodology which joins two substrates by locally melting the sub-parts and consolidating the melted zones of the part, to create a seamless joint and one final part. The elimination of mechanical fasteners could allow for a 20% reduction of cost and 10% weight reduction in primary aircraft structures when compared to conventional composite fastening solutions [9].

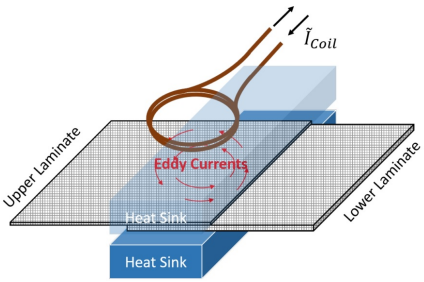

Figure 1.1: Example induction welding set-up [1]

The welding process of interest for this research is induction welding. The process of induction welding begins by placing an alternating high-power current across a conductive coil as shown in Figure 1.1. The alternating current induces an alternating electromagnetic field with the same frequency as the alternating current. When a conductive material, like a carbon fiber reinforced thermoplastic (CFRTP) is placed in this electromagnetic field and closed-loop circuits can be formed in the material, eddy currents are induced. This will be discussed in depth in Chapter 2.

The energy loss mechanism that causes the heating is joule heating. Joule heating, which is a form of heating that occurs due to the resistance of the conductor, creates a localized increase in temperature. With careful design of the coil and substrate, targeted heating of only the desired location is possible.

1.2 Current State

In this section, the aim is to introduce the in-house developed code, WelDone [1], which is based on the previous work of Bossavit [10] and on the TRIFOU method [11]. WelDone is a script in which the electromagnetic currents in a conductive domain, such as a composite laminate, can be calculated through Maxwell's equations. The non-conductive domain, the air between the coil and the laminates, does not have to be discretized when evaluating the problem in this manner. The coil is replaced by a current line which can be discretized in linear sections and the magnetic field

created quantified with the Biot-Savart law. The electromagnetic currents generate heat through Joule heating, and the heat can then be found by Joule's first law. In this code, the only element available is a cuboid element, as shown in Figure 1.2. A property of this element, in which all element edges are orthogonal, is that its geometry can be defined by only 6 variables, while retaining 8 variables in the nodes and 12 variables on the edges. These variables are employed to represent the vector and scalar field of interest, such as the magnetic field.

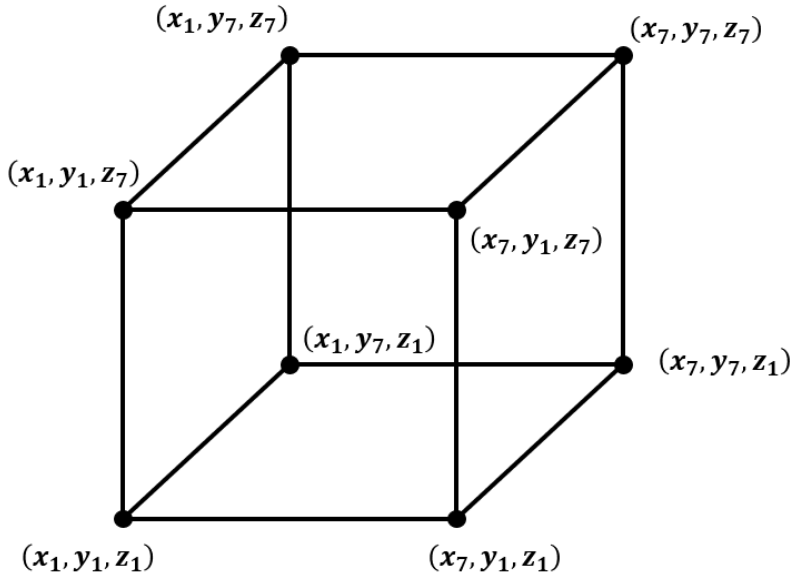

Figure 1.2: Cuboid element with 8 nodes and 12 edges, defined by 2 nodes

The element's shape and position can be defined by the 3 spatial coordinates of two nodes, which are referred to as node 1 and 7 in Figure 1.2. The advantage of this element is that the shape functions can be simplified significantly. The element is characterized by 90^o angles between the surfaces, and as such is limited in its modelling capabilities. Only cuboid shapes can be meshed and evaluated accurately. This is acceptable for research purposes, however in reality most parts are curved, and therefore more complex element shapes are necessary.

1.3 Research Questions and Technical Challenges

Modeling the process of induction welding of thermoplastic composites is a multi-parameter, multi-domain and complex challenge. The excitation frequency, current, coil shape, composite laminate stacking sequence, coil position, and speed all have an impact on the generation of heat both in location and magnitude. Currently, an experimental and iterative process is used to identify feasible welding parameters for a given welding configuration. This process is expensive in both time and cost, therefore, a numerical tool that accurately captures the physics of induction welding is beneficial to the manufacturing engineer. The research objective of this dissertation is to improve the speed and accuracy of the simulations and to mesh more complex structures by implementing a hexahedral element. The research objective can be summarized in the following research questions:

1. Which steps are required to move from cuboid elements to elements which can represent curved structures to simulate induction heating?

The goal of this question is to extend the code to model curved panels. This is achieved by replacing the cuboid element as shown in Figure 1.2 by a conventional hexahedral element as presented in Figure 1.3. The eight nodes of the hexahedral elements are defined independently and edges are not orthogonal, therefore the element can represent curved and complex geometries accurately.

Hybrid first order 8-node hexahedral elements will be implemented in the new version of the code. These elements are hybrid elements as both nodal and edge shape functions are used to quantify scalar and vector variables respectively. The new shape functions associated with the 8-node hexahedral element are implemented in the weak form of the Maxwell's equations that govern the electromagnetic problem. The implementation of the 8-node hexahedral element revealed the occurrence

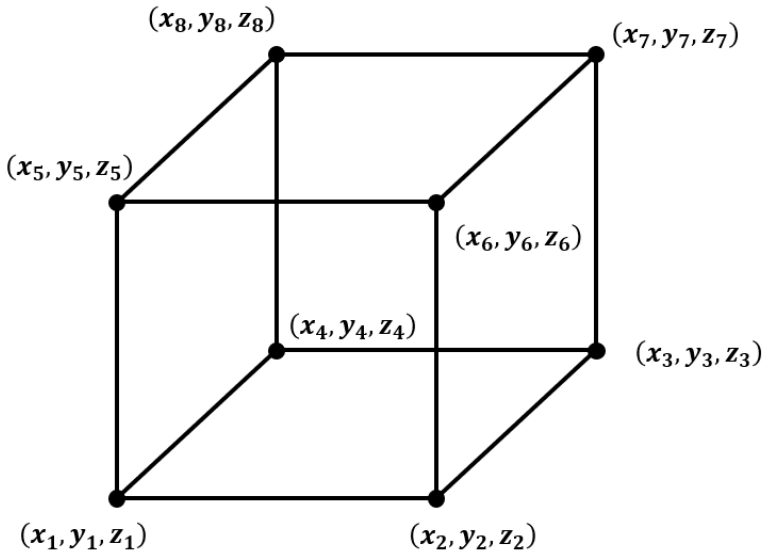

Figure 1.3: Hexahedral element with 8 nodes and 12 edges.

of a numerical singularity when considering thin composite laminates. Hence, the following research question is posed:

2. Which integration methods/approaches are required to cope with the singularity in Green's equation for the Laplace operator when applying a numerical integration to the governing equations to solve the eddy current problem?

The goal is to find an integration scheme that is precise and applicable to a laminate type model. The model has a conductive domain with 1 dimension much smaller than the other 2 dimensions.

The integration scheme of the boundary integration elements must solve Green's function for the 3-dimensional Laplace operator. This transforms the Dirichlet boundary conditions to Neumann boundary conditions. The equation is a rational function of -1 over the Euclidean norm, in essence an integration scheme must be found for an integral of the form $\int \frac{-1}{4\pi r}$. Where the Euclidean norm is: $r = \sqrt{x^2 + y^2 + z^2}$. In laminate structures, or other evaluated volumes where this norm approaches zero, a

singularity manifests itself in the term inside the integral. Taking the integral over this singularity results in a term that will tend to infinity. One could involve transformations [12] or adaptive refinements of the integration rule around the singularity [13] to handle this challenge. As this tool is aimed at being suitable for inclusion in an iterative process to allow for the optimization of the welding parameters, a logical follow-up question is:

3. Which adaptations are required to improve speed and accuracy with respect to a numerical integration solution, such that the tool can be used for an optimization problem?

To answer this question, multiple numerical and an analytical integration scheme is applied to the aforementioned Green's functions. The speed and accuracy of these methods are compared, and the best candidate is selected to be implemented in the code. What remains is the final research question:

4. How well is the developed tool able to simulate the induction welding process, and what could be done to improve the accuracy of the model?

The last question is answered by comparison of experimental results with simulated results using the new elements to simulate welding of a single lap joint between two component laminates.

1.4 Significance of the Study

In this dissertation, the aim is to pave the way for improved process simulation with the goal of finding values for the welding process variables that will lead to acceptable welds and to support optimization of laminate and coils for welding. This will significantly reduce the effort required to evaluate thermoplastic induction welded

joints. Currently, trial-and-error is often required to find the correct process parameters for thermoplastic induction welding; resources can be saved by replacing this trial-and-error methodology through simulation. This dissertation introduces the 8-node hexahedral element and solves the singularity in the Green's function for the Laplace operator to aid in modelling the induction welding process efficiently and accurately.

The results of this dissertation will aid in setting up simulations, which can help reduce the time and resources spent to get the welding parameters correct to achieve a well-connected weld. In essence, this study aims to make thermoplastic induction welding more accessible to the industry. The consequences of this research can be far-reaching.

1.5 Dissertation Outline

The outline of this dissertation follows the order of the research questions, however first, in the next chapter, Chapter 2, the state of the art of joining, induction welding and modeling is reviewed. In Chapter 3, the implementation of the 8-node hexahedral element is discussed. This includes the discussion of the assembly of the various stiffness matrices and the process that led to the discovery of the singularity in the boundary element formulation. The source of the singularities and solutions to the integrals containing the singularities are discussed in Chapter 4, these solutions are compared in accuracy in speed and the most appropriate solution is found. In Chapter 5 two induction welding cases are evaluated in WelDone and compared to COMSOL, a commercially available software package. In Chapter 6, the dissertation is concluded, the work is discussed and avenues in which the work can be improved upon is presented.

Chapter 2

State of the Art and Framework

The state of the art of joining of thermoplastic composite parts is presented in this chapter. In the first section, Section 2.1 joining technologies are introduced and discussed. In the next section, Section 2.2, induction welding is discussed, and the Maxwell's equations are presented. First, the induction welding process will be discussed and then the equations that describe the process are presented. The assumptions related to the eddy current in Maxwell's equations and the governing equations are derived in Section 2.3. In Section 2.4, the nodal based shape and edge-based shape functions of the proposed new elements are presented.

2.1 Joining Methodologies

Joining is an important process, where parts are assembled to create a structure, for instance a stringer is attached to a shell to create a stiffened skin. This process is critical to manufacturing, since the point of failure in a joined structure is often the joint. As a result, the joining method is an important consideration when designing a structure.

In this section, the different methods of joining composite structures are discussed. The three main methods of joining structures are mechanical fastening, adhesive bonding and fusion welding. Each of these joining methods have their advantages and disadvantages. In Section 2.1.1, perhaps the most well known and common method of joining is discussed: mechanical fastening. In Section 2.1.2, the principles and properties of adhesive bonding will be discussed. Finally, in Section 2.1.3, fusion

welding is discussed.

2.1.1 Mechanical Fastening

Mechanical fastening is common in various industries to join parts to form a structure, and an extensive pool of knowledge and experience to design, analyze, manufacture and repair mechanically fastened structures is available. Mechanical fasteners can be divided into two categories based on the type of fastener used, non-permanent and permanent.

The greatest strength of non-permanent fasteners is that after assembly, the structure can be disassembled and reassembled. This is especially useful when inspection is required or when a damaged portion of the structure needs to be replaced. Some of the more common non-permanent fasteners, based on bolts/screws and nut plates, lend themselves well to this purpose. Commonly used permanent fasteners are the Hi-Lok and Huck-Spin lockbolts.

This process, where the subcomponents require that holes are drilled into them, can introduce damage to the structure. Drilling a hole into the composite can cause damage to fibers and cause local weaknesses at the edge of the hole. Additionally, these holes introduce stress concentrations. The introduction of these flaws are common in mechanical fastening and one of the biggest structural disadvantages of mechanical fasteners [14].

The manner in which the fastener joins the subcomponents allows for the load transfer of both shear and perpendicular loads. In composites, four main failure types are shear failure, tensile failure, bearing failure and fastener shear. These failure types are presented in Figure 2.1 [15].

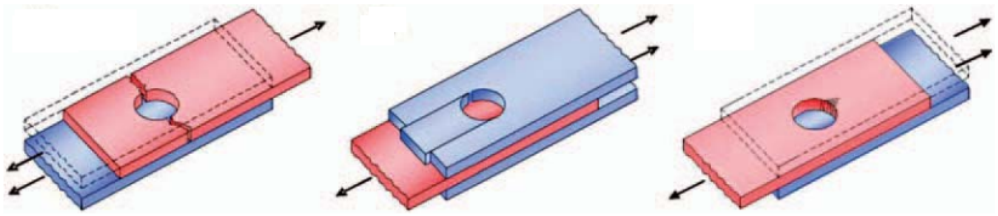

Figure 2.1: Tensile, shear and bearing failure [2]

The shear failure load P_s of the sheet can be related to the ultimate shear stress with Eqn. 2.1.1.

$$P_s = 2at\sigma_{SM} \tag{2.1.1}$$

In the above equation, the a is the distance from the hole to the edge of the laminate in the direction of the load. The t is the thickness and σ_{SM} is the ultimate shear stress of the material. The tensile failure load P_t is found through Eqn. 2.1.2.

$$P_t = t(w - d)\sigma_u K_t \tag{2.1.2}$$

With, t the thickness of the material, d is the diameter of the hole, w is the width, σ_u the ultimate tensile strength of the material, and K_t is the stress concentration factor. The bearing failure load of a joint P_b can be found through Eqn. 2.1.3 [2].

$$P_b = dt\sigma_b \tag{2.1.3}$$

In this equation, the diameter of the hole is denoted by d, t is the thickness of the load bearing subcomponent and P is the failure load. Finally, fastener shear failure load, P_f, can be found through Eqn. 2.1.4.

$$P_f = n\frac{\pi}{4}d^2\sigma_s \tag{2.1.4}$$

The variable n is the number of bolt shear planes. The ultimate shear stress is σ_s. The loads on these fasteners is dependent on the number of fasteners used to join the subcomponents. By increasing the rivet pitch and/or adding a second row of fasteners, the load experienced by the fasteners can be reduced. In this dissertation, only some insight into these failure modes is provided, as it does not pertain to the subject of the thesis. The goal is to merely highlight the complexity of the failure modes that are present in mechanical fastening.

Another effect of mechanical fasteners, with respect to the other joining methods discussed in future sections, is that the hole created for the fastener allows moisture to penetrate the laminate, making the whole structure more vulnerable to environmental degradation appropriate actions. Mechanical fasteners have the property that they scale with the thickness of the parts. As the load increases and the thicknesses of the joint parts increase, allowable loads in the joint increases as well.

Mechanical fasteners do not rely on chemical interactions and do not require immaculate surfaces and the logistics that come with keeping surfaces clean, in contrast to adhesive bonding, which is discussed in upcoming Section 2.1.2. Mechanical fastening is a tried and true way to connect two structures. However, it is a relatively high weight inducing form of joining with respect to the alternatives. In comparison to the alternatives, mechanical fastening is effective at handling loads perpendicular to the laminate, which is important to prevent peel off.

2.1.2 Adhesive Bonding

Joint performance is often characterized by lap shear performance, shown in Figure 2.2. To create this bond, three processes are available, as shown in Figure 2.3. Co-curing of thermoplastics is when both the substrates, as displayed in Figure 2.2, are cured at the same time without an adhesive. The thermoplastic equivalent is co-consolidation, which is when the thermoplastic is (re)heated and the two substrates

consolidate at the same time.

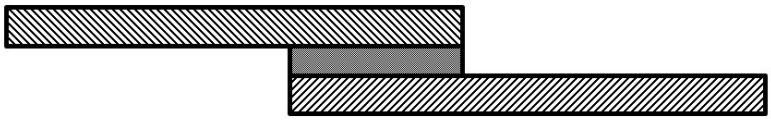

Figure 2.2: A single lap shear joint with adhesive connecting the upper and lower substrate

Both of these bonding methodologies create seamless bonds and create a single part. Co-bonding is when one of the substrates is uncured/unconsolidated and the other is cured/consolidated, careful preparation of the already cured surface is required to ensure a good bond with the adhesive. Secondary bonding is when both of the substrates are cured/consolidated laminates, and the parts bonded using a film, paste or epoxy. With co-bonding, the surface of the substrates plays a vital role in the strength of the bond.

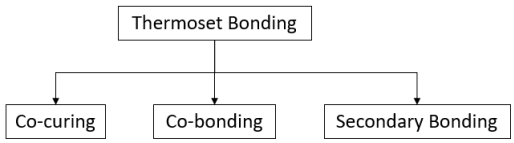

(a) Three types of bonding for thermoset plastics

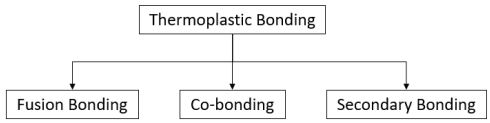

(b) Three types of bonding for thermoplastic plastics

Figure 2.3: Bonding types for plastics

Co-cured joints (without adhesive), fusion joining and secondary bonded joints generally provide a higher strength bond than co-bonded joints and co-cured joints with an adhesive [16] as no foreign material is introduced. Relations between the water content and storage humidity may seem trivial, but are vital to the strength of a bonded joint [17]. Surface preparation includes the removal of contaminants and protecting the surface, providing good surface wettability and surface energy [18, 19]. To protect the surface from contamination and maintain the desired surface textures, peel ply treatment is a popular solution [20]. The surface roughness has shown to increase the fatigue threshold strain energy release rate of the adhesive

bond [21]. Surface modifications are made to increase the surface energy, the surface energy expresses how easily a substance spreads over a surface. Increasing total surface energy results in a reduction in the contact angle and a better wettability of adherents to the substrates [18]. This highlights the importance of surface preparation and a clean environment [22]. Another parameter worth discussing is temperature. Adhesives are chemicals prone to thermal degradation. The materials of which aircraft are made are exposed to hostile environments, large changes in the temperature and high humidity environments can degrade materials rapidly. It is important for these joints to maintain their structural integrity in these environments. Adhesives tend to thermally degrade significantly as they undergo heating and cooling, making them less suitable for aerospace applications [23, 24].

Akin to mechanical fastening, the adhesive joints also introduce stress concentrations. Unlike mechanical fastening, these are not introduced due to pin loads or holes, but instead due to uneven deformation in the adherent and adhesive when the lap shear joint is loaded. The external loads are transferred by the adherent joint through shear. The deformations that introduce these stress concentrations, also known as the bath tub curve, becomes more pronounced the greater the difference in stiffness is between the substrates and the adhesive. The bath tub curve and an exaggerated deformed bond are shown in Figure 2.4. When the substrate is significantly stiffer than the adherent, which is generally true, the deformation at the extremities of the adhesive layer is larger and the stresses in the adhesive induced by that deformation are larger too.

The thickness of the adhesive layer is also an important factor, an increase in the thickness reduces the failure load [25] as this introduces peel stresses due to the eccentricity. As discussed by Silva [26], increasing the overlap length with respect to the thickness reduces the peel stresses. In addition, increasing the overlap length increases the shear load at which the adhesive fails due to the shear forces.

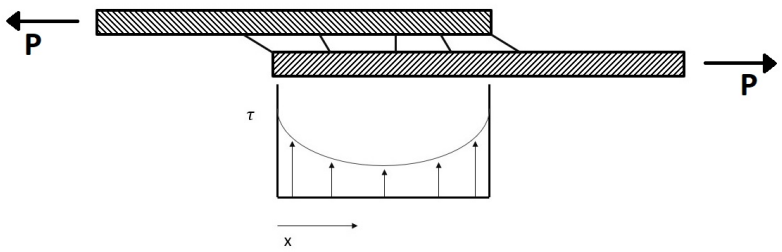

Figure 2.4: Lap shear joint loaded in shear with corresponding shear stress plot

In summary, adhesive bonding can be done, however a significant effort in creating favorable bonding conditions is required. The surface needs to be treated to remove impurities and to maximize wettability of the adherent. This requires a clean environment and specialized equipment. The upsides can be significant, the weight introduced by adhesive bonding is low and unlike mechanical fastening the bond is airtight.

2.1.3 Fusion Welding

In this research, the focus is on fusion joining the thermoplastic matrices for the purpose of joining skins through a single lap shear joint or joining a stringer to a skin. To do so, the thermoplastic matrix is heated to a temperature above the glass-transition temperature T_g or the melting point T_m for semi-crystalline thermoplastics. After heating, the thermoplastic matrix at the interface will be in a low enough viscous state, the polymer chains will intermingle and entangle, resulting in the fusion of two individual pieces. To promote contact of the interface, and thereby ensure a better bond quality, pressure is applied to the weld area. After solidification of the two components, the mechanical properties are regained [27]. Co-curing, as is done with thermoset polymers, yields similar results. During co-curing, the entirety of the parts is in an uncured, or soft, state. Whereas, in a thermoplastic material only the joint area needs to be in a viscous state that the remainder of the parts can remain

consolidated and, thus, do not require tooling or other measures to stay in their shape.

Various methods exist to fuse components. The mechanism to induce heat at the interface is used to distinguish various methods: (i) thermal welding; (ii) friction welding; and (iii) electromagnetic welding.

As the goal for this thesis work is to provide a tool for the design of aerospace joints, specifically with wing-boxes and stiffened skins in mind, the joining methodology has to include the ability to join pieces into a wing-box. The implication of this requirement is that some of the joining methodologies are unsuitable for the application sought.

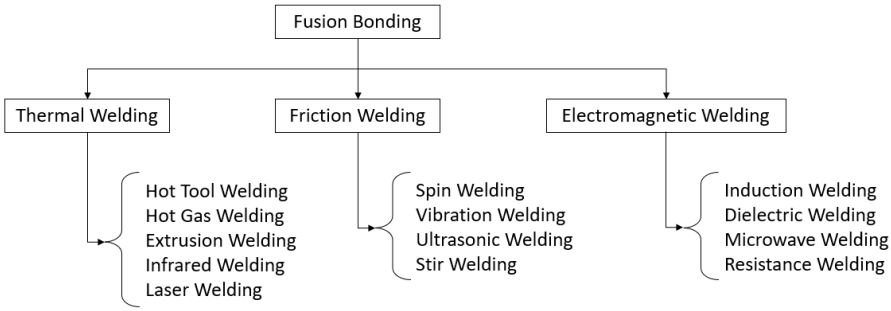

Figure 2.5: Thermal fusion welding classification

In Figure 2.5, a large selection of fusion welding methodologies is presented. From these it can be seen that the friction welding methodologies, such as ultrasonic welding, are suitable for the generation of composite joints. In thermal welding, heat is required at the interface. Therefore, welding methodologies that introduce heat on the outer surface when the interface is not accessible are suboptimal. Electromagnetic welding generates heat throughout the laminate and is able to generate heat at the desired location, giving it an edge over some other welding methods.

The quality of an induction welded joint is often compared to joints in a co-cured part or an autoclave consolidated or compression-molded structure, as the polymer chains intermingle and joint surfaces disappear, creating a seamless bond[28].

When comparing electromagnetic welding to mechanical fastening, no stress concentrations are induced by imperfections that are created due to the joining process. Induction welding is similar to adhesive bonding in the sense that it does not introduce holes or drilling induced delamination. Furthermore, fusion welding is less labor-intensive as compared to mechanical fastening and reduces the weight of the structure. Finally, the introduction of metals through a carbon fiber structure, as done with mechanical fastening, introduces the possibility of galvanic corrosion. Advantages of mechanical fastening are that the joint can be undone, and it works at very high load interactions. Mechanical fastening is a well-established fastening method that is used in multiple industries. In induction welding, difficulties remain as edge effects create local hot spots and optimization of the induction heating process remains a challenge [29].

Similar to adhesive bonding, stress concentrations are present at the edge of the induction welded overlap. However, the bond thickness is relatively small and therefore the introduced eccentricity and, by extension, the peel off stresses, are much smaller than for an adhesive bonded joint. Due to the bonding mechanism, no surface, chemicals or clean rooms are required. There is also no need for a long curing cycle when compared to thermoset plastics. The rate at which the joint is cooled does need to be taken into account, as this influences the crystallinity in the joint and directly influences the mechanical properties of the bond [30].

In induction welding, a coil generates an electromagnetic field. This field is rapidly alternated in direction by an alternating current in the coil generating the field. The alternating magnetic field induces eddy currents in a conductive material in the joint. The heat is then generated by Joule losses due to the resistance of the conductive material [31, 32]. Induction welding will be discussed in depth in Section 2.2.

In dielectric welding, the joint is sandwiched between two platens and a press applies pressure to the joint. The platens are alternatively charged positively and

negatively. The dipoles in a dipolar material will attempt to align with the electric field. By rapidly changing the electric field, the orientation of the dipolar molecules will be out of phase, causing internal molecular friction and this friction generates heat [14].

In microwave welding, the specimen is radiated at a frequency of about 2.45 GHz [14]. At this frequency, most thermoplastics are not excited. To create heat, a microwave susceptible material is inserted at the weld surface. This material will generate heat and thus allow the thermoplastic surrounding it to melt. A disadvantage is that the final product is 'contaminated' by a susceptor in the joint, which is likely to lead to fatigue and crack growth causing failure in the part [32].

Similar to microwave welding, resistance welding requires an insert in the joint interface. An electric current passes via this insert through electrical contacts. Energy is lost due to the resistance and the heat generated increases the temperature at the joint interface [14].

2.1.4 Conclusion

The importance of joining was highlighted, and the joining methods available were categorized in three different groups: mechanical fastening, adhesive bonding and fusion welding. The different joining methods and their strengths and weaknesses were discussed.

Fusion welding does not require the extensive curing period and has fewer restrictions on the manufacturing environment and surface preparation. In comparison to mechanical fastening, fusion welding creates less stress concentrations and induces fewer imperfections. Fusion welding on a wing structure can significantly reduce labor costs when compared to a bolted variant [28] while also reducing the weight of the structure.

Of the four electromagnetic welding methodologies, as shown in Figure 2.5, in-

duction welding [31, 33, 34], does not introduce any undesirable material in the joint that cannot be removed after welding. All these mean that induction welding lends itself excellently to the welding of lap joints and stringers to shell interface.

2.2 Induction Welding

The principle of induction welding relies on induction heating, the basis of induction heating was discovered in the 1830s by Michael Faraday. In 1873 James Maxwell published on electromagnetic theories [35]. In this section, the subject of induction welding will be discussed in depth. First, the history and the physical process of induction welding will be presented in Subsection 2.2.1. This will be followed by the general Maxwell's equations in Subsection 2.2.2. In section 2.3 the general Maxwell's equations will be reduced to the eddy current problem as discussed in the remainder of this thesis.

2.2.1 Physical Process

Induction welding is not a new process, and has been applied since the early 1900s [36]. Induction heating works as follows: an alternating current flows through a coil, near the workpiece that requires heating, and generates a time-variant magnetic field with the same frequency of the alternating current. This time-variant magnetic field can induce currents in an electrically conductive and magnetically susceptible material. The prerequisite is that a closed loop is available for the induced electrical current also known as eddy currents. In carbon fiber reinforced thermoplastics, the closed loops are formed by the carbon fibers. These closed loops can then heat the material through 4 different heating mechanisms: dielectric polymer heating, Joule polymer heating, dielectric hysteresis heating and contact resistance heating [31, 34].

The first heating mechanism is the heating generated by the Joule losses due to the resistance of the carbon fibers. Joule-based heating also known as resistive or ohmic

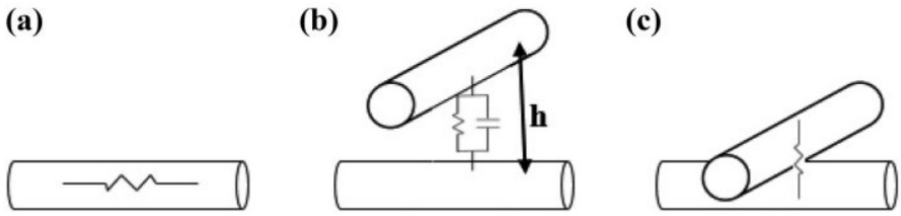

Figure 2.6: Induction heating mechanisms; (a) Joule-based fiber heating, (b) Joule and/or dielectric hysteresis polymer heating, and (c) contact resistance heating [1].

heating is caused by the energy lost as the current flows through a resistive medium, and is thus based on the resistivity of the medium. The higher the resistance, the more heat will be generated at the same current.

The remaining three heating mechanisms occur where two plies meet. 1) Joule based polymer heating, the resistive medium being the matrix that is between two fibers where the majority of the heating occurs. 2) Dielectric hysteresis heating of the polymer, where the fibers act as two sides of a capacitor and the heat is generated by the movement of the dipolar molecules in the polymer, akin to how a microwave generates heat. 3) Contact resistance heating, which is a form of Joule heating where the resistance of the contact patch between two fibers is the cause of the heat, as opposed to the resistance of the thermoplastic material. The resistance is high due to the small cross-section in which the two fibers contact[37].

Dielectric hysteresis heating is of low importance to the research as performed in this document. As the heat generated through this heating mechanism is negligible due to the low frequencies of the time-variant magnetic field used for induction welding [37], see also Appendix B.

2.2.2 Physics Foundation

The physical phenomenon of electromagnetic induction is described by Faraday's law, Maxwell-Amperes law, the Gauss' law and Gauss' law for magnetism. Faraday's law of induction, Eqn. 2.2.1, states that the line integral of the electric field around a

closed loop is opposite to the rate of change of the magnetic flux through the area enclosed by the loop. In simpler terms, Faraday's law of induction describes the relation between the rate of change of the magnetic field and the electric field in the conductive material. In reference to Figure 2.7, Faraday's law relates the alternating magnetic field generated by the coil to the electric field in the conductive domain.

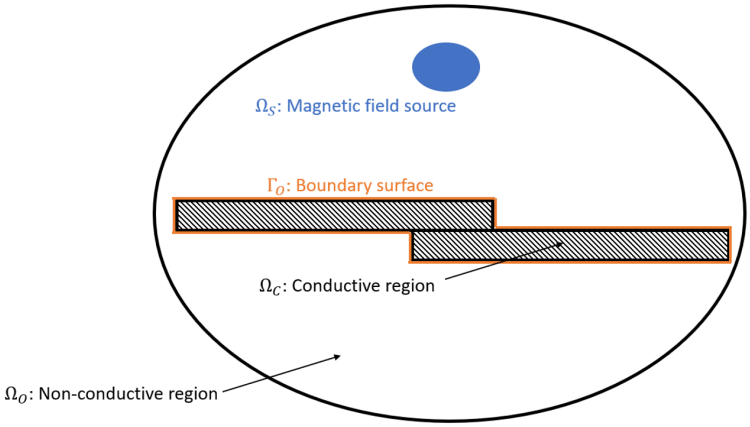

Figure 2.7: The physical elements involved in induction welding

$$\oint_C \vec{E} \cdot dl = -\iint_S \frac{d\vec{B}}{dt} \cdot dS \tag{2.2.1}$$

Here $\vec{E}$ is the electric field intensity that is induced around a closed loop line l by the time-variant magnetic flux density $\vec{B}$ through the stationary surface S that is enclosed by the loop. In this equation, the C in $\oint_C$ denotes a loop in the conductive domain. The elements of Faraday's law are shown visually in Figure 2.8.

Next is Maxwell-Ampere's law, which relates the electric flux density $\vec{D}$ to the magnetic field strength $\vec{H}$. Referencing Figure 2.7, the Maxwell-Ampere law relates the current in a coil to the magnetic field generated by the coil in the non-conductive domain, as is shown in Figure 2.9.

$$\oint_C \vec{H} \cdot dl = \frac{d}{dt} \iint_S \vec{D} \cdot dS + \iint_S \vec{J} \cdot dS \tag{2.2.2}$$

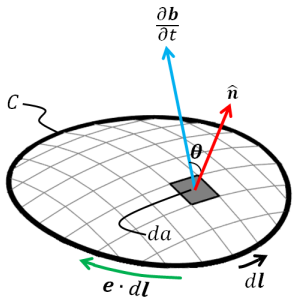

Figure 2.8: Faraday's law visualized [3]

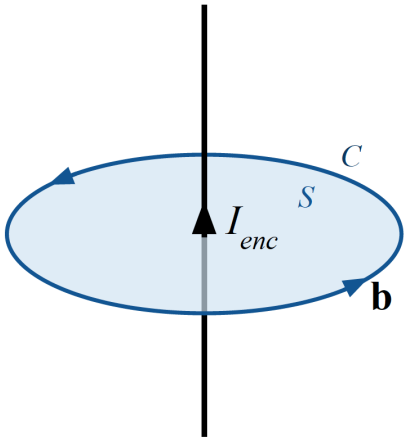

Figure 2.9: Maxwell-Ampere's law visualized [3]

Finally, the two remaining equations are the Gauss' laws for electricity, Eqn. 2.2.3, and magnetism, Eqn. 2.2.4.

$$\oiint_S \vec{D} \cdot dS = -\iiint_V \rho \, dV \tag{2.2.3}$$

Gauss' law for electricity states that the electric flux out of any enclosed surface is proportional to the total charge enclosed within the volume enclosed by that surface. Here ρ describes the electric charge density. According to Gauss' Law for electricity, the amount of charge in a volume V is equal to the total amount of electric flux $\vec{D}$ exiting the boundary surface S of the volume.

Finally, Gauss' law for magnetism states that the magnetic flux density $\vec{B}$ over a closed surface S is always zero. Thus, in Figure 2.7, the surface S of the conductive domain has the same amount of magnetic flux going into the volume as is coming out of the volume.

$$\oiint_S \vec{B} \cdot dS = 0 \tag{2.2.4}$$

These four equations describe the relation between electric and magnetic fields generated by static charges, magnetic sources and electrical currents.

2.3 The Eddy Current Problem

The problem treated in this document, the induction heating problem, is known as the time-harmonic eddy current problem, and the problem is solved through a finite element method-boundary element method (FEM-BEM) formulation as presented by Rodger in 1983 [38]. Multiple approaches to solving the time-harmonic eddy current problem are available. The governing equations can be solved using the magnetic field strength $\vec{H}$ [11] [39] or the electric field intensity $\vec{E}$ [40] as a state variable. Potential formulations have been used to solve the eddy current problem, involving the magnetic vector potential $\vec{A}$ formulation [41, 42] when solving for the magnetic field, a scalar potential field V for the electric field in the conductive domain, and a scalar potential ψ for the magnetic field in the non-conductive domain. Hybrid potential formulations that apply the vector potential $\vec{A}$ and scalar potential ψ were developed in the 1980s and applied to three-dimensional eddy current FEM-BEM coupling [43, 44].

To introduce the FEM-BEM problem, the domain of the problem is divided into three different domains. The first domain contains the coil. The second is a volume in which current is present, the conductive domain, see Figure 2.10. The third domain

is denoted by O in Figure 2.10 as the non-conductive domain.

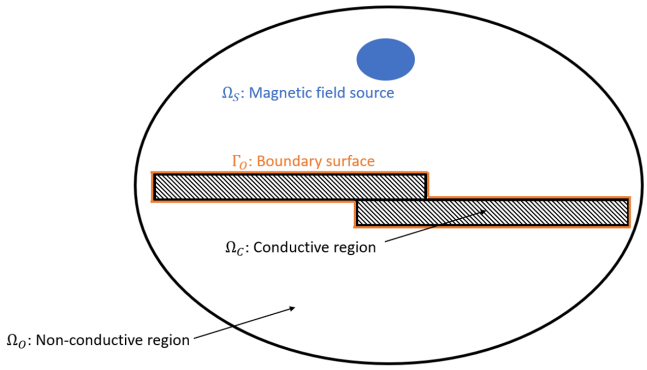

Figure 2.10: The physical elements involved in induction welding

For the volume of the non-conductive domain O, no calculation has to be done, instead a link is found between the discretization representing the coil and the discretized volume representing the weld zone [11]. In this dissertation, the eddy induction problem is solved by coupling finite elements and boundary elements. The boundary elements relate the magnetic field as generated by the coil to boundary conditions on the conductive domain. The finite element method is then employed to solve the weak formulation within the conductive domain with the boundary conditions, using the magnetic field $\vec{H}$ as the state variable. The method, as described by Bossavit [11, 10], formulates a solution that uses edge elements. These elements can represent a vector field with a single scalar, as the edges already have an orientation in space, as opposed to applying nodal shape functions to represent the vector field $\vec{H}$.

2.3.1 Maxwell's equations

The Maxwell equations, as shown in Eqns. 2.2.1, 2.2.2, 2.2.3 and 2.2.4, can be rewritten with Gauss' and Stokes' theorem which are presented in Eqns. 2.3.1 and 2.3.2 respectively.

$$\iiint_V \vec{\nabla} \cdot \vec{f}\, dV = \oiint_S \vec{f} \cdot dS \tag{2.3.1}$$

In this equation, V denotes the volume over which an integration is performed, $\vec{\nabla} \cdot \vec{f}$ is the divergence of the vector function $\vec{f}$, and S denotes a surface that encloses the volume V.

$$\iint_S (\vec{\nabla} \times \vec{f}) \cdot dS = \oint_C \vec{f} \cdot dl \tag{2.3.2}$$

In Stokes' theorem, S represents a surface bounded by the contour C. The surface integral of the curl of the function $\vec{f}$ is equal to the line integral of the function around that surface.

By applying Gauss' theorem to Gauss' laws, Eqns. 2.2.4 and 2.2.3, the integral form can be derived [45, 46] which yields:

$$\vec{\nabla} \cdot \vec{D} = \rho \tag{2.3.3}$$

$$\vec{\nabla} \cdot \vec{B} = 0 \tag{2.3.4}$$

By applying Stokes' theorem to Maxwell-Ampere law and Faraday's law, Eqns. 2.2.1 and 2.2.2 in the integral form can be rewritten to the differential form in similar ways as above [45, 46] yielding:

$$\vec{\nabla} \times \vec{E} = -\frac{\partial \vec{B}}{\partial t} \tag{2.3.5}$$

$$\vec{\nabla} \times \vec{H} = \frac{\partial \vec{D}}{\partial t} + \vec{J} \tag{2.3.6}$$

The equations are rewritten in the differential form to make the initial assump-

tions and derivations easier. These will later be rewritten to the integral form when applying the weak formulation. The magnetic field strength $\vec{H}$ is related to the magnetic flux density $\vec{B}$ through the magnetic permeability μ:

$$\vec{B} = \mu\vec{H} \tag{2.3.7}$$

the electric flux density and the electric field intensity are related through the permittivity ε:

$$\vec{D} = \varepsilon\vec{E} \tag{2.3.8}$$

The current density $\vec{J}$ and the electric field intensity $\vec{E}$ are related through the electrical conductivity tensor $\boldsymbol{\sigma}$ and the source current forced onto the system $\vec{J_S}$ by the extended form of Ohm's law:

$$\vec{J} = \vec{J_S} + \boldsymbol{\sigma}\vec{E} \tag{2.3.9}$$

In the case of a composite material, the material properties are assumed to be orthotropic, and the properties are assumed to be homogeneous in the plies. Therefore, the conductivity tensor is a 3×3 matrix, which defines the conductivity in the principal material axes system.

$$\boldsymbol{\sigma} = \begin{bmatrix} \sigma_{11} & 0 & 0 \\ 0 & \sigma_{22} & 0 \\ 0 & 0 & \sigma_{33} \end{bmatrix} \tag{2.3.10}$$

The conductivity tensor $\boldsymbol{\sigma}$ has the form of Eqn. 2.3.10, akin to a composite stiffness tensor. The ply properties are rotated through conventional means with the rotation matrix [47]:

$$R = \begin{bmatrix} \cos(\theta) & -\sin(\theta) & 0 \\ \sin(\theta) & \cos(\theta) & 0 \\ 0 & 0 & 1 \end{bmatrix} \tag{2.3.11}$$

Here θ is the angle of the ply rotation, which is equal to the ply angle if the coordinate system is equal to the principal material axes system. This yields the following expressions for the conductivity in the global coordinate system:

$$\begin{aligned} \sigma_{xx}^{\theta} &= m^4\sigma_{11} + n^4\sigma_{22} + 4m^2n^2\sigma_{33} \\ \sigma_{yy}^{\theta} &= n^4\sigma_{11} + m^4\sigma_{22} + 4m^2n^2\sigma_{33} \\ \sigma_{xy}^{\theta} &= m^2n^2\sigma_{11} + m^2n^2\sigma_{22} - 4m^2n^2\sigma_{33} \\ \sigma_{zz}^{\theta} &= m^2n^2\sigma_{11} + m^2n^2\sigma_{22} + \left(m^2 - n^2\right)^2\sigma_{33} \\ \sigma_{xz}^{\theta} &= m^3n\sigma_{11} - mn^3\sigma_{22} + 2\left(mn^3 - m^3n\right)\sigma_{33} \\ \sigma_{yz}^{\theta} &= mn^3\sigma_{11} - m^3n\sigma_{22} + 2\left(m^3n - mn^3\right)\sigma_{33} \end{aligned} \tag{2.3.12}$$

In Eqn. 2.3.12, the variable m is defined as the $\cos(\theta)$ and n is $\sin(\theta)$, and θ is the angle of the ply.

To solve the eddy current problem, two simplifications are made. First, the displacement current $\frac{\partial \vec{D}}{\partial t}$ is assumed to be small in comparison to the current induced by the magnetic field $\vec{J}$, as seen in Eqn. 2.3.6 and as substantiated in Appendix B.

$$max|\frac{\partial \vec{D}}{\partial t}| << |\vec{J}| \tag{2.3.13}$$

Then Ampere's law reduces from Eqn. 2.3.6 to:

$$\vec{\nabla} \times \vec{H} = \vec{J} \tag{2.3.14}$$

The second simplification is to introduce a time harmonic notation for the alternating source current density J_S [48] and assumes that $\vec{J_S}$, $\vec{H}$ and $\vec{E}$ are in phase:

$$\vec{J_S}(\vec{x},t) = \vec{J_*}(\vec{x})\cos(\omega t + \phi) = Re\left[\vec{J_*}(\vec{x})e^{i(\omega t)}\right] \tag{2.3.15}$$

Here the $\vec{J_*}$ represents a real-valued vector function and ω is the angular frequency and ϕ is the phase angle.

This allows us to re-write the time-harmonic representations for the electric field intensity $\vec{E}$ and the magnetic field intensity $\vec{H}$.

$$\begin{aligned} \vec{E}(\vec{x},t) &= Re\left[\vec{E_*}(\vec{x})e^{i(\omega t)}\right] \\ \vec{H}(\vec{x},t) &= Re\left[\vec{H_*}(\vec{x})e^{i(\omega t)}\right] \end{aligned} \tag{2.3.16}$$

Here $\vec{E_*}$ and $\vec{H_*}$ are complex vector functions. The time-harmonic representation allows us to find a term for the time derivative function of $\vec{B}$, by substituting 2.3.16 into 2.3.7.

$$\frac{\partial \vec{B}}{\partial t} = \frac{(x)Re\left[\mu\vec{H_*}(x)e^{i(\omega t)}\right]}{\partial t} = i\omega\mu\vec{H} \tag{2.3.17}$$

The equation above can then be substituted into Faraday's Law in Eqn. 2.3.5, note that the $\vec{E_*}$ and $\vec{H_*}$ complex vector functions have been re-symboled to $\vec{E}$ and $\vec{H}$ to avoid cluttering:

$$\vec{\nabla} \times \vec{E} + i\omega\mu\vec{H} = 0 \tag{2.3.18}$$

Substituting Eqns. 2.3.8 and 2.3.7 into Eqns. 2.3.3 and 2.3.4 respectively.

$$\begin{aligned} \vec{\nabla} \cdot \left(\varepsilon\vec{E}\right) &= \rho \\ \vec{\nabla} \cdot \left(\mu\vec{H}\right) &= 0 \end{aligned} \tag{2.3.19}$$

These yield the Gaussian laws in the differential form, which will be used in the derivation of the weak form. The second equation in Eqn. 2.3.19 drops out, since it is a consequence of Faraday's Law (Eqn. 2.3.18) [49, 45, 48].

2.3.2 Derivation of the weak form and separating the conductive and non-conductive domain

The set of equations as presented in the previous section lacks any applicability without the actual development of a piece of software that implements the theory and solves the problem. To construct a solution for the equations presented in the previous section, a weak formulation is constructed. The set of equations from the previous section (Eqns. 2.3.18, 2.3.14, 2.3.9) are restated here:

$$\vec{\nabla} \times \vec{E} + i\omega\mu\vec{H} = 0 \tag{2.3.20}$$

$$\vec{\nabla} \times \vec{E} = \vec{J} \tag{2.3.21}$$

$$\vec{J_S} + \boldsymbol{\sigma}\vec{E} = \vec{J} \tag{2.3.22}$$

In the non-conductive region (or the air) $\vec{\nabla} \times \vec{H_0} = 0$, where $\vec{H_0}$ is the magnetic field in the non-conductive domain O. In the coil $\vec{\nabla} \times \vec{H_S} = J_S$. Where $\vec{H_S}$ is the source magnetic field. These equations must be solved for $\vec{H}$ in the conductive domain, introducing the weak form of Eqn. 2.3.20 [50]. This is achieved by introducing the variational formulation. The equation is first put into a weighted-integral (or weighted-residual) form, as shown in Eqn. 2.3.23 [13]. A solution to Eqn. 2.3.20 is then found by selecting the approximation functions H' in the weighted-integral and setting the result to 0 [11]. If the weighted-integral is 0 the approximate functions H' and Φ' as introduced in the weighted-integral satisfy the original Eqn. 2.3.20.

$$\int_{\Omega} \left(i\omega\mu\vec{H} + \vec{\nabla} \times \vec{E} \right) \cdot \vec{H'} \, dV = 0 \tag{2.3.23}$$

This expression can be proven to have a unique solution through the Lax-Milgram's lemma, as demonstrated in [48], page 103. To proceed with the derivation, the two integrals are separated:

$$\int_{\Omega} \left(i\omega\mu\vec{H} \cdot \vec{H'} \right) \, dV + \int_{\Omega} \left(\vec{\nabla} \times \vec{E} \right) \cdot \vec{H'} \, dV = 0 \tag{2.3.24}$$

The second term, $\int_{\Omega} \vec{\nabla} \times \vec{E} \cdot \vec{H'} \, dV$, can be transformed through Green's formula [48]:

$$\int_{\Omega} \vec{\nabla} \times \vec{E} \cdot \vec{H'} \, dV = \int_{\Omega} \vec{E} \cdot \left(\vec{\nabla} \times \vec{H'} \right) \, dV - \int_{\Gamma} \vec{E} \times \vec{n} \cdot \vec{H'} \, dS = \int_{\Omega} \vec{E} \cdot \left(\vec{\nabla} \times \vec{H'} \right) \, dV \tag{2.3.25}$$

Note that in Eqn. 2.3.25 the term $-\int_{\Gamma} \vec{E} \times n \cdot \vec{H'} \, dS$ is 0. This can be shown by rewriting [48] the term using $\vec{E} \times n = -\vec{\nabla} V \times \vec{n}$ where V is a smooth function defined in the volume Ω:

$$\int_{\Gamma} \vec{E} \times \vec{n} \cdot \vec{H'} \, dS = -\int_{\Gamma} \vec{\nabla} V \times \vec{n} \cdot \vec{H'} \, dS = \int_{\Omega} \vec{\nabla} V \cdot \vec{\nabla} \times \vec{H'} dV \tag{2.3.26}$$

Then we can use that $V = 0$ on Γ which yields, which is true as there is no electric field going out of the surface:

$$\int_{\Omega} \vec{\nabla} V \cdot \left(\vec{\nabla} \times \vec{H'} \right) \, dV = \int_{\Gamma} V \left(\vec{\nabla} \times \vec{H'} \cdot n \right) \, dS = 0 \tag{2.3.27}$$

Having proven Eqn. 2.3.25, it is now substituted into 2.3.24 and yields:

$$i\omega \int_{\Omega} \left(\mu\vec{H} \cdot \vec{H'} \right) \, dV + \int_{\Omega} \left(\vec{E} \cdot \left(\vec{\nabla} \times \vec{H'} \right) \right) \, dV = 0 \tag{2.3.28}$$

$\vec{E}$ can be eliminated from Eqn. 2.3.28 when evaluating the equation outside the conductive region, as outside the conductive region the curl of the trial function H' is zero, $\vec{\nabla} \times \vec{H'} = 0$. The remaining volume is the conductive region Ω_C.

Evaluating Eqn. 2.3.22 in the conductive region, there is no source current as the current is solely a function of the electric field $\vec{E}$; hence the third equation Eqn. 2.3.22 becomes $\vec{E} = \boldsymbol{\sigma}^{-1}\vec{J}$. Substituting into Eqn. 2.3.14 results in $\vec{E} = \vec{\sigma}^{-1}\left(\nabla \times \vec{H}\right)$ substituting in Eqn. 2.3.28 yields:

$$i\omega \int_{\Omega} \left(\mu \vec{H} \cdot \vec{H'}\right)\, dV + \int_{\Omega_C} \left(\boldsymbol{\sigma}^{-1}\left(\vec{\nabla} \times \vec{H}\right) \cdot \left(\vec{\nabla}\ \times \vec{H'}\right)\right)\, dV = 0 \tag{2.3.29}$$

For the next step, the assumption is made that the conductive domain is without holes or loops. As there is no source current in the conductive domain, the source magnetic field can be rewritten to be a function of the gradient of a scalar potential field:

$$\vec{H_S} = \vec{\nabla}\Phi_S \tag{2.3.30}$$

The response magnetic field in the non-conductive domain is :

$$\vec{H} = \vec{H_S} + \vec{\nabla}\left(\Phi - \Phi_S\right) \tag{2.3.31}$$

$$\vec{H'} = \vec{H_S} + \vec{\nabla}\left(\Phi' - \Phi_S\right) \tag{2.3.32}$$

Applying the response magnetic fields to Eqn. 2.3.29 and splitting up the first integral, which is currently defined as still being over the full domain, over the conductive and non-conductive domain:

$$i\omega \int_{\Omega_C} \left(\mu \vec{H} \cdot \vec{H}'\right)\ dV + i\omega\mu_0 \int_{\Omega_O} \left(\vec{H}_S + \vec{\nabla}\left(\Phi - \Phi_S\right)\right) \cdot \left(\vec{H}_S + \vec{\nabla}\left(\Phi' - \Phi_S\right)\right)\ dV + \int_{\Omega_C} \left(\sigma^{-1}\left(\vec{\nabla} \times \vec{H}\right) \cdot \left(\vec{\nabla} \times \vec{H}'\right)\right)\ dV = 0 \quad (2.3.33)$$

In the next section, the application of the Biot-Savart law to find the source magnetic field is discussed.

2.3.3 Loads and boundary conditions on the conductive domain

To compute the source magnetic field $\vec{H}_S$ and the source magnetic scalar potential Φ_S, the Biot-Savart law is employed:

$$\vec{H}_S(\vec{x}) = \frac{1}{4\pi} \int \frac{I\vec{e}_{12} \times d\vec{s}}{\vec{r}_{12}^2} \quad (2.3.34)$$

The magnetic field generated by the coil can be found by discretizing the coil into elements, as shown in Figure 2.11.

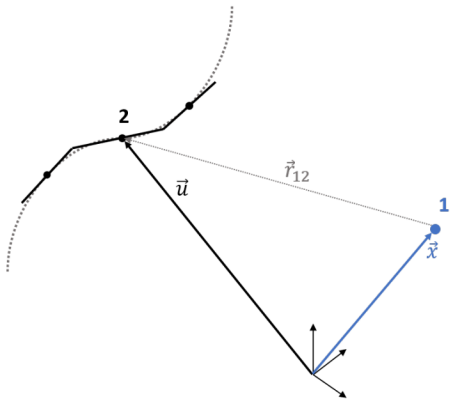

Figure 2.11: Discretization of the Biot-Savart law

The magnetic field of each individual line element $d\boldsymbol{s}$ is calculated at point $\vec{x}$ or point 1, where r_{12} is the distance between points 1 and 2. This procedure can be discretized, as shown in Figure 2.11 [1, 10].

$$\vec{H}_S(\vec{x}) = \frac{I}{4\pi} \int_{\vec{u}^{n-1/2}}^{\vec{u}^{n+1/2}} \frac{(\vec{u} - \vec{x}) \times d\vec{u}}{\vec{r}_{12}^{3}} \tag{2.3.35}$$

The Biot-Savart law will be symbolically integrated by assuming that the electric current is constant over the coil and the distance between point 1 and 2 is constant over each line segment. The result is a summation of the contributions of the individual line segments, w which are used to discretize the coil. This will then provide the source magnetic field:

$$\vec{H_S} = \frac{I}{4\pi} \sum_w f(\vec{x}, \vec{X}) \tag{2.3.36}$$

Here $\vec{X}$ contains the coordinates of the start and end of the coil segment, and f is the function inside the integral in Eqn. 2.3.35. The source scalar magnetic potential is as defined in Eqn. 2.3.30. Now that the magnetic field at a location $\vec{x}$ is defined, the difference in potential can be calculated from the line integral:

$$\Phi_2 - \Phi_1 = \int_1^2 \vec{H_S} \cdot ds \tag{2.3.37}$$

Substituting 2.3.36 into 2.3.37 yields:

$$\Phi_2 - \Phi_1 = \int_1^2 \frac{I}{4\pi} \sum_w f(\vec{x}, \vec{X}) \; d\boldsymbol{s} \tag{2.3.38}$$

Note that the process of finding the potentials on the surface of the conductive domain can be started at any point by setting the source magnetic potential at that point to zero and integrating along over the surface to find the scalar potential in all nodes of the boundary surface.

Before going to the element definitions, a few remarks regarding the discretization method as introduced by Bossavit[10]. The load vectors $\vec{\Phi_S}$ and $\vec{L_S}$ are zero inside the conductive domain and non-zero on the interface of the conductive and in the

non-conductive domain.

A potential field can only be calculated by the line integral if the vector field is conservative. A conservative field is a vector field in which the curl is zero or the line integral is path independent. These fields are often used to model vector fields in which no work is done. This means the following must be true on the boundary Γ_c:

$$\vec{J} = \left(\vec{\nabla} \times \left(\vec{\nabla}\Phi\right)\right) = 0 \tag{2.3.39}$$

Since a gradient field is curl-free by definition[49], the boundary condition $\vec{H} \times n = 0$ on the boundary Γ_c[45, 48, 10] is satisfied naturally.

2.3.4 The Dirichlet-to-Neumann mapping

In the previous section, a weak-formulation was derived to solve the magneto-static problem and Biot-Savart law was employed to find the scalar potential Φ on the surface of the conductive domain. The weak formulation, as derived in Eqn. 2.3.33, contains two types of integrals: the integral over the conductive domain Ω_C and the integral over the non-conductive domain Ω_O. To solve the integral without having to discretize the non-conductive domain or specify boundary conditions for the non-conductive domain [51], the problem is turned into a hybrid finite element boundary element problem. This carries an advantage, as a finite element solution of this problem would contain artificial boundary conditions at the edge of the discretized non-conductive space. These artificial boundary conditions must be carefully managed, or these may cause a spurious or otherwise incorrect solution [51]. The boundary integral equation formulated on the boundary of the conductive domain not only reduces the domain that needs to be discretized, but the boundary conditions at ∞ will be naturally satisfied.

In the previous section, the scalar magnetic potential Φ on the interface of the conductive and non-conductive domain is found. In Eqn. 2.3.33, the term $\vec{\nabla}\Phi$ can

be rewritten: $\vec{\nabla}\Phi \cdot \vec{\nabla} = \frac{\partial \Phi(\vec{x})}{\partial n}$. To solve this, equation a Neumann boundary condition ($\frac{\partial \Phi(\vec{x})}{\partial n}$) is required, however, from the Biot-Savart law a Dirichlet boundary condition (Φ) is acquired. To overcome this obstacle, the single layer source method is introduced.

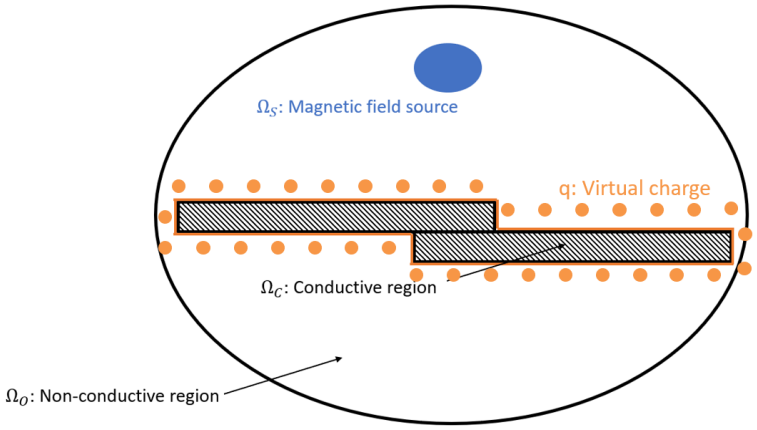

Figure 2.12: Virtual charges as distributed on the interface of the conductive and non-conductive domain

In the single layer source method, the potential field on the boundary Γ is related to a virtual charge q located in $(\vec{x})$ on the boundary, see Figure 2.12. The scalar potential can be expressed by the following integral [10, 51, 52]:

$$\Phi(\vec{x}) = \int_{\Gamma} q(y) \cdot \frac{1}{||\vec{r}_{\vec{x}\vec{y}}||} \, dS_y \tag{2.3.40}$$

In this equation, $\vec{x}$ is a location on the boundary surface Γ, as is $\vec{y}$. The vector between these two points is $\vec{r}_{\vec{x}\vec{y}}$. $q(y)$ is a virtual charge on the boundary of the laminate. From the potential Φ, the magnetic field can be derived by $\vec{H} = \vec{\nabla}\Phi$. Eqn. 2.3.40 maps the virtual charge to the Dirichlet boundary conditions. Applying the variational approach to Eqn. 2.3.40 yields the weak formulation:

$$\int_{\Gamma} \Phi(\vec{x}) \cdot \Phi'(\vec{x}) d\vec{S}_x = \int_{\Gamma} \int_{\Gamma} q(\vec{y}) \cdot \frac{1}{||\vec{r}_{\vec{x}\vec{y}}||} \Phi'(\vec{x}) \, dS_y \, dS_x \tag{2.3.41}$$

From potential theory, the normal derivative of the potential value at a point $\vec{x}$ on the boundary Γ can be expressed by the following integral [10, 51, 52]:

$$\vec{\nabla}\Phi = \frac{\partial\Phi(\vec{x})}{\partial n} = 2\pi q(\vec{x}) - \int_{\Gamma} q(\vec{y}) \cdot \frac{\vec{n}_x \cdot \vec{r}_{\vec{x}\vec{y}}}{||\vec{r}^{3}_{\vec{x}\vec{y}}||}\, dS_y \tag{2.3.42}$$

In Eqn. 2.3.42, the variable $\vec{n}_x$ is the unit normal vector of the surface at the point x. This equation relates the virtual charge $q\,(\vec{y})$ to the derivative of the potential $\frac{\partial\Phi}{\partial n}$. Introducing the variational formulation results in Eqn. 2.3.43 [10, 51, 52].

$$\int_{\Gamma} \frac{\partial\Phi(\vec{x})}{\partial n}\Phi'(\vec{x})\, dS_x = \int_{\Gamma} 2\pi\; q(\vec{x}) \cdot \Phi'(\vec{x})\, dS_x - \int_{\Gamma}\int_{\Gamma} q(\vec{y}) \cdot \frac{\vec{n}_x \cdot \vec{r}_{\vec{x}\vec{y}}}{||\vec{r}_{\vec{x}\vec{y}}||^3}\, dS_y\, dS_x \tag{2.3.43}$$

From Eqn. 2.3.41, a relation between the virtual charge q and the potential Φ is found and from Eqn. 2.3.43, a relation between the virtual charge and the derivative of the potential. Discretizing these equations by virtue of the boundary element method, a system of matrix equations can be found:

$$\Phi\,(\vec{x}) = \boldsymbol{K} q \tag{2.3.44}$$

$$\vec{\nabla}\Phi = \frac{\partial\Phi(\vec{x})}{\partial n} = (\boldsymbol{B}/2 + \boldsymbol{H})\, q \tag{2.3.45}$$

Eliminating the virtual charge from Eqn. 2.3.44 by substituting Eqn. 2.3.45 in Eqn. 2.3.44 yields:

$$\frac{\partial\Phi(\vec{x})}{\partial n} = (\boldsymbol{B}/2 + \boldsymbol{H})\, \boldsymbol{K}^{-1}\; \Phi\,(\vec{x}) \tag{2.3.46}$$

The term $(\boldsymbol{B}/2 + \boldsymbol{H})\, \boldsymbol{K}^{-1}$ is known as the Poincaré-Steklov operator and relates the Dirichlet boundary condition to the Neumann boundary condition:

$$\boldsymbol{P}^* = (\boldsymbol{B}/2 + \boldsymbol{H})\,\boldsymbol{K}^{-1} \tag{2.3.47}$$

This naive implementation is not symmetric, and thus symmetry needs to be introduced. This is done through the following equation [10]:

$$\boldsymbol{P} = \frac{1}{2}\left(\boldsymbol{P}^*\boldsymbol{B}^T + \left(\boldsymbol{P}^*\boldsymbol{B}^T\right)^T\right) \tag{2.3.48}$$

Note that this forces symmetry, which could introduce a discretization error [10].

2.3.5 Reformulating to the boundary of the conductive domain

In this section, Eqn. 2.3.33 is reformulated such that the integration over the non-conductive domain is replaced with an integral over the surface of the conductive domain. The integral over the non-conductive domain in Eqn. 2.3.33 is defined as follows:

$$Z = \int_{\Omega_O} \left(\vec{H} + \vec{\nabla}\left(\Phi - \Phi_S\right)\right) \cdot \left(\vec{H} + \vec{\nabla}\left(\Phi' - \Phi_S\right)\right)\, dV \tag{2.3.49}$$

Using the properties of the Poincare-Steklov operator found in the previous section, Eqn. 2.3.49 can be rewritten:

$$Z = \int_{\Omega_O} \left(\vec{H} - \vec{\nabla}\left(\Phi\right)\right)^2\, dV + 2\int_{\Gamma} \vec{n}\cdot\vec{H}\; dS + \int_{\Gamma} P\Phi\Phi'\; dS - 2\int_{\Gamma} P\Phi_S\Phi'\; dS \tag{2.3.50}$$

This result can then be substituted in Eqn. 2.3.33:

$$i\omega \int_{\Omega_C} \left(\mu \vec{H} \cdot \vec{H}'\right)\ dV + i\omega\mu_0 \int_{\Omega_O} \left(\vec{H} - \nabla\left(\vec{\Phi}\right)\right)^2\ dS + 2\int_{\Gamma} \vec{n} \cdot \vec{H}\ dS + \int_{\Gamma} P\Phi\Phi'\ dS - 2\int_{\Gamma} P\Phi_S\Phi'\ dS + \int_{\Omega_C} \left(\boldsymbol{\sigma^{-1}}\left(\nabla \times \vec{H}\right) \cdot \left(\nabla \times \vec{H}'\right)\right)\ dV = 0 \quad (2.3.51)$$

Note that the second integral is 0 since the definition of the scalar potential is $\vec{H} = \vec{\nabla}\Phi$, and the third and fourth integral can be combined into one, resulting in the following equation:

$$i\omega \int_{\Omega_C} \left(\mu \vec{H} \cdot \vec{H}'\right)\ dV + i\omega\mu_0 \int_{\Gamma} \vec{P}\Phi\Phi'\ dS + \int_{\Omega_C} \boldsymbol{\sigma^{-1}}\left(\vec{\nabla} \times \vec{H}\right) \cdot \left(\vec{\nabla} \times \vec{H}'\right)\ dV = \int_{\Gamma} \left(P\Phi_S\Phi' - \vec{n}_B \cdot \vec{H}\Phi'\right) dS \quad (2.3.52)$$

In this equation, the scalar potential Φ and the magnetic field $\vec{H}$ are the state variables.

2.3.6 Finite Element Discretization of the State Variables

In this section, the finite element discretization of the state variables will be discussed. To discretize the weak formulation that was derived in the previous section, Eqn. 2.3.52, the scalar potential Φ is discretized with nodal shape functions, while the magnetic field is discretized with edge elements. The edge elements have degrees of freedom assigned to the edges, thus allowing a scalar value to represent a vector in the direction of the edge.

Mixing finite element types, i.e. mixing node elements and edge elements in a single element, is not new. These mixed 3D elements were first described by Nedelec [53] in 1980. Mixed finite element were applied to electromagnetic simulation by Bossavit [44] and used by Holland [1] for the development of the WelDone soft-

ware. Holland used a hexahedral element, the geometry of which is based on the location of 2-nodes. Through this definition, the shape functions of the element can be simplified. However, it limits the geometry of the element significantly, as there are only 6 coordinates or 2 nodes, (x_1, y_1, z_1) and (x_7, y_7, z_7), defining the element. By comparison, a conventional hexahedral has 24 coordinates defining the geometry of the element. The nodes, edges and surface are numbered as defined in Figure 2.13. The element still retains its 8 nodal variables and 12 edge variables, through which a vector or scalar field can be defined.

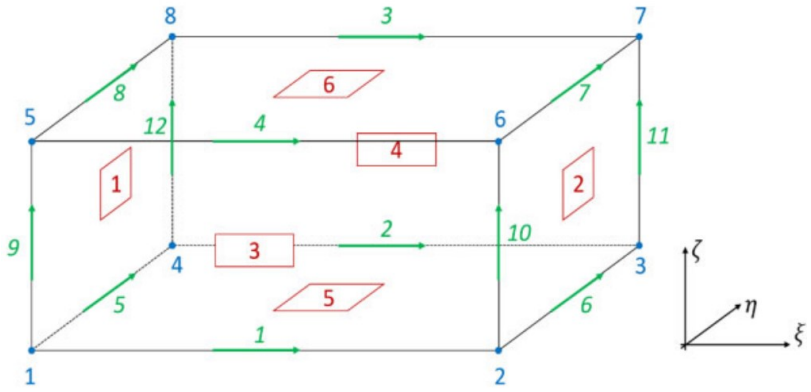

Figure 2.13: Brick element with 8 nodes and 12 edges [1]

In this dissertation, a fully defined 8-node element is created, where the coordinates of each node in the element are defined independent of the coordinates of the other nodes in the element. Then, the relation between the nodal and edge shape functions, N_n and $\vec{N}_e$, and the state variables is created.

$$\vec{\Phi} = \sum_{n \in N_s} \Phi_n N_n \tag{2.3.53}$$

$$\vec{H} = \sum_{e \in E_C} H_e \vec{N}_e + \sum_{n \in N_s} \Phi_n \vec{\nabla} N_n \tag{2.3.54}$$

In Eqn. 2.3.54, E_C denotes a set containing all the edges of the conductive domain Ω_C. N_s is a set containing all the nodes on the boundary surface of the conductive

domain. This implies that there will be a scalar degree of freedom H_e on every internal edge and a scalar degree of freedom Φ_n on each node on the surface of the conductive domain.

The weak formulation, as described in Eqn. 2.3.52 can now be rewritten with Eqns. 2.3.53 and 2.3.54:

$$i\omega \left(\boldsymbol{M}(\mu) + \mu_0 \boldsymbol{P}\right) \boldsymbol{\kappa} + \boldsymbol{N}(\boldsymbol{\sigma})\boldsymbol{\kappa} = i\omega\mu_0 \left(\boldsymbol{P\Phi} - \boldsymbol{L}\right) \tag{2.3.55}$$

In this equation, the matrix $\boldsymbol{M}$ originates from the first integral in Eqn. 2.3.52 which can be discretized through Eqns. 2.3.53 and 2.3.54:

$$\boldsymbol{M}(\mu) = i\omega \iiint_{\Omega_C} \left(\mu \vec{H} \cdot \vec{H}'\right)\, dV = \mu \iiint_{\Omega_C} \left(\sum_{e \in E_C} H_e \vec{N}_e + \sum_{n \in N_s} \Phi_n \nabla N_n\right) \cdot \vec{H}'\, dV \tag{2.3.56}$$

The test function H' is the edge shape function $\vec{N}_e$ for the edges and $\vec{\nabla} N_n$ for the nodes.

The matrix $\boldsymbol{M}$ is dependent on the element geometry and location, and has 3 sub-matrices: $\boldsymbol{M_{ee}}$, $\boldsymbol{M_{ne}}$, $\boldsymbol{M_{nn}}$ resulting in the following equations:

$$\boldsymbol{M}\kappa = \begin{bmatrix} \boldsymbol{M_{ee}} & \boldsymbol{M_{en}} \\ \boldsymbol{M_{ne}} & \boldsymbol{M_{nn}} \end{bmatrix} \begin{bmatrix} H_e \\ \Phi_n \end{bmatrix} \tag{2.3.57}$$

Calculating the contributions of the global matrix $\boldsymbol{M}$ element wise, for element a results in:

$$
\begin{aligned}
M^a_{ee} &= \iiint_{\Omega_a} \mu_a \vec{N}_k \cdot \vec{N}_l \; dV, \quad \text{for edges } k \text{ and } l \text{ on element } a \\
M^a_{ne} = M^a_{en} &= \iiint_{\Omega_a} \mu_a \left(\vec{\nabla} N_i\right) \cdot \vec{N}_k \; dV, \quad \text{for edge } k \text{ and node } i \text{ on element } a \\
M^a_{nn} &= \iiint_{\Omega_a} \mu_a \left(\vec{\nabla} N_i\right) \cdot \left(\vec{\nabla} N_i\right) \; dV, \quad \text{for nodes } i, j \text{ on element } a
\end{aligned}
\tag{2.3.58}
$$

Where Ω_a denotes the volume of element a in the conductive domain. $\vec{\nabla} N_i$ is the gradient of the nodal shape functions and $\vec{N}_k$ are the edge shape functions.

The matrix $\boldsymbol{N}$ is found by expanding the last integral on the left hand side of Eqn. 2.3.52, and eliminating the terms involving the gradient, as $\vec{\nabla} \times \vec{\nabla} N_n = 0$ since a gradient field is curl free.

$$
\begin{aligned}
\vec{N}^a_{kl} &= \iiint_{\Omega_c} \boldsymbol{\sigma}^{-1} \left(\vec{\nabla} \times \vec{H}\right) \cdot \left(\vec{\nabla} \times \vec{H}'\right) \; dV \\
&= \iiint_{\Omega_c} \left(\boldsymbol{\sigma}^{-1} \left(\vec{\nabla} \times \vec{N}_k\right)\right) \cdot \left(\vec{\nabla} \times \vec{N}_l\right) \; dV \\
&\qquad \text{for edges } k \text{ and } l \text{ on element } a
\end{aligned}
\tag{2.3.59}
$$

Finally, the $\boldsymbol{L}$ and $\boldsymbol{P}$ matrices from Eqn. 2.3.55 have to be found. The matrix $\boldsymbol{L}$ is the load vector, which can be found by integrating the normal component of the magnetic source field $\vec{H}_S$ over the boundary surface of the conductive volume, which is the second integral in Eqn. 2.3.52.

$$
\boldsymbol{L} = \iint_{\Gamma} \vec{n_B} \cdot \vec{H}_S N_n \; dS \text{ for node } n \text{ on the boundary surface} \tag{2.3.60}
$$

The Dirichlet-to-Neumann map $\boldsymbol{P}$ is based on three sub-matrices:

$$\boldsymbol{P} = \frac{1}{2}\left(\left(\frac{\boldsymbol{B}}{2} + \boldsymbol{H}\right)\boldsymbol{K}^{-1}\boldsymbol{B}^{T} + \left(\left(\frac{\boldsymbol{B}}{2} + \boldsymbol{H}\right)\boldsymbol{K}^{-1}\boldsymbol{B}^{T}\right)^{T}\right) \tag{2.3.61}$$

In this equation the matrices $\boldsymbol{B}$, $\boldsymbol{K}$ and $\boldsymbol{H}$ are defined as follows:

$$B_e^a = \int_\Gamma N_i(\vec{x})\zeta_a(\vec{x})d\vec{x} \tag{2.3.62}$$

$$K_e^a = \frac{1}{4\pi}\int_\Gamma \left(\int_\Gamma \frac{\zeta_a(\vec{x})\zeta_b(\vec{y})}{||\vec{y}-\vec{x}||}\, d\vec{x}\right) d\vec{y} \tag{2.3.63}$$

$$H_e^a = \frac{1}{4\pi}\int_\Gamma \left(\int_\Gamma \frac{n_{\Omega_O}(\vec{x})\cdot(\vec{y}-\vec{x})\,\zeta_a(\vec{y})\vec{N}_e(\vec{x})}{||\vec{y}-\vec{x}||^3}\, d\vec{x}\right) d\vec{y} \tag{2.3.64}$$

The vectors $\vec{x}$ and $\vec{y}$ are two points on the boundary surface, Γ of the conductive domain Ω_C. Both $d\vec{x}$ and $d\vec{y}$ refer to the coordinates on the surface Γ over which integration takes place. The indices a and b refer to the 2D-elements on the surface of Γ. The variables ζ_a and ζ_b are 1 divided by the area of the respective surface element and 0 in any other position. N_i is the weighting function for the node i.

2.4 Elements and Element Definitions

In this section, three element formulations are presented that can be used to replace the current cuboid elements. In the first subsection, Subsection 2.4.1, first order 8-node hexahedral elements are discussed. In Subsection 2.4.3 second order 27-node hierarchical hexahedrons are reviewed. In the final subsection, Subsection 2.4.4, first order tetrahedral elements are presented.

2.4.1 First Order 8-node Hexahedral Element

In this section, the 8-node linear element is represented. The implementation, as discussed here, is based on 8-nodes, each defined with 3 independent coordinates (x, y, z) or (ξ, η, ζ), as opposed to having the element geometry described by only two nodes, limiting the application to rectangular brick mesh. The configuration for an iso-parametric element is shown in Figure 2.14.

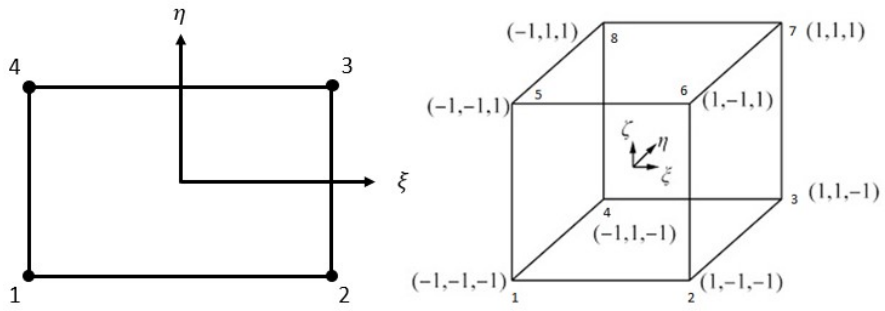

Figure 2.14: The nodes of a 4-node iso-parametric surface element (left) and an 8-node iso-parametric volume element (right)

The nodal shape functions for the 4-node quadrilateral surface are defined as:

$$N_i = \frac{1}{4}\left(1 + \xi\xi_i\right)\left(1 + \eta\eta_i\right) \tag{2.4.1}$$

Here, i denotes the node number of the shape functions and ξ and η denote the local coordinate system.

The nodal shape functions for the 8-node brick element are defined as:

$$N_i = \frac{1}{8}\left(1 + \xi\xi_i\right)\left(1 + \eta\eta_i\right)\left(1 + \zeta\zeta_i\right) \tag{2.4.2}$$

The edge shape function for the 8 node brick element is described below [54]:

$$\vec{N}_p = \begin{bmatrix} N_p^{\xi} \\ N_p^{\eta} \\ N_p^{\zeta} \end{bmatrix} \tag{2.4.3}$$

The components of the edge shape functions are defined by:

$$\begin{aligned} N_p^{\xi} &= \frac{1}{8}\left(1+\eta\eta_p\right)\left(1+\zeta\zeta_p\right)\vec{\nabla}\xi \\ N_p^{\eta} &= \frac{1}{8}\left(1+\zeta\zeta_p\right)\left(1+\xi\xi_p\right)\vec{\nabla}\eta \\ N_p^{\zeta} &= \frac{1}{8}\left(1+\eta\eta_p\right)\left(1+\xi\xi_p\right)\vec{\nabla}\zeta \end{aligned} \tag{2.4.4}$$

Here, $\vec{\nabla}\xi$ is defined as:

$$\vec{\nabla}\xi = \begin{bmatrix} \frac{\partial\xi}{\partial x} \\ \frac{\partial\xi}{\partial y} \\ \frac{\partial\xi}{\partial z} \end{bmatrix} \tag{2.4.5}$$

The variables $\vec{\nabla}\eta$ and $\vec{\nabla}\zeta$ are defined in a similar manner, replacing ξ for η and ζ.

2.4.2 Second Order 20-node Hexahedral Elements

In this section, the shape functions for an interpolatory 20-node element hexahedron will be presented. For the implementation of the element, the shape functions for the surface of an 8-node element are required. The element node numbering is as defined in Figure 2.15.

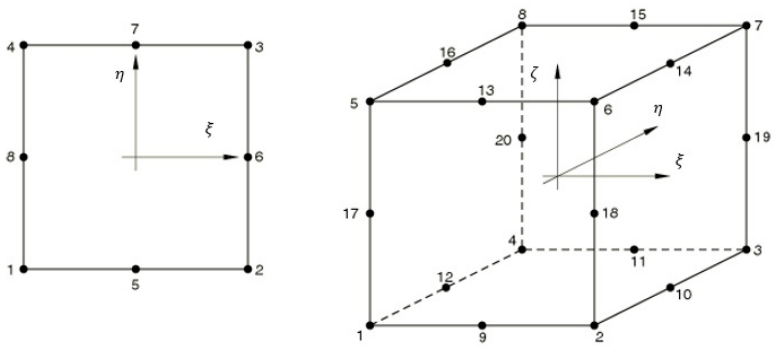

Figure 2.15: The nodes of an 8-node surface element (left) and a 20-node volume element (right)

The resulting surface nodal shape functions are [55]:

$$\begin{aligned} N_i &= \frac{1}{4}\left(1+\xi_i\xi\right)\left(1+\eta_i\eta\right)\left(\xi_i\xi+\eta_i\eta-1\right) \\ N_i &= \frac{1}{2}\left(1-\xi^2\right)\left(1+\eta_i\eta\right), \text{ for } \xi_i = 0 \\ N_i &= \frac{1}{2}\left(1+\xi_i\xi\right)\left(1-\eta^2\right), \text{ for } \eta_i = 0 \end{aligned} \tag{2.4.6}$$

These coincide with the nodes on the surface element, as shown in Figure 2.15. The volume nodal shape functions for a 20-node element are [55]:

$$\begin{aligned} N_i^n &= \frac{1}{8}\left(1+\xi_i\xi\right)\left(1+\eta_i\eta\right)\left(1+\zeta_i\zeta\right)\left(\xi_i\xi+\eta_i\eta+\zeta_i\zeta-2\right) \\ N_i^n &= \frac{1}{4}\left(1-\xi^2\right)\left(1+\eta_i\eta\right)\left(1+\zeta\zeta_i\right) \text{ for the middle nodes with } \xi_i = 0 \\ N_i^n &= \frac{1}{4}\left(1-\eta^2\right)\left(1+\xi_i\xi\right)\left(1+\zeta\zeta_i\right) \text{ for the middle nodes with } \eta_i = 0 \\ N_i^n &= \frac{1}{4}\left(1-\zeta^2\right)\left(1+\eta_i\eta\right)\left(1+\xi\xi_i\right) \text{ for the middle nodes with } \zeta_i = 0 \end{aligned} \tag{2.4.7}$$

The edge shape functions for the physical edges of the element shown in Figure 2.15 are shown in Eqn. 2.4.8. Three edge shape functions are displayed in Eqns. 2.4.8 and 2.4.9, since the edge shape equations are different for the three different principal directions. The top equation of Eqn. 2.4.8 is used to find the edge functions for the

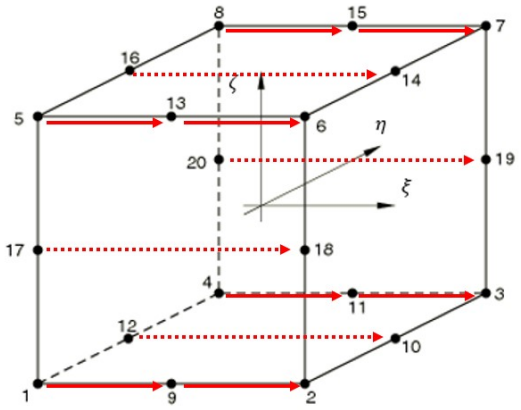

Figure 2.16: The edges in the ξ direction on a 20-node element

physical edges in the ξ-direction, which are the edges marked in solid red arrows in Figure 2.16.

$$
\begin{aligned}
N_i^{\xi} &= \frac{1}{8}\left(1+\eta_i\eta\right)\left(1+\zeta_i\zeta\right)\left(\xi_i\xi+\eta_i\eta+\zeta_i\zeta-1\right)\vec{\nabla}\xi \\
N_i^{\eta} &= \frac{1}{8}\left(1+\xi_i\xi\right)\left(1+\zeta_i\zeta\right)\left(\xi_i\xi+\eta_i\eta+\zeta_i\zeta-1\right)\vec{\nabla}\eta \\
N_i^{\zeta} &= \frac{1}{8}\left(1+\xi_i\xi\right)\left(1+\eta_i\eta\right)\left(\xi_i\xi+\eta_i\eta+\zeta_i\zeta-1\right)\vec{\nabla}\zeta
\end{aligned}
\tag{2.4.8}
$$

For the same reason, multiple equations are required to define the non-physical edges. The non-physical edges are indicated by the dotted arrows in Figure 2.16, the shape functions for these edges are given in Eqn. 2.4.9 [56].

$$
\begin{aligned}
N_i^{\xi} &= \frac{1}{4}\left(1-\eta^2\right)\left(1+\zeta_i\zeta\right)\vec{\nabla}\xi, \quad \text{if} \quad \eta = \pm 1 \\
N_i^{\xi} &= \frac{1}{4}\left(1+\eta\eta_i\right)\left(1-\zeta^2\right)\vec{\nabla}\xi, \quad \text{if} \quad \zeta = \pm 1 \\
N_i^{\eta} &= \frac{1}{4}\left(1-\xi^2\right)\left(1+\zeta_i\zeta\right)\vec{\nabla}\eta, \quad \text{if} \quad \xi = \pm 1 \\
N_i^{\eta} &= \frac{1}{4}\left(1+\xi\xi_i\right)\left(1-\zeta^2\right)\vec{\nabla}\eta, \quad \text{if} \quad \zeta = \pm 1 \\
N_i^{\zeta} &= \frac{1}{4}\left(1-\eta^2\right)\left(1+\xi_i\xi\right)\vec{\nabla}\zeta, \quad \text{if} \quad \eta = \pm 1 \\
N_i^{\zeta} &= \frac{1}{4}\left(1+\eta\eta_i\right)\left(1-\xi^2\right)\vec{\nabla}\zeta, \quad \text{if} \quad \xi = \pm 1
\end{aligned}
\tag{2.4.9}
$$

2.4.3 Second Order Hierarchical 27-node Hexahedral Elements

The shape functions for the higher order hexahedral element are constructed in their hierarchic forms. This approach is chosen as it allows easy expansion in future work to a third or fourth order shape function if desired. In Eqn. 2.4.10, the shape function for a quadratic hierarchical line element is shown. These are sourced from Wunderlich [4], page 356, but are also available in Zienkiewicz [55]. The basis functions, N_l^L for a line element containing l nodes, are defined by Eqn. 2.4.10.

$$
N_l^L = \frac{\prod_{j=1, j\neq i}^{m}(\xi - \xi_j)}{\prod_{j=1, j\neq i}^{m}(\xi_i - \xi_j)} \tag{2.4.10}
$$

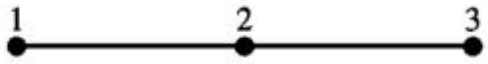

Figure 2.17: Line element with 3 nodes

Generating the three basis functions for a quadratic 3-node line element, as shown in Figure 2.17, results in Eqn. 2.4.11.

$$
\begin{aligned}
N_1^L &= \frac{(\xi - \xi_2)(\xi - \xi_3)}{(\xi_1 - \xi_2)(\xi_1 - \xi_3)} \\
N_2^L &= \frac{(\xi - \xi_1)(\xi - \xi_3)}{(\xi_2 - \xi_1)(\xi_2 - \xi_3)} \\
N_3^L &= \frac{(\xi - \xi_1)(\xi - \xi_2)}{(\xi_3 - \xi_1)(\xi_3 - \xi_2)}
\end{aligned}
\tag{2.4.11}
$$

Simplifying these for a line element in the natural coordinate system, which entails that $\xi_1 = -1$, $\xi_2 = 0$ and $\xi_3 = 1$, results in the following equations for the shape functions of the 3-node line:

$$
\begin{aligned}
N_1^L(\xi) &= \frac{(\xi)(\xi - 1)}{2} \\
N_2^L(\xi) &= -(\xi + 1)(\xi - 1) \\
N_3^L(\xi) &= \frac{(\xi + 1)(\xi)}{2}
\end{aligned}
\tag{2.4.12}
$$

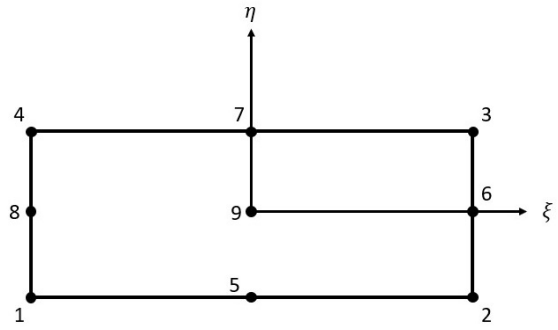

Figure 2.18: A 9-node iso-parametric element [4]

The shape functions in Eqn. 2.4.12 can be expanded to find the surface shape functions N^S for the element as shown in Figure 2.18, with Eqn. 2.4.13.

$$
N_{ij}^S(\xi, \eta) = \sum_{i=1}^{3} \sum_{j=1}^{3} N_j^L(\xi) N_i^L(\eta) \tag{2.4.13}
$$

The relation between the surface nodal shape functions, the hierarchical numbering $N_{ij}^S(\xi,\eta)$, and the node shape functions N_k^S is found by comparing Figure 2.18 to 2.19. The ξ and η represent the coordinates in the natural coordinate system.

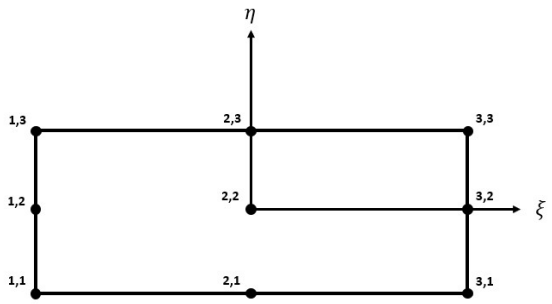

Figure 2.19: A 9-node iso-parametric element with the surface shape function as a combination of the line shape functions

This results in the following nodal shape functions for a 9-node surface element:

$$
\begin{aligned}
N_1 = N_{1,1} &= \frac{\xi(\xi-1)}{2}\frac{\eta(\eta-1)}{2} \\
N_2 = N_{3,1} &= \frac{\xi(\xi+1)}{2}\frac{\eta(\eta-1)}{2} \\
N_3 = N_{3,3} &= \frac{\xi(\xi+1)}{2}\frac{(\eta+1)(\eta)}{2} \\
N_4 = N_{1,3} &= \frac{\xi(\xi-1)}{2}\frac{(\eta+1)(\eta)}{2} \\
N_5 = N_{2,1} &= -(\xi+1)(\xi-1)\frac{\eta(\eta-1)}{2} \\
N_6 = N_{3,2} &= -\frac{(\xi+1)(\xi)}{2}(\eta+1)(\eta-1) \\
N_7 = N_{2,3} &= -(\xi+1)(\xi-1)\frac{(\eta+1)(\eta)}{2} \\
N_8 = N_{1,2} &= -\frac{\xi(\xi-1)}{2}(\eta+1)(\eta-1) \\
N_9 = N_{2,2} &= (\xi+1)(\xi-1)(\eta+1)(\eta-1)
\end{aligned}
\tag{2.4.14}
$$

Similarly, the nodal volume shape functions can be derived. The node numbers are given in Figure 2.20. The shape functions are defined by Eqn. 2.4.15.

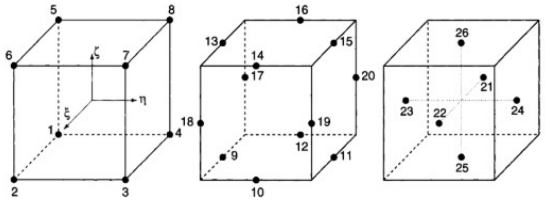

Figure 2.20: A 27-node iso-parametric element

$$N_{ijk}^{V} = \sum_{i=1}^{3}\sum_{j=1}^{3}\sum_{k=1}^{3} N_j(\xi)N_i(\eta)N_k(\zeta) \tag{2.4.15}$$

For a 27-node volume element, the nodal shape functions are presented in Eqns. 2.4.16 2.4.17, 2.4.20 and 2.4.23.

$$N_i^V = \frac{1}{8}\left(1+\xi_i\xi\right)\left(1+\eta_i\eta\right)\left(1+\zeta_i\zeta\right), \quad i = 1...8 \tag{2.4.16}$$

$$N_i^V = \frac{1}{4}\left(1-\xi^2\right)\left(1+\eta_i\eta\right)\left(1+\zeta_i\zeta\right), \quad i = 9,\ 11,\ 13,\ 15 \tag{2.4.17}$$

$$N_i^V = \frac{1}{4}\left(1+\xi_i\xi\right)\left(1-\eta^2\right)\left(1+\zeta_i\zeta\right), \quad i = 10,\ 12,\ 14,\ 16 \tag{2.4.18}$$

$$N_i^V = \frac{1}{4}\left(1+\xi_i\xi\right)\left(1+\eta_i\eta\right)\left(1-\zeta^2\right), \quad i = 17,\ 18,\ 19,\ 20 \tag{2.4.19}$$

$$N_i^V = \frac{1}{2}\left(1+\xi_i\xi\right)\left(1-\eta^2\right)\left(1-\zeta^2\right), \quad i = 21,\ 22 \tag{2.4.20}$$

$$N_i^V = \frac{1}{2}\left(1-\xi^2\right)\left(1+\eta_i\eta\right)\left(1-\zeta^2\right), \quad i = 23,\ 24 \tag{2.4.21}$$

$$N_i^V = \frac{1}{2}\left(1-\xi^2\right)\left(1-\eta^2\right)\left(1+\zeta_i\zeta\right), \quad i = 25,\ 26 \tag{2.4.22}$$

$$N_i^V = \left(1-\xi^2\right)\left(1-\eta^2\right)\left(1-\zeta^2\right), \quad i = 27 \tag{2.4.23}$$

In the next section, the edge shape functions for a p-order hexahedron will be derived. For a second-order element, there is a total of 54 edges. 18 edge shape equations are orientated in each of the three directions ξ, η and ζ, which are shown in Eqns. 2.4.24, 2.4.25 and 2.4.26 respectively. These are sourced from Jin [57] page 289.

$$N_{ijk}^{\xi,p+1} = \alpha_{ijk}^{\xi,p+1} \prod_{i'=1,\ i'\neq i}^{p+1} (\xi - \xi_{i'}) \prod_{j'=0,\ j'\neq j}^{p+1} (\eta - \eta_{j'}) \prod_{k'=0,\ k'\neq k}^{p+1} (\zeta - \zeta_{k'})\, \vec{\nabla}\xi \qquad (2.4.24)$$

$$i = 1, 2, ..., p+1; \quad j = 0, 1, ..., p+1 \quad k = 0, 1, ..., p+1$$

$$N_{ijk}^{\eta,p+1} = \alpha_{ijk}^{\eta,p+1} \prod_{i'=0,\ i'\neq i}^{p+1} (\xi - \xi_{i'}) \prod_{j'=1,\ j'\neq j}^{p+1} (\eta - \eta_{j'}) \prod_{k'=0,\ k'\neq k}^{p+1} (\zeta - \zeta_{k'})\, \vec{\nabla}\eta \qquad (2.4.25)$$

$$i = 0, 1, ..., p+1; \quad j = 1, 2, ..., p+1 \quad k = 0, 1, ..., p+1$$

$$N_{ijk}^{\zeta,p+1} = \alpha_{ijk}^{\zeta,p+1} \prod_{i'=0,\ i'\neq i}^{p+1} (\xi - \xi_{i'}) \prod_{j'=0,\ j'\neq j}^{p+1} (\eta - \eta_{j'}) \prod_{k'=1,\ k'\neq k}^{p+1} (\zeta - \zeta_{k'})\, \vec{\nabla}\zeta \qquad (2.4.26)$$

$$i = 0, 1, ..., p+1; \quad j = 1, 2, ..., p+1 \quad k = 0, 1, ..., p+1$$

In these equations, the variable α represents the normalization factor which is defined such that $|N_{ijk}| = 1$ if $\xi = \xi_i$, $\eta = \eta_j$ and $\zeta = \zeta_k$. The $\vec{\nabla}\xi$ denotes the gradient matrix in the represented natural coordinate (see equation 2.4.5) w.r.t. the global coordinate system, also known as the Jacobian for ξ. Now, the mapping from i, j and k to the mapping as shown in Figure 2.20 is as displayed in table 2.1, table 2.2 and table 2.3 below for the directions ξ, η and ζ respectively. A visual representation of the numbering scheme is shown in Figure 2.21.

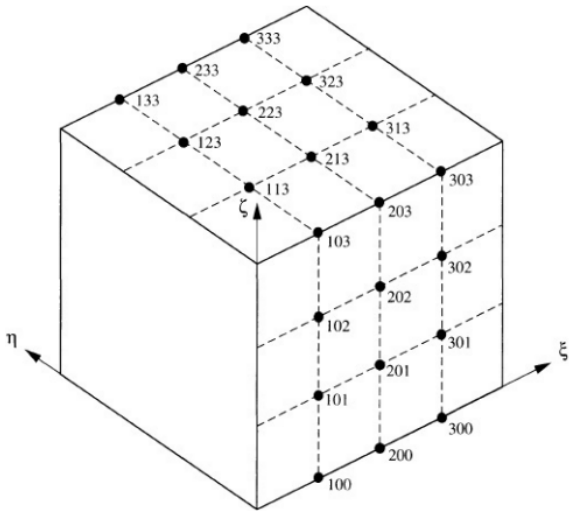

Figure 2.21: Example numbering scheme for interpolatory third order edge basis functions on a hexahedral

Table 2.1: Edge numbers, numbers and the code ijk for the shape functions in ξ direction for equation (2.4.24)

Edge number	Nodes	i, j, k code
1	$1 \to 9$	$(2, 1, 1)$
2	$9 \to 2$	$(3, 1, 1)$
3	$12 \to 25$	$(2, 2, 1)$
4	$25 \to 10$	$(3, 2, 1)$
5	$4 \to 11$	$(3, 2, 1)$
6	$11 \to 3$	$(3, 3, 1)$
7	$17 \to 23$	$(2, 1, 2)$
8	$23 \to 18$	$(3, 1, 2)$
9	$21 \to 27$	$(2, 2, 2)$
10	$27 \to 22$	$(3, 2, 2)$
11	$20 \to 24$	$(2, 3, 2)$
12	$24 \to 19$	$(3, 3, 2)$
13	$5 \to 13$	$(2, 1, 3)$
14	$13 \to 6$	$(3, 1, 3)$
15	$16 \to 26$	$(2, 2, 3)$
16	$26 \to 14$	$(3, 2, 3)$
17	$8 \to 15$	$(2, 3, 3)$
18	$15 \to 7$	$(3, 3, 3)$

Table 2.2: Edge numbers, node numbers and the code ijk for the shape functions in η direction for equation (2.4.25)

Edge number	Nodes	i, j, k code
19	$1 \rightarrow 12$	$(1, 2, 1)$
20	$12 \rightarrow 4$	$(1, 3, 1)$
21	$9 \rightarrow 25$	$(2, 2, 1)$
22	$25 \rightarrow 9$	$(2, 3, 1)$
23	$2 \rightarrow 10$	$(3, 2, 1)$
24	$10 \rightarrow 3$	$(3, 3, 1)$
25	$17 \rightarrow 21$	$(2, 1, 2)$
26	$21 \rightarrow 20$	$(3, 1, 2)$
27	$23 \rightarrow 27$	$(2, 2, 2)$
28	$27 \rightarrow 24$	$(3, 2, 2)$
29	$18 \rightarrow 22$	$(2, 3, 2)$
30	$22 \rightarrow 19$	$(3, 3, 2)$
31	$5 \rightarrow 16$	$(2, 1, 3)$
32	$16 \rightarrow 8$	$(3, 1, 3)$
33	$13 \rightarrow 26$	$(2, 2, 3)$
34	$26 \rightarrow 15$	$(3, 2, 3)$
35	$6 \rightarrow 14$	$(2, 3, 3)$
36	$14 \rightarrow 7$	$(3, 3, 3)$

2.4.4 First Order Tetrahedral Elements

Another type of element discussed is the family of tetrahedral elements. In this section, the shape functions that govern this element will be presented. These are sourced from Miyata [54], Zienkiewicz [13] and Pilkey and Wunderlich [4]. Aside from the shape functions on the tetrahedral elements, the shape functions for the triangular surfaces are required as well. The element geometry of the 2D and 3D triangular and tetrahedral elements and their nodes are shown in Figure 2.22.

Table 2.3: Edge numbers, node numbers and the code ijk for the shape functions in ζ direction for equation (2.4.26)

Edge number	Nodes	i, j, k code
37	$1 \rightarrow 17$	$(1, 1, 2)$
38	$17 \rightarrow 5$	$(1, 1, 3)$
39	$9 \rightarrow 23$	$(2, 1, 2)$
40	$23 \rightarrow 13$	$(2, 1, 3)$
41	$2 \rightarrow 18$	$(3, 1, 2)$
42	$18 \rightarrow 6$	$(3, 1, 3)$
43	$12 \rightarrow 21$	$(1, 2, 2)$
44	$21 \rightarrow 16$	$(1, 2, 3)$
45	$25 \rightarrow 27$	$(2, 2, 2)$
46	$27 \rightarrow 26$	$(2, 2, 3)$
47	$10 \rightarrow 22$	$(2, 2, 2)$
48	$22 \rightarrow 14$	$(3, 2, 3)$
49	$4 \rightarrow 20$	$(1, 3, 2)$
50	$20 \rightarrow 8$	$(1, 3, 3)$
51	$11 \rightarrow 24$	$(2, 3, 2)$
52	$24 \rightarrow 15$	$(2, 3, 3)$
53	$3 \rightarrow 19$	$(3, 3, 2)$
54	$19 \rightarrow 7$	$(3, 3, 3)$

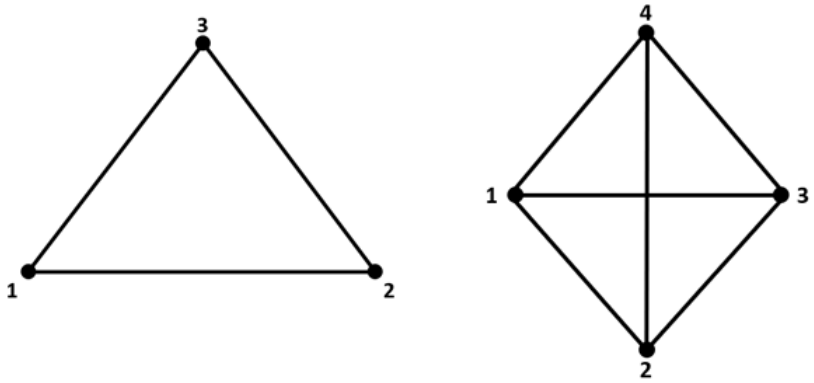

(a) 3 Node triangle (b) 4 Node tetrahedron

Figure 2.22: The node numbering schemes for the surface and volume of triangular and tetrahedral elements.

The equations for the nodal shape functions can be derived using Eqn. 2.4.27.

$$\vec{N}^v = \boldsymbol{N}_{\boldsymbol{u}}^{-1} \vec{X} \tag{2.4.27}$$

This equation can be employed to find both the shape functions for a triangular surface through Eqn. 2.4.28.

$$N^n = \begin{bmatrix} \lambda_1^t \\ \lambda_2^t \\ \lambda_3^t \end{bmatrix}, \quad N_u = \begin{bmatrix} 1 & 1 & 1 \\ x_1 & x_2 & x_3 \\ y_1 & y_2 & y_3 \end{bmatrix}, \quad X = \begin{bmatrix} 1 \\ x \\ y \end{bmatrix} \tag{2.4.28}$$

The variables, defined as shown in Eqn. 2.4.29, allow the derivation of the shape function for the tetrahedral surface element.

$$N^v = \begin{bmatrix} \lambda_1^v \\ \lambda_2^v \\ \lambda_3^v \\ \lambda_4^v \end{bmatrix}, \quad N_u = \begin{bmatrix} 1 & 1 & 1 & 1 \\ x_1 & x_2 & x_3 & x_4 \\ y_1 & y_2 & y_3 & y_4 \\ z_1 & z_2 & z_3 & z_4 \end{bmatrix}, \quad X = \begin{bmatrix} 1 \\ x \\ y \\ z \end{bmatrix} \tag{2.4.29}$$

These equations yield the relation between the global coordinate system, the area coordinates λ_i^t, and the volume coordinates λ_i^v. The volume and triangle coordinates are equal to the shape functions, $N_i = \lambda_i$. The edge shape functions of a tetrahedral can be found with Eqn 2.4.30 [58]:

$$\vec{N}_{ij}^e = \lambda_i \vec{\nabla} \lambda_j - \lambda_j \vec{\nabla} \lambda_i \tag{2.4.30}$$

Where i and j are the starting and ending nodes of the edge and the direction of the edge is from i to j

Alternatively, through Miyata [54]:

$$N_i = \boldsymbol{G} \begin{bmatrix} (\delta_2^i \lambda_3 - \delta_3^i \lambda_2) - \delta_4^i \left(\lambda_s^i + \lambda_1^i \lambda_4\right) \\ (\delta_3^i \lambda_1 - \delta_1^i \lambda_3) - \delta_4^i \left(\lambda_s^i + \lambda_2^i \lambda_4\right) \\ (\delta_1^i \lambda_2 - \delta_2^i \lambda_1) - \delta_4^i \left(\lambda_s^i + \lambda_3^i \lambda_4\right) \end{bmatrix} \tag{2.4.31}$$

With $\boldsymbol{G}$ being the gradient matrix, as presented in Appendix A. The δ variables

are defined by:

$$\delta_1^i = 4\lambda_2^i\lambda_3^i, \quad \delta_2^i = 4\lambda_3^i\lambda_1^i, \quad \delta_3^i = 4\lambda_1^i\lambda_2^i, \quad \delta_4^i = 1 - \left(\delta_1^i + \delta_2^i + \delta_3^i\right) \tag{2.4.32}$$

The variables λ_s^i are defined by:

$$\lambda_s^i = \lambda_1^i\lambda_1 + \lambda_2^i\lambda_2 + \lambda_3^i\lambda_3 \tag{2.4.33}$$

The δ values can be found through:

$$\delta_1^i = 4\lambda_2^i\lambda_3^i, \quad \delta_2^i = 4\lambda_3^i\lambda_1^i, \quad \delta_3^i = 4\lambda_1^i\lambda_2^i, \quad \delta_4^i = 1 - \left(\delta_1^i + \delta_2^i + \delta_3^i\right) \tag{2.4.34}$$

The variables λ^i are defined as shown in Table 2.4.

Table 2.4: The λ_1^i, λ_2^i and λ_3^i values for the 6 different edges.

Edge number	λ_1^i	λ_2^i	λ_3^i
1	0	$\frac{1}{2}$	$\frac{1}{2}$
2	$\frac{1}{2}$	0	$\frac{1}{2}$
3	$\frac{1}{2}$	$\frac{1}{2}$	0
4	1	0	0
5	0	1	0
6	0	0	1

Chapter 3

Implementation of new elements

The implementation of the element formulation discussed in Chapter 2 is elaborated upon here. First, the implementation of the 8-node hexahedral element is examined in Section 3.1. The 8-node hexahedral element was needed to model curved surfaces. Second, in Section 3.2, the 4-node tetrahedral element implementation is elaborated upon. Tetrahedral elements are better suited to model curved structures, but require more elements to achieve the same accuracy when compared to hexahedral elements. Third, in Section 3.3, the implementation of higher order elements is discussed. In Sections 3.4 and Section 3.5 reduced complexity second order elements are proposed and in Section 3.6 some of the discovered inaccuracies are evaluated, and a solution is proposed.

3.1 Implementation of the 8-node Hexahedral Element

A 4-node iso-parametric quadrilateral and an 8-node iso-parametric hexahedral element are displayed in Figure 3.1.

The shape functions for the element are as described in Subsection 2.4.1. Eqn. 3.1.1 describes the nodal shape functions for the quadrilateral surface element on a hexahedral volume element.

$$N_i = \frac{1}{4}\left(1 + \xi\xi_i\right)\left(1 + \eta\eta_i\right) \tag{3.1.1}$$

In this equation, N_i represents the nodal shape function of node i, ξ and η are the

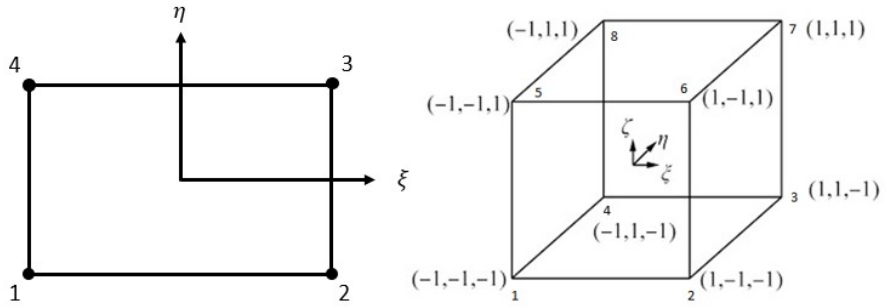

Figure 3.1: The nodes of a 4-node surface element (left) and an 8-node volume element (right)

natural coordinates, and the location of node i is given by ξ_i and η_i. In Eqn. 3.1.2, the shape functions for the hexahedral element are presented.

$$N_i = \frac{1}{8}\left(1+\xi\xi_i\right)\left(1+\eta\eta_i\right)\left(1+\zeta\zeta_i\right) \tag{3.1.2}$$

In this equation, the natural coordinate ζ is added. Eqn. 3.1.3 presents the edge shape functions in the three directions of the natural coordinate system. Here, N_p are the shape functions of the edges, and p represents the edge number.

$$\begin{aligned} N_p &= \frac{1}{8}\left(1+\eta\eta_p\right)\left(1+\zeta\zeta_p\right)\vec{\nabla}\xi \\ N_p &= \frac{1}{8}\left(1+\zeta\zeta_p\right)\left(1+\zeta\zeta_p\right)\vec{\nabla}\eta \\ N_p &= \frac{1}{8}\left(1+\eta\eta_p\right)\left(1+\xi\xi_p\right)\vec{\nabla}\zeta \end{aligned} \tag{3.1.3}$$

The term $\vec{\nabla}\xi$ is as defined in Eqn. 2.4.5. The rotation of the shape function is required to calculate the contributions to the $\boldsymbol{N}$ matrix, as shown in Eqn. 2.3.59. The rotation (or curl) of the edge shape functions is given by Eqn. 3.1.4 [54].

$$\vec{\nabla} \times \vec{N}_p = \frac{\boldsymbol{J}}{8J} \begin{bmatrix} \left(1 + \vec{\xi_p}\xi\right)\left(\vec{\eta_p}\delta_{\zeta p} - \vec{\zeta_p}\delta_{\eta p}\right) \\ \left(1 + \vec{\eta_p}\eta\right)\left(\vec{\zeta_p}\delta_{\xi p} - \vec{\xi_p}\delta_{\zeta p}\right) \\ \left(1 + \vec{\zeta_p}\zeta\right)\left(\vec{\xi_p}\delta_{\eta p} - \vec{\eta_p}\delta_{\xi p}\right) \end{bmatrix} \tag{3.1.4}$$

Here, J is the determinant of the Jacobian, and $\mathbf{J}$ is the Jacobian matrix. The values for the variable δ are found by the following equations [54]:

$$\delta_{\xi p} = |\eta_p \zeta_p|, \quad \delta_{\eta p} = |\xi_p \zeta_p|, \quad \delta_{\zeta p} = |\eta_p \xi_p| \tag{3.1.5}$$

The shape functions are based on an iso-parametric element in the natural coordinate system. The volume and surface nodal shape functions then map the resulting functions for the electromagnetic equations to the global coordinate system. To achieve this, linear shape functions transform the electromagnetic functions from the global coordinate system to the natural coordinate system. In the natural coordinate system, the boundaries of integration are always from -1 to 1. An example of how the matrices discussed are derived for the 8-20 element introduced in the next section is shown in Appendix E.

3.1.1 Implementation of the $\boldsymbol{M}$ and $\boldsymbol{N}$ matrices

The equations for the $\boldsymbol{M}$ and $\boldsymbol{N}$ matrices are given in Eqns. 2.3.59 and 2.3.58, as presented by Bossavit [10]. The volume integrals over Ω_c have -1 and 1 as their limits, since the shape functions are defined on the natural coordinate system. The gradient, that is required for the definition of the $\boldsymbol{M}$ matrix, as a function of the nodal shape function, is found and presented in Eqn 3.1.6. For more a derivation of the gradient, see Appendix A.

$$\vec{\nabla}\vec{N} = \begin{bmatrix} \frac{\partial \vec{N}_i}{\partial x} \\ \frac{\partial \vec{N}_i}{\partial y} \\ \frac{\partial \vec{N}_i}{\partial z} \end{bmatrix} = \boldsymbol{J^{-1}} \begin{bmatrix} \frac{\partial \vec{N}_i}{\partial \xi} \\ \frac{\partial \vec{N}_i}{\partial \eta} \\ \frac{\partial \vec{N}_i}{\partial \zeta} \end{bmatrix} \tag{3.1.6}$$

The equations for the curl (in Eqn. 3.1.4) and gradient (in Eqn. 3.1.6) are required for the $\boldsymbol{M^a}$ and $\boldsymbol{N^a}$ matrices. Minimal adaption of the formulation of these matrices is required. The $\boldsymbol{N^a}$ matrix, as presented in Eqn. 2.3.59, only requires an adaption by substituting in Eqn. 3.1.4. This results in Eqn. 3.1.7. In this equation, the electrical conductivity $\boldsymbol{\sigma}$ is assumed to be constant and can be taken outside the integration, i.e., it is not a function of $\vec{x}$ as this is a constant within the element a.

$$\vec{N}^a_{kl} = \boldsymbol{\sigma}_a^{-1} \iiint_{\Omega_c} \left(\begin{bmatrix} \left(1 + \vec{\xi}_k \xi\right)\left(\vec{\eta}_k \delta_{\zeta k} - \vec{\zeta}_k \delta_{\eta k}\right) \\ \left(1 + \vec{\eta}_k \eta\right)\left(\vec{\zeta}_k \delta_{\xi k} - \vec{\xi}_k \delta_{\zeta k}\right) \\ \left(1 + \vec{\zeta}_k \zeta\right)\left(\vec{\xi}_k \delta_{\eta k} - \vec{\eta}_k \delta_{\xi k}\right) \end{bmatrix} \right) \cdot \left(\begin{bmatrix} \left(1 + \vec{\xi}_l \xi\right)\left(\vec{\eta}_l \delta_{\zeta l} - \vec{\zeta}_l \delta_{\eta l}\right) \\ \left(1 + \vec{\eta}_l \eta\right)\left(\vec{\zeta}_l \delta_{\xi l} - \vec{\xi}_l \delta_{\zeta l}\right) \\ \left(1 + \vec{\zeta}_l \zeta\right)\left(\vec{\xi}_l \delta_{\eta l} - \vec{\eta}_l \delta_{\xi l}\right) \end{bmatrix} \right) \, dV \tag{3.1.7}$$

For the $\boldsymbol{M^a}$ matrix, Eqn. 3.1.6 is substituted in Eqn. 2.3.58, resulting in

$$\begin{aligned} M^a_{kl} &= \mu_a \iiint_{\Omega_a} \vec{N}_k \cdot \vec{N}_l \, dV \\ M^a_{ik} = M^a_{ki} &= \mu_a \iiint_{\Omega_a} \left(\boldsymbol{J^{-1}} \begin{bmatrix} \frac{\partial \vec{N}_i}{\partial \xi} \\ \frac{\partial \vec{N}_i}{\partial \eta} \\ \frac{\partial \vec{N}_i}{\partial \zeta} \end{bmatrix} \right) \cdot \vec{N}_k \, dV \\ M^a_{ij} &= \mu_a \iiint_{\Omega_a} \left(\boldsymbol{J^{-1}} \begin{bmatrix} \frac{\partial \vec{N}_i}{\partial \xi} \\ \frac{\partial \vec{N}_i}{\partial \eta} \\ \frac{\partial \vec{N}_i}{\partial \zeta} \end{bmatrix} \right) \cdot \left(\boldsymbol{J^{-1}} \begin{bmatrix} \frac{\partial \vec{N}_j}{\partial \xi} \\ \frac{\partial \vec{N}_j}{\partial \eta} \\ \frac{\partial \vec{N}_j}{\partial \zeta} \end{bmatrix} \right) \, dV \end{aligned} \tag{3.1.8}$$

Symbolic integration of Eqns. 3.1.7 and 3.1.8 did not yield a solution due to the

complex nature of the equations. Therefore, a numerical integration scheme was used to evaluate the integral. Different numerical integration schemes were utilized to determine the best solution and least computational effort; the integration schemes used were: Simpson's rule, Simpson's 3/8th rule, and the closed Newton-Cotes formula with 4 nodes [59]. Gaussian Quadrature with 1, 2, 3 and 4 integration points was also considered.

When comparing the numerically integrated 8-node hexahedral functions to the cubic 2-node functions that were symbolically integrated, the ones currently implemented in WelDone, no difference is expected when comparing the $\boldsymbol{M}^a$ and $\boldsymbol{N}^a$ matrices for the same element. To validate the implementation of the 8-node hexahedral element, the $\boldsymbol{M}^a$ and $\boldsymbol{N}^a$ matrices of the different numerical implementations are compared to that of the symbolic derivation. When comparing the Gaussian Quadrature with 1 node numerical integration for a sample brick shaped hexahedral element, errors with a magnitude of 12.5% to 125% are observed, see Appendix C. The solution has errors in the domain of machine errors when applying Simpson's rule for numerical integration. The results of this endeavor are presented in Appendix C. Since Simpson's rule is the least resource intensive integration scheme, it is applied to find the $\boldsymbol{M}^a$ and $\boldsymbol{N}^a$ matrices.

3.1.2 Implementation of the Poincare operator

To find the equations that transform the Dirichlet boundary conditions to Neumann boundary conditions, Eqns. 2.3.62, 2.3.63 and 2.3.64 are employed, for reference see Subsection 2.3.4. These equations are the general equations and can be simplified to fit the formulation of the quadrilateral element to which they are applied. Note, as a simplification, the term $||\vec{y} - \vec{x}||$ is replaced by $\vec{r}_{xy}$ in Eqns 3.1.10 and 3.1.11.

$$\boldsymbol{B}_e^{\boldsymbol{a}} = \zeta_a \int_{-1}^{1} \int_{-1}^{1} N_i(\vec{x})\ d\vec{x} \tag{3.1.9}$$

The variables ζ_a and ζ_b are constants [10] and thus can be taken out of the integral. In this equation, a and b are the indices of the two elements evaluated as discussed in Section 2.3.4.

$$\boldsymbol{K_e^a} = \frac{\zeta_a \zeta_b}{4\pi} \int_{-1}^{1} \int_{-1}^{1} \left(\int_{-1}^{1} \int_{-1}^{1} \frac{1}{\vec{r}_{xy}} \, d\vec{x} \right) d\vec{y} \tag{3.1.10}$$

Similarly, the $\boldsymbol{H}$ matrix as given in Eqn. 2.3.64 can be rewritten:

$$\boldsymbol{H_e^a} = \frac{\zeta_a}{4\pi} \int_{-1}^{1} \int_{-1}^{1} \left(\vec{N}_e(\vec{x}) \int_{-1}^{1} \int_{-1}^{1} \frac{(\hat{n}_b \cdot (\vec{y} - \vec{x}))}{\vec{r}_{xy}^3} \, d\vec{y} \right) d\vec{x} \tag{3.1.11}$$

Here, $\hat{n}_b$ is the unit normal vector associated with the surface of element b. The nodal shape function is dependent exclusively on the variables $\vec{x}$, thus they can be moved outside the first surface integral. When numerically integrating these equations through Gauss' quadrature, as described in Holland [1], some erroneous results are produced. The details of these errors will be elaborated upon in Section 3.6. An example of how the matrices discussed are derived is shown in Appendix E.

3.2 Implementation of the 4-node Tetrahedral Element

To find the element matrices $\boldsymbol{M}^a$ and $\boldsymbol{N}^a$ for the tetrahedral element, as presented in Figures 3.2a and 3.2b, the curl of the nodal shape functions is required.

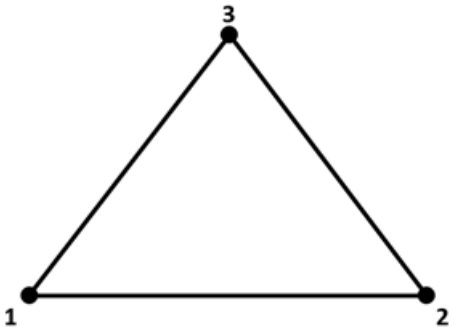

(a) 3 Node triangle

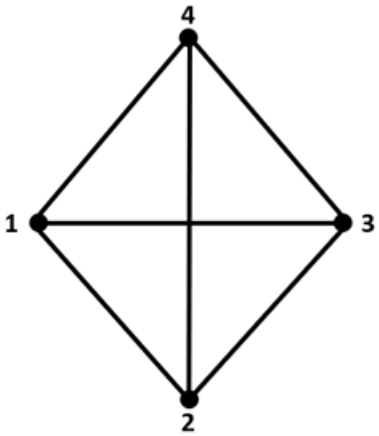

(b) 4 Node tetrahedron

The equation for the curl in the volume coordinates of a tetrahedral element is presented in Eqn. 3.2.1.

$$\vec{\nabla} \times \vec{N} = \frac{2\boldsymbol{J}}{J} \begin{bmatrix} (\delta_1^i + \delta_4^i (\lambda_3^i - \lambda_2^i) \\ (\delta_2^i + \delta_4^i (\lambda_1^i - \lambda_3^i) \\ (\delta_3^i + \delta_4^i (\lambda_2^i - \lambda_1^i) \end{bmatrix} \tag{3.2.1}$$

The λ^i's in this equation are presented in Table 2.4, J is the determinant of the Jacobian matrix while $\boldsymbol{J}$ is the Jacobian matrix. The δ variables are defined by:

$$\delta_1^i = 4\lambda_2^i\lambda_3^i, \quad \delta_2^i = 4\lambda_3^i\lambda_1^i, \quad \delta_3^i = 4\lambda_1^i\lambda_2^i, \quad \delta_4^i = 1 - \left(\delta_1^i + \delta_2^i + \delta_3^i\right) \tag{3.2.2}$$

With these equations, the integrals in the equations for the $\boldsymbol{M}^a$ and $\boldsymbol{N}^a$ matrices still need to be rewritten for a 4-node tetrahedron volume, as will be shown in Subsection 3.2.1.

3.2.1 Implementation of the $\boldsymbol{M}^a$ and $\boldsymbol{N}^a$ matrices

The equations for the $\boldsymbol{M}^a$ and $\boldsymbol{N}^a$ matrices given in Eqn. 2.3.59 and 2.3.58 are modified to reflect that the integration is over a tetrahedral element with volume coordinates. For the $\boldsymbol{N}^a$ matrix, this yields:

$$\boldsymbol{N}_{kl}^a = \boldsymbol{\sigma}^{-1} \int_0^1 \int_0^{1-\lambda_1} \int_0^{1-\lambda_1-\lambda_2} \left(\left(\vec{\nabla} \times \vec{N}_k\right)\right) \cdot \left(\vec{\nabla} \times \vec{N}_l\right) \, d\lambda_3 \, d\lambda_2 \, d\lambda_1 \tag{3.2.3}$$

Similarly, the integrals for the $\boldsymbol{M}^a$ matrices can be rewritten, this yields:

$$\boldsymbol{M}^a_{kl} = \mu_a \int_0^1 \int_0^{1-\lambda_1} \int_0^{1-\lambda_1-\lambda_2} \vec{N}_k \cdot \vec{N}_l \; d\lambda_3 \; d\lambda_2 \; d\lambda_1,$$

for edges k and l on element a (3.2.4)

$$\boldsymbol{M}^a_{ik} = \boldsymbol{M}^a_{en} = \mu_a \int_0^1 \int_0^{1-\lambda_1} \int_0^{1-\lambda_1-\lambda_2} \left(\vec{\nabla}\vec{N}_i\right) \cdot \vec{N}_k \; d\lambda_3 \; d\lambda_2 \; d\lambda_1,$$

for edge k and node i on element a (3.2.5)

$$\boldsymbol{M}^a_{ij} = \mu_a \int_0^1 \int_0^{1-\lambda_1} \int_0^{1-\lambda_1-\lambda_2} \left(\vec{\nabla}\vec{N}_i\right) \cdot \left(\vec{\nabla}\vec{N}_j\right) \; d\lambda_3 \; d\lambda_2 \; d\lambda_1,$$

for nodes i, j on element a (3.2.6)

The integration of these equations was performed symbolically. Some difficulties may arise when implementing these in a finite element setting. These difficulties are discussed in Appendix D as the dissertation does not continue the implementation of the tetrahedral elements.

3.2.2 Implementation of the Poincare operator

Similar to how the equations that transform the Dirichlet boundary conditions to Neumann boundary conditions are adapted for the quadrilateral element in Subsection 3.1.2, the integration is re-written for the triangular elements with the volume coordinates λ_1 and λ_2 for triangular surface a and γ_1 and γ_2 for triangular surface b.

$$\boldsymbol{B}^{\boldsymbol{a}}_{\boldsymbol{e}} = \zeta_a \int_0^1 \int_0^{1-\lambda_1} N_i(\vec{x}) \; d\lambda_2 \; d\lambda_1 \tag{3.2.7}$$

$$\boldsymbol{K_e^a} = \frac{\zeta_a \zeta_b}{4\pi} \int_0^1 \int_0^{1-\gamma_1} \left(\int_0^1 \int_0^{1-\lambda_1} \frac{1}{\vec{r}_{xy}} \, d\lambda_2 \, d\lambda_1 \right) d\gamma_1 d\gamma_2 \tag{3.2.8}$$

In a similar fashion, the $\boldsymbol{H}$ matrix as given in Eqn. 2.3.64 can be rewritten:

$$\boldsymbol{H_e^a} = \frac{\zeta_a}{4\pi} \int_0^1 \int_0^{1-\gamma_1} \left(\vec{N}_e(\vec{x}) \int_0^1 \int_0^{1-\lambda_1} \frac{(\hat{n}_b \cdot (\vec{y} - \vec{x}))}{\vec{r}_{xy}^3} \, d\lambda_2 \, d\lambda_1 d \right) \gamma_1 d\gamma_2 \tag{3.2.9}$$

3.3 Implementation of the 27-node Hexahedral Element

In this section, the 27-node hexahedral element is discussed. For brevity, this section points out the differences between the 8-node hexahedral element and the 27-node hexahedral element, as these are similar in the implementation.

3.3.1 Implementation of the M and N matrices

For the $\boldsymbol{M}^a$ and $\boldsymbol{N}^a$ matrices, the Eqns. as presented in section 3.1.1 can be used. The nodal shape functions N_i^a and edge shape functions $\vec{N}_l^a$ are altered to represent the shape functions of the 27-node hexahedral. The symbolic integration of these matrices was attempted, however similar to the 8-node element, the symbolic integration could not be completed. This is no surprise, as the shape functions in these equations are second order, and thus more complex than the shape functions of the 8-node hexahedral.

To find a solution, numerical integration is once more employed. The following numerical integration algorithms were considered:

1. Simpson's rule
2. Simpson's 3/8th rule
3. Gaussian quadrature with 1 integration point

4. Gaussian quadrature with 2 integration points

5. Gaussian quadrature with 3 integration points

6. Gaussian quadrature with 4 integration points

When developing the functions which contain numerically integrated equations for Eqns. the files created rapidly became too large to be useable (over $500MB$). Evaluating these function files in MATLAB is not viable, however as computing technology develops, this may become available in the future. To provide an alternative second order element, a modified second order hexahedral element is proposed in the next section. An example of how the matrices discussed are derived is shown in Appendix E.

3.4 The 8-20-node Hexahedral Element

In this section, a second order element of reduced complexity is proposed. In the previous section, a 27-node element was introduced. The functions for this element are too complex for the derivation of the $\boldsymbol{M}^a$ and $\boldsymbol{N}^a$ matrices in both numerical and symbolic form, therefore an 8-20-node hexahedral is proposed. This element is based on a 20-node serendipity element as presented by Zienkiewicz [55] and shown in Figure 3.3.

To reduce the number of variables in the equations describing the $\boldsymbol{M}$ and $\boldsymbol{N}$ matrices, a simplification is implemented. The location of the middle nodes, nodes 9 and up, are proposed to be fully defined by nodes 1 through 8 and therefore disappear from the element definition. For example: the coordinates of the 9^{th} node are defined as by Eqns. 3.4.1 through 3.4.3.

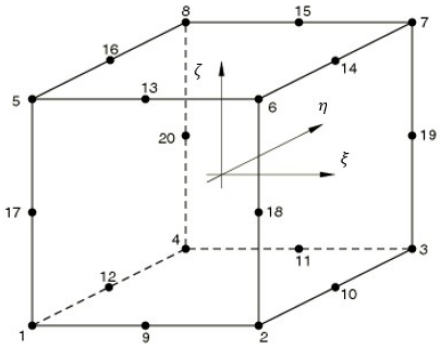

Figure 3.3: The 20-node iso-parametric hexahedral element

$$x_9 = \frac{x_1 + x_2}{2} \tag{3.4.1}$$

$$y_9 = \frac{y_1 + y_2}{2} \tag{3.4.2}$$

$$z_9 = \frac{z_1 + z_2}{2} \tag{3.4.3}$$

By defining the middle nodes in this fashion, the number of variables defining the geometry is reduced back to the same number (24) of variables as in the 8-node hexahedral. The shape functions however remain quadratic, thus the increase in fidelity of the unknowns is maintained. The downside of this simplification is that it does not increase the ability of the software to follow complex geometries as the shape of the element is defined by 8 nodes as opposed to 20 nodes, so all edges are straight lines. The element is geometrically the same as the 8-node hexahedral, however the shape functions are second order due to the mid-point node introduced. The shape functions for this element have been developed but not implemented. The MATLAB code for the derivation of this element is shown in Appendix E.

3.5 The 2-20-node Hexahedral Element

In this section, a second order element is proposed that is reduced in complexity beyond those proposed in Section 3.4. By reverting to the same scheme for the geometrical representation of the node, as in the brick element shown in Figure 1.2. The complexity of the element is reduced to an even greater extent, while retaining the capability of the element to provide a second order accuracy for the unknowns in the nodes and edges. The element matrices for this element, as shown in Section 3.3, are employed and, with the proposed geometrical constraints, are derived for both Gaussian and Newton-Cotes quadrature. The implementation of these was cut short due to the discovery of the numerical instability discussed in Section 3.6. An example of how the matrices discussed are derived for the 8-20 element introduced in the next section is shown in Appendix E. To make this example derive the 2-20 element matrices, the code must be altered in the lines 11, 12 and 13 to make the node locations a function of nodes 1 and 7, see Figure 1.2.

3.6 Curved Mesh Induced Errors and the Poincare Operator

The new functions for the $\boldsymbol{M}^a$ and $\boldsymbol{N}^a$ as derived in Section 3.1 replace the brick element functions. To verify the correct implementation of the new 8-noded hexahedrons, two meshes were evaluated with the previously developed 2-node hexahedral elements and the newly developed 8-noded hexahedral elements. The results from these analyses were identical. This confirmed that the 8-node hexahedrons were successfully implemented. The results of this implementation are shown in Section 5.1.

To leverage the new elements, a curved plate, shown in Figure 3.4 is introduced. Note, the curve is exaggerated due to the z-axis scaling. The curvature introduced only increases the height in the middle of the plate by 0.2 mm. The analysis resulted in an increase of the volumetric ohmic losses of 4 to 5 fold with respect to the flat

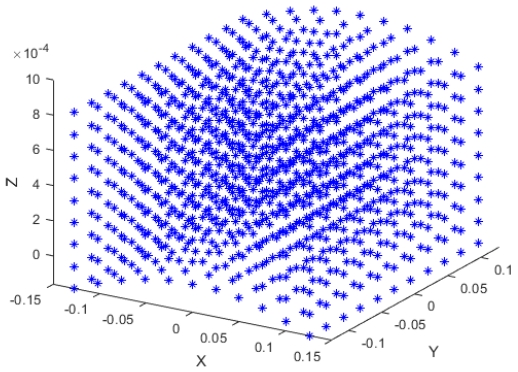

Figure 3.4: The curved plate

plate. The meshes that had curvature introduced showed a significant increase in the number of non-zero elements in the $\boldsymbol{H}$ matrix. Upon inspection, the code would assume that the contribution to the $\boldsymbol{H}$ is 0 if the surfaces are parallel. However, the contribution of any pair of surfaces to the $\boldsymbol{H}$ matrix is 0 if the surfaces are co-planar, not parallel. This error is found when evaluating curved geometries, as the opposing surfaces that were previously neglected are now added. For an in-depth explanation, please refer to Appendix F.

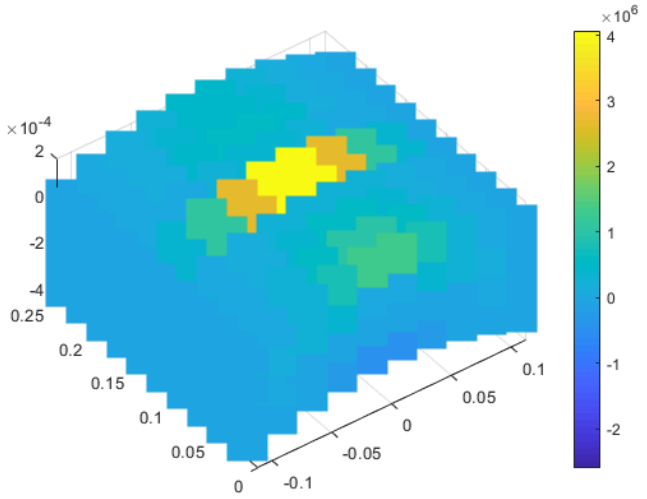

Figure 3.5: The difference in the ohmic loses between the flat and curved plate in J/s

In Figure 3.5, the difference in the heat generated between the flat plate and the

curved one is shown per element. Note that the largest discrepancy is in the middle of the plate, where the heating is most significant. The distribution of the heat is in line with the expectations based on the location of the coil and experiments. The pattern being the same, and in line with in-house experiments, indicates that during the process of solving the system of equations there is a term not related to the distribution of the currents that is erroneous. This erroneous term amplifies ohmic losses. Indicating that the term in question is likely to be the $\boldsymbol{P}$ matrix.

The values of the $\boldsymbol{H}$ matrix for the flat plate and the curved plate are expected to be different. However, with the small curvature introduced, the ohmic losses are not expected to change a factor 4 to 5. The integration of the $\boldsymbol{H}$ matrix is done through Gaussian quadrature. To see whether this manner of evaluating the integrals provides a sufficiently accurate result, the term inside the integrals of Eqn. 3.1.11 is evaluated. This term, as shown in Eqn. 3.6.1 is plotted as a function of the first variable of integration, ξ_x of which $\vec{r}_{xy}$ is a function.

$$H_{int} = \frac{(\hat{n}_b \cdot (\vec{y} - \vec{x}))}{\vec{r}_{xy}^{3}} \tag{3.6.1}$$

For an example case, Eqn. 3.6.1 is evaluated over two 1 inch by 1 inch square quadrilateral elements as shown in Figure 3.6. Note that $\vec{r}_{xy}$ is a function of ξ_x, ξ_y, η_x and, η_y which are the iso-parametric coordinates of the two surfaces shown in Figure 3.6. The choice of the orientation of the surfaces, as shown in this figure, is the worst case scenario. In this scenario, the singularity is the strongest, therefore if the solution is found for this case it will be sufficient for any other scenario.

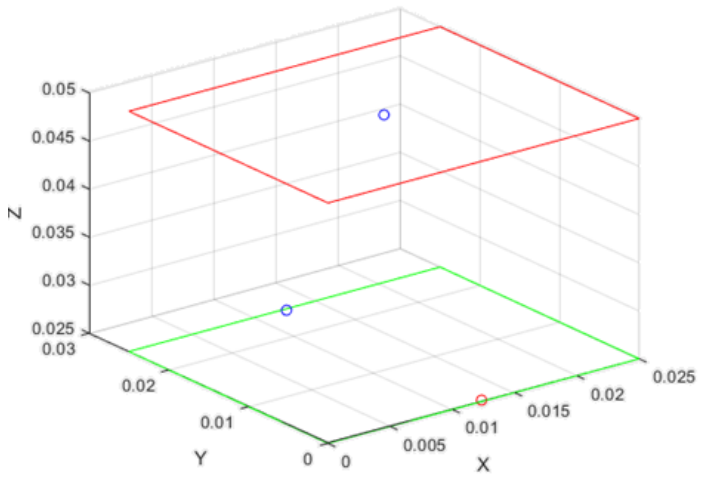

Figure 3.6: The two quadrilateral surfaces

To evaluate what happens in a thin conductive domain, or a laminate, as opposed to a thick structure, the distance between the two surfaces in the z-direction is varied. The results of Eqn. 3.6.1 is plotted against ξ_x, which represents the equation for H_{int} going from the red to the blue dot in Figure 3.6. The value for the integration variables, η_x, ξ_y and η_y, are assumed to be constant. This simplifies the example and allows for a two-dimensional plot, these variables are set at $\frac{1}{2}$ inch, the middle of the example surfaces. As such, the example represents one of the four integrals that is required to find the contribution of an element to the $\boldsymbol{H}$ matrix, see Figure 3.7. In Figure 3.7a the distance between the two surfaces is equal to the length of one of the sides of the rectangle, or 1 inch. In the second figure, Figure 3.7b, the distance between the surfaces is one tenth of the length of the side of the rectangle. In the last figure, Figure 3.7c, the distance between the two surfaces is one hundredth of an inch, or one hundredth of the side of the surface element.

From these figures, it becomes apparent that as the distance between the surfaces decreases, Eqn. 3.6.1 becomes more difficult to capture with a polynomial, and the equation starts looking more like a Dirac delta function. These cannot be numerically integrated with Gaussian Quadrature, as the polynomial shape functions are

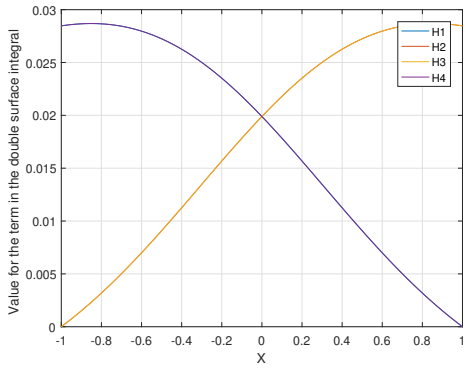

(a) H_{int} at a distance of the element length

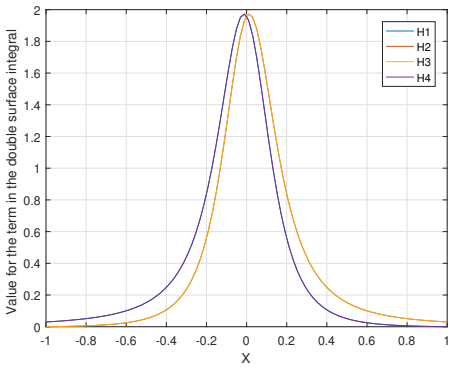

(b) H_{int} at a distance of 1/10th the element length

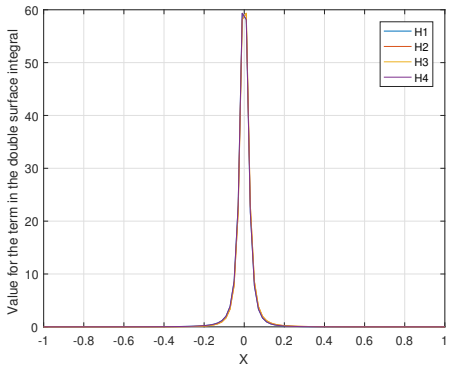

(c) H_{int} at a distance of 1/100th the element length

Figure 3.7: H_{int} at various distances between the two quadrilateral surfaces

unsuitable to capture the function shown in Figure 3.7c. Note that the scale of the y-axis between Figure 3.7b and 3.7c is significantly different. In conclusion, when evaluating a thin plate shaped mesh, the discretization must be small enough such that the function H_{int} as shown in Eqn. 3.6.1 can be represented by a polynomial, however when evaluating laminates this is likely not the case. In the next section, the requirement to achieve convergence on such a plate is discussed.

3.6.1 Convergence study on Cube and Plate

To confirm that the phenomenon discussed in the previous question causes the errors found when modelling a curved plate as presented at the start of this section, two

convergence studies were conducted. The first is conducted on a cube, shown in Figure 3.8a and the second study is conducted on a volume representing a plate, as shown in Figure 3.8b.

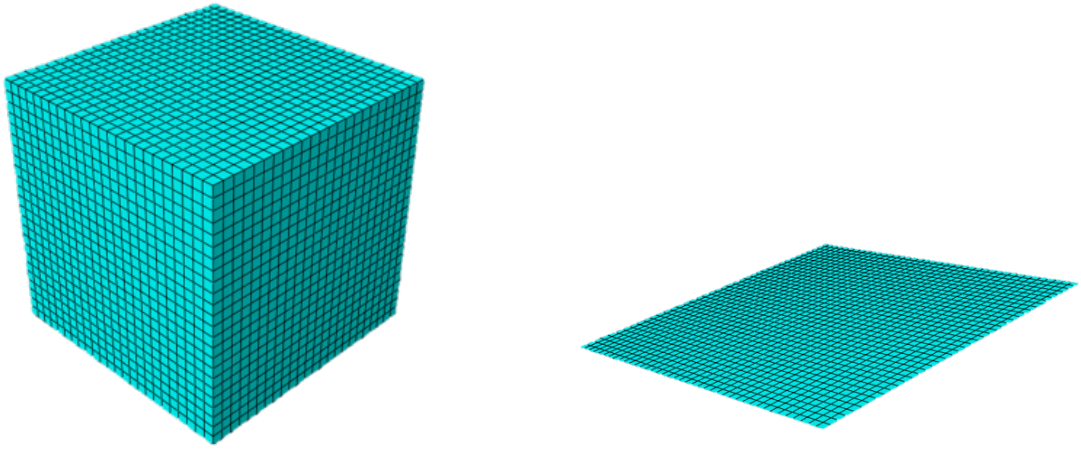

(a) Cube with example mesh employed in the convergence study

(b) Plate with example mesh employed in the convergence study

Figure 3.8: Two discretized volumes for which a mesh convergence study was attempted

It is expected that to represent the function H_{int} as a polynomial, the mesh representing the laminate will require a significant increase in the number of elements. The goal of this convergence study is to show convergence of the heat generated over the cube and plate as the number of elements increases. The expectation is that if the root of the problem is the $\boldsymbol{H}$ matrix as described previously, then the cube will converge. However, the plate will not converge.

Table 3.1: Results of the convergence study of the cube

Element Code	Number of Elements	$\dot{Q}_{total}$
5x5x4	100	0.05143
8x8x8	512	0.00805
10x10x8	800	0.00929
12x12x12	1,728	0.01031
16x16x16	4,096	0.01142
20x20x20	8,000	0.01216
24x24x24	13,824	0.01247

In Table 3.1 and 3.2, the element code column shows the number of elements that are applied to the volume in the x, y and z-direction. The $\dot{Q}_{total}$ is the total heat generated in the volume in $[J/s]$.

Table 3.2: Results of the convergence study of the plate

Element Code	Number of Elements	$\dot{Q}_{total}$
10x10x4	400	11.04
15x15x4	900	31.64
20x20x4	1,600	52.05
25x25x4	2,500	54.81
30x30x4	3,600	67.72
35x35x4	4,900	89.27
40x40x4	6,400	129.40
45x45x4	8,100	127.33
50x50x4	10,000	145.49

In the case of the plate, the number of elements through the thickness, the z-direction, is not increased as the size of the elements in the xz and yz plane are small with respect to the distance between the surfaces. The results given in the tables are visualized in Figures 3.9a and 3.9b.

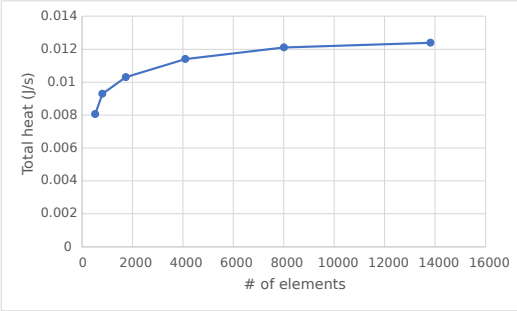

(a) Convergence of the cube as a function of the number of elements

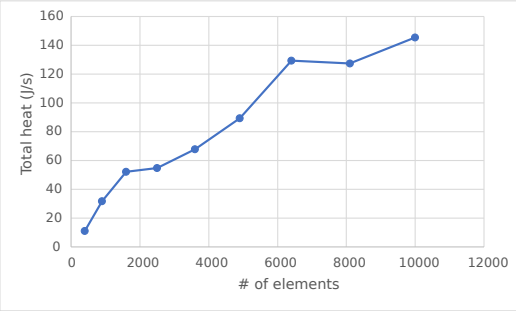

(b) Convergence of the plate as a function of the number of elements

Figure 3.9: Convergence as a function of the number of elements

In figure 3.9a it is shown that the heat generated converges as the mesh density is increased. In the case of the plate volume, convergence is not achieved, as shown

in Figure 3.9b. To evaluate these volumes, a significantly higher number of mesh elements are required.

If the model with element code "16x16x16" is considered converged, as shown in Table 3.1, the singularity issue could be avoided by selecting an element size that is $\frac{1}{16}$th of the plate thickness. Calculating the number of elements required on a thin plate results in the mesh bein prohibitively dense. Assuming a 30 cm by 30 cm plate consisting of 16 plies with a single ply thickness of 0.125 mm, results in a total laminate thickness of 2 mm. Through the thickness 16 elements are required, thus an element would have to be a cube with 0.125 mm sides. In the length and width directions, this would yield 2400 elements, resulting in a total of 92 million elements. The resulting mesh would require 100's of days to calculate with the cluster available to the researcher, and would therefore be computationally prohibitive.

3.7 Conclusion

In Section 3.1, the 8-node hexahedral element is introduced; implementation of this element is discussed and, although symbolic integration of the element matrices $\boldsymbol{M}^a$ and $\boldsymbol{N}^a$ is impossible, by applying Simpson's rule, the element matrices can be numerically integrated. In Section 3.2, thoughts on how the tetrahedral global matrices would be assembled are presented and the element matrices $\boldsymbol{M}^a$ and $\boldsymbol{N}^a$ are found through symbolic integration. The tetrahedral element matrices are symbolically derived, however these were not implemented. A 27-node hexahedral element was discussed and created in Section 3.3; the symbolic integration was impossible, and the numerical integration was too computationally expensive, this may change with the rapid development in computational power. To introduce a higher order element, the 8-20-node hexahedral element was proposed in Section 3.4. This element has a reduced number of variables defining the geometry, which reduces the computational resources required, and allows us to find a feasible solution with this element. The

element does not have curved edges, but will retain higher order shape functions for the variable that is discretized. The derivation of the element matrices $\boldsymbol{M}^a$ and $\boldsymbol{N}^a$ of this element is achieved with a 2-integration point Gaussian quadrature. The decoupling of the discretized variable and the geometry is a numerical tool that can be applied to a greater extent. With this in mind, a 2-20-node element is introduced in Section 3.5. The element matrices were derived through various numerical means; Newton-Cotes with 2, 3 and 4 integration points and Gaussian quadrature with 7, 9 and 11 integration points. The evaluation and implementation of all elements except for the 8-node hexahedral was halted as a numerical instability was found, as discussed in Section 3.6. In conclusion, the element matrices for the 8-node hexahedral were derived through numerical integration and the element matrices for the 4-tetrahedral were derived symbolically. Through numerical integration, the element matrices for reduced complexity elements were found. The implementation of the 8-node hexahedral elements was performed, the remainder elements were not implemented, however these are ready to be implemented in future work.

The requirement of the surface size vs the distance between the top and bottom surface in a plate is constrictive and significantly inhibits the applicability of the solution. The increase in mesh density makes it impossible to evaluate larger, thin structures. Two possibilities are available, the first is to significantly increase the mesh density such that the ratio between the size of the surface elements and the distance between the surfaces that discretize the conductive domain is within a range where Gaussian quadrature does not exhibit the numerical instability. Alternatively, the manner in which the singular integrals are solved can be altered. Alternative solutions to these integrals are presented by Z. Ren [52], S. Balac [60], G. Xie [61], H. Ma [62] and A. Masserey [5]. In the next chapter, the problem of the numerical integration instability, as discussed in Subsection 3.6, will be addressed.

Chapter 4

Solving weakly and strongly singular boundary integral formulations in FEM-BEM thermoplastic composite welding

In this chapter, the weakly and strongly singular integrations that occur when formulating the boundary element problem are discussed. The derivation of the Dirichlet-to-Neumann operator is presented in Section 4.1. The numerical integration methods employed in this dissertation are presented in Section 4.2. The Dirichlet-to-Neumann operator consists of two singular equations, the first is discussed in Section 4.3 while the second is discussed in Section 4.4. The solutions presented in these sections are valid for triangular surfaces, in Section 4.5 these solutions are expanded to allow for application to quadrilateral surfaces.

4.1 Derivation of the Dirichlet-to-Neumann Operator

The FEM-BEM approach requires the following steps:

1. On the boundary of the conductive domain, which is modeled with a finite element mesh, the magnetic field is found by modeling the coil. The coil is discretized and assumed to be a line through the center of its cross-section, then applying the Biot-Savart law to calculate the electromagnetic field with the current and the frequency as inputs;

2. The magnetic scalar potential on the surface of the laminate is found through

the magnetic vector field

3. With Green's theorem, the volume integral over the non-conductive space, is transformed to a surface integral at the interface between the conductive domain and non-conductive domain as shown in Eqn. 4.1.1.

$$\int_{\Omega_o} \mu \vec{\nabla}\Phi \cdot \vec{\nabla}\psi \; d\Omega_o = \int_{\Gamma_O} \mu \frac{\partial \Phi}{\partial n} \cdot \psi \; d\Gamma_O = P\Phi \cdot \psi \tag{4.1.1}$$

Here, Ω_o is the non-conductive domain, Γ_O is the boundary surface, as previously shown in Figure 2.10. P is an integral operator, and ψ is the weighting function of the weighted residual method to the Laplacian equation. By discretization of Eqn. 4.1.1, the P operator can be found in the form of the "outside stiffness matrix" which provides a relationship between the Dirichlet boundary condition Φ and the Neumann boundary condition $\frac{\partial \Phi}{\partial n}$. Ren published on these boundary integral formulations in his previous work [52, 63]. Specifically, in the second publication, a comparison was made between different boundary integral formulations. In conclusion, the single-layer source method seems to be most appropriate to solve this problem in an accurate yet resource efficient way. The single-layer source method imposes a distribution of virtual charges on the boundary of the conductive domain. The scalar potential of the virtual charge is then expressed through the Fredholm integrals as:

$$\Phi\left(\vec{y}\right) = \int_{\Gamma_O} \frac{q\left(\vec{x}\right)}{\left|\vec{y} - \vec{x}\right|} \; d\vec{x} \tag{4.1.2}$$

In Eqn. 4.1.2, $\vec{x}$ and $\vec{y}$ are points on the boundary Γ. The normal derivative to the boundary of the magnetic scalar potential, as required by Eqn. 4.1.1, can be found by:

$$\frac{\partial \Phi\left(\vec{y}\right)}{\partial n} = 2\pi q\left(y_0\right) + \int_{\Gamma} q\left(\vec{x}\right) \frac{\partial}{\partial n} \frac{1}{\left|\vec{y} - \vec{x}\right|} \; d\vec{x} \tag{4.1.3}$$

By multiplying Eqns. 4.1.2 and 4.1.3 with a test functions $\eta(\vec{y})$ and $\psi(\vec{y})$ respectively. After which the integration over the boundary Γ_O can be performed. The following variational formulation relating the virtual charge distribution $q(\vec{y})$ to the magnetic scalar potential is found:

$$\int_{\Gamma_O} \Phi(\vec{y})\,\eta(\vec{y})\,d\vec{y} = \int_{\Gamma_O}\int_{\Gamma_O} \frac{q(\vec{x})}{|\vec{y}-\vec{x}|}\eta(\vec{y})\;\; d\vec{x}\;d\vec{y} \tag{4.1.4}$$

In this equation, the test function $\eta(\vec{y})$ is a constant with respect to the integration over the surface coordinates $\vec{x}$.

$$\begin{aligned}\int_{\Gamma_O} \frac{\partial\Phi(\vec{y})}{\partial n}\cdot\psi(\vec{y})\,d\vec{y} &= \int_{\Gamma_O} 2\pi q(y_0)\cdot\psi(\vec{y})\,d\vec{y} \\ &+ \int_{\Gamma_O}\int_{\Gamma_O} q(\vec{x})\,\frac{n_x\cdot|\vec{y}-\vec{x}|}{|\vec{y}-\vec{x}|^3}\psi(\vec{y})\;\; d\vec{x}\;d\vec{y}\end{aligned} \tag{4.1.5}$$

The test function $\psi(\vec{y})$ is a linear interpolation function that is identical to the linear nodal shape functions. The Eqns. 4.1.4 and 4.1.5 can be expressed as a system of matrix equations:

$$\Phi(\vec{y}) = \boldsymbol{K}q \tag{4.1.6}$$

$$\frac{\partial\Phi(\vec{y})}{\partial x} = \left(\frac{\boldsymbol{B}}{2} + \boldsymbol{H}\right)q \tag{4.1.7}$$

Here, the matrices $\boldsymbol{B}$, $\boldsymbol{K}$ and, $\boldsymbol{H}$ are defined in Eqns. 2.3.62, 2.3.63 and 2.3.64 respectively. Bringing the $\boldsymbol{K}$-matrix in Eqn. 4.1.6 to the left-hand side and substituting this function for q into Eqn. 4.1.7 yields a stiffness matrix that can transform Dirichlet boundary conditions to Neumann boundary conditions, as shown in Eqn. 4.1.8.

$$\frac{\partial \Phi(\vec{y})}{\partial n} = (\boldsymbol{B}/2 + \boldsymbol{H})\, \boldsymbol{K}^{-1}\, \Phi\,(\vec{y}) \tag{4.1.8}$$

Now, the stiffness matrix $\boldsymbol{P^*}$ is defined in Eqn. 4.1.9 [63, 52].

$$\boldsymbol{P^*} = \left(\frac{\boldsymbol{B}}{2} + \boldsymbol{H}\right) \boldsymbol{K^{-1}} \tag{4.1.9}$$

In this formulation, the two integrals, the double integral on the right-hand side of Eqn. 4.1.4 and the double integral in the second term of the right hand-side of Eqn. 4.1.5, both have an integrand that exhibits singularities as the denominator approaches 0. The first will be identified as I_1 and the second as I_2:

$$I_1 = \int_{\Gamma_O} \int_{\Gamma_O} \frac{1}{|\vec{y} - \vec{x}|}\, d\vec{x}\, d\vec{y} \tag{4.1.10}$$

$$I_2 = \int_{\Gamma_O} \int_{\Gamma_O} \frac{n_x \cdot |\vec{y} - \vec{x}|}{|\vec{y} - \vec{x}|^3} N\,(\vec{y})\; d\vec{x}\, d\vec{y} \tag{4.1.11}$$

In Eqn. 4.1.11, the shape function is independent of $\vec{y}$, therefore the shape function can be moved outside the first integral:

$$I_1 = \int_{\Gamma_O} \int_{\Gamma_O} \frac{1}{|\vec{y} - \vec{x}|}\, d\vec{x}\, d\vec{y} \tag{4.1.12}$$

$$I_2 = \int_{\Gamma_O} N\,(\vec{y}) \int_{\Gamma_O} \frac{n_x \cdot |\vec{y} - \vec{x}|}{|\vec{y} - \vec{x}|^3}\, d\vec{x}\, d\vec{y} \tag{4.1.13}$$

Now, the inside integral of these two equations are defined as k_1 and k_2:

$$k_1 = \int_{\Gamma_O} \frac{1}{|\vec{y} - \vec{x}|} d\vec{x} \tag{4.1.14}$$

$$k_2 = \int_{\Gamma_O} \frac{n_x \cdot |\vec{y} - \vec{x}|}{|\vec{y} - \vec{x}|^3} d\vec{x} \tag{4.1.15}$$

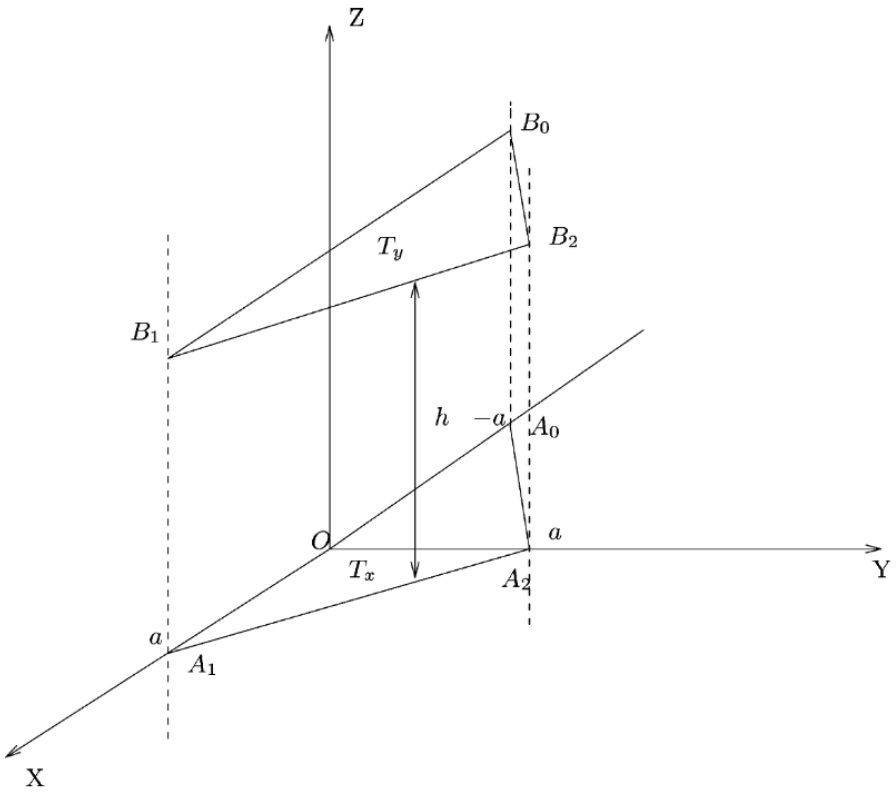

Figure 4.1: Two opposite triangular surfaces [5]

For illustration, please refer to Figure 4.1. Two parallel triangles are presented, triangle T_x and T_y consisting of nodes A_0, A_1 and A_2 and B_0, B_1 and B_2 respectively. The variables $\vec{x}$ and $\vec{y}$ denote points in these triangles. The vertical distance between these triangles is h. The denominator in Eqns. 4.1.14 and 4.1.15 is a function of the distance between the two surfaces shown in the figure. To simplify discussing the equations, the fractions in Eqn. 4.1.10 and 4.1.11 are defined as the first kernel O_1 and second kernel O_2, respectively. The kernels O_1 and O_2 are weakly and strongly singular respective of whether surfaces in the parallel planes overlap and the distance between the two parallel surfaces reduce. As these triangular surfaces move closer together and h becomes smaller, or the $\frac{h}{a}$ ratio becomes smaller, the fraction defines α as shown in Eqn. 4.1.16. The reduction of α is analogous to reducing the distance between the top and bottom surface of a laminate (Section 3.6) without changing the size of the elements. The weak and strong singular behavior of Eqns. 4.1.14 and

4.1.15, respectively, are demonstrated in Figure 4.2. In the figure, the x-axis, r, is the distance between a point on the surface T_x and T_y. For demonstration purposes the points considered are the midpoints of the surfaces and the height, h, between the surfaces is altered to alter the value of r. The singular behavior can clearly be observed, the kernel value, as presented on the y-axis approaches infinite as r approaches 0.

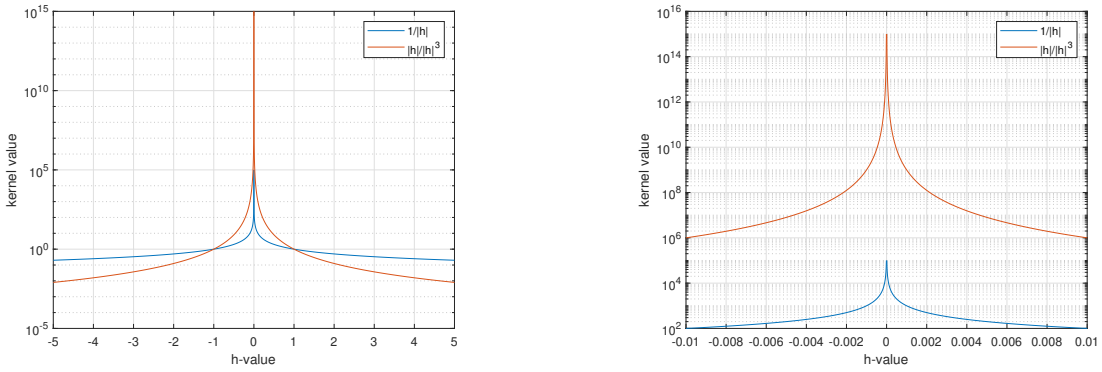

(a) Example of singularity by both kernels

(b) Example of singularity zoomed in on the singularity

Figure 4.2: Example of for both integration kernels

The electromagnetic analysis is performed on a thin volume, to assess what defines a "good" integration, the following case is presented: the two parallel triangular surfaces are in R^3, these surfaces are perpendicular to the xy-plane and are offset by a distance h in the z-direction, as shown in Figure 4.2. This configuration is chosen as it encompasses the worst-case scenario. For other cases the surfaces may not overlap which makes the singularity less severe, or it may disappear entirely. For parallel surfaces, the singularity is the most extreme. In the case that one surface is tilted with respect to the other, the numerator of the second kernel is less severe. The surface or sides of the elements are related to this distance h, through the ratio α:

$$\alpha = \frac{h}{a} \tag{4.1.16}$$

The relevant range of the ratio α is established by assuming that a laminate with a length of 300 mm, width of 300 mm and a thickness of 1 mm is a realistic case. A composite of 1 mm thickness contains 8 plies, which is considered the minimum reasonable, and generally the desire is to simulate thicker laminates which reduce the severity of the singularity. A coarse mesh with 10-elements in the horizontal dimensions is evaluated. An element will then be 30 mm by 30 mm in the horizontal plane while having a thickness of 1 mm. The resulting value of α for this element is $3.333 \cdot 10^{-2}$. Based on this hypothetical worst-case scenario, the lower boundary for the ratio α is set to $1 \cdot 10^{-3}$. The upper bound is not critical, as an increase in α would reduce the severity of the singularity.

To perform numerical calculation of the integrals shown in Eqns. 4.1.12 and 4.1.13, three methods are employed in this thesis. The surface integral is rewritten to be a function of two variables, which is done by converting from global Cartesian coordinates to surface coordinates using Eqn. 4.1.17:

$$\int_T F(\vec{x}) \; d\vec{x} = |T| \int_0^1 \int_0^{1-\eta} F(\xi, \eta) \, d\xi d\eta \tag{4.1.17}$$

Here, $\vec{x}$ is the vector of the original global coordinates, while ξ and η are the surface coordinates of the triangle T with $0 < \xi \leq 1$, $0 < \eta \leq 1$. The area of the triangle is $|T|$. This yields equations that can be numerically integrated through conventional numerical integration schemes which leverage the volume coordinates to reduce the number of variables from 3 to 2 variables, as the volume coordinates can represent a point in space with two variables [4].

4.2 Numerical Integration Methods

Three different numerical integration methods, (I) Gauss-Legendre quadrature; (II) Rathod's quadrature; and (III) Hammer-Marlowe-Stroud quadrature, were investi-

gated to efficiently solve the integrals shown in Eqn 4.1.12 and 4.1.13.

The first numerical integration method is the Gauss-Legendre quadrature formula [59]. By substituting in the boundary of the first integral, a summation is found of the form:

$$\int_0^1 \int_0^{1-\eta} F(\xi,\eta)\ d\xi\ d\eta = \sum_{i=1}^{n}\ w_i\ \sum_{j=1}^{m}\ w_j\ F(\xi_i,\eta_j) \tag{4.2.1}$$

In this equation, the m and n denote the number of integration points, i and j the integration point numbering, and w_i and w_j are weights for the respective integration points. Variables ξ_i and η_j denote the integration point location. This equation does not take into account the altered surface to enable integration of a triangle as opposed to a quadrilateral with standard Gaussian-Legendre quadrature.

By symbolically substituting the boundary of $1-\eta_x$ and $1-\eta_y$, a solution can be found through the Gauss-Legendre quadrature rule. The boundaries of the Gaussian quadrature can be reformulated with Eqn. 4.2.2 [59]:

$$\int_a^b f(x)\ dx = \int_{-1}^{1} f\left(\frac{(b-a)\,t+(b+a)}{2}\right)\frac{b-a}{2}\ dt \tag{4.2.2}$$

After substituting the boundaries of $1-\eta_x$ into Eqn. 4.2.2 to find new quadrature coefficients and weights based on the weights and coefficients of Gauss-Legendre quadrature rules, Eqn. 4.2.3 is found.

$$\int_0^1 \int_0^{1-\eta} F(\xi,\eta)\ d\xi\ d\eta = \sum_{i=1}^{N} w_i \sum_{j=1}^{N} w_j F\left(\frac{(1-\eta_j)\,\xi_i+(1-\eta_j)}{2},\eta_j\right) \tag{4.2.3}$$

The second numerical integration method is an alteration to Gauss' quadrature rule, as introduced by Rathod [64]. This method provides a more accurate solution, and the weights and nodes do not require symbolic substitution. It maps the triangular problem to a standard 2-square $(\xi,\eta)|-1\leq\xi,\eta\leq 1$, by continuing from Eqn.

4.1.17 the following can be found [64]:

$$\int_0^1 \int_0^{1-\eta} F(\xi,\eta)\, d\xi d\eta = \int_{-1}^1 \int_{-1}^1 F\left(\frac{1+\xi}{2}, \frac{(1-\eta)(1+\eta)}{4}\right) \left(\frac{1-\xi}{8}\right) d\xi d\eta \tag{4.2.4}$$

Then, substituting Eqn.4.2.4 in the Gaussian quadrature equation yields [64]:

$$\begin{aligned} \iint_T F(x,y)\, dxdy &= |T| \int_{-1}^1 \int_{-1}^1 F\left(\frac{1+\xi}{2}, \frac{(1-\eta)(1+\eta)}{4}\right) \left(\frac{1-\xi}{8}\right) d\xi d\eta \\ &= |T| \sum_{i=1}^n \sum_{j=1}^n w_i w_j \frac{1-\xi_i}{8} F\left(\frac{1+\xi_i}{2}, \frac{(1-\xi_i)(1+\eta_j)}{4}\right) \end{aligned} \tag{4.2.5}$$

The third and final method of numerical integration being considered is the Hammer-Marlowe-Stroud (HMS) conical integration quadrature [65, 66].

In Figure 4.3 the value in the integral in Eqn. 4.1.11 is shown, when numerical integration is performed through Gaussian Quadrature with 3 and 9 nodes. The other pair of lines employ the HMS quadrature to evaluate the inner surface integral, in Eqn. 4.1.15, and Rathod's quadrature to evaluate the outer integral. Note: the x-axis in Figure 4.3 represents the ratio of h/a, and ranges from 0.001 to 0.5. This interval is chosen as the lower bound is in line with the previously established lower bound, in this section. The upper bound is irrelevant, as the singularity only manifests as the h/a ratio approaches 0 and is stable for larger ratios. The y-axis is limited to 1 to ensure the graph remains readable even when the integration values goes to infinity as the ratio of h/a approaches zero.

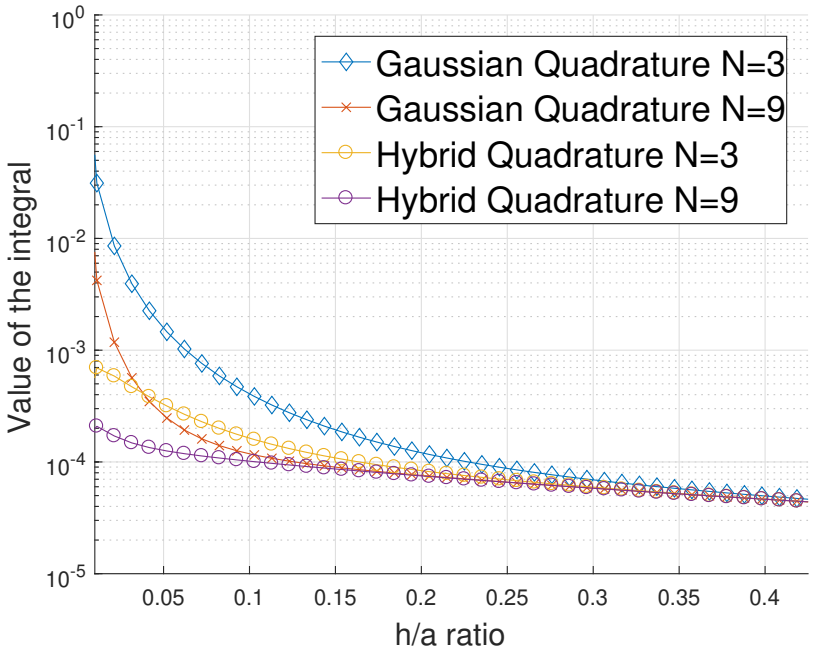

Figure 4.3: Comparing conventional numerical integration to hybrid numerical integration.

Applying a hybrid method, a combination of Rathod's quadrature and HMS' quadrature proved to provide a stable solution even when the ratio of h/a approaches zero (as can be seen in Figure 4.3, and note the integral value does not go to infinity). The hybrid approach used Rathod's quadrature to solve the inner surface integral of Eqn. 4.1.13 and HMS' quadrature to solve the outer surface integral of Eqn. 4.1.13. The singularity is caused by the integration nodes laying on top of one another in the surfaces over which the numerical integration takes place. When increasing the number of integration points in the hybrid method to 9, a more stable solution to the integral was obtained, however, for h/a ratios between 0.2 and 0.001 the integral value increases first before decreasing. This hump, the initial increase and subsequent decrease, is attributed to the discretization of the continuous integral, and the effect of the numerical instability is reduced, however, it persists in the form of the hump. This phenomenon is reduced when 9-node integration schemes are applied. An increase in the number of integration points can be used to provide an accurate solution,

however, a larger number of nodes would still be required, and the resources required to pursue this solution would be too computationally expensive. Therefore, additional research is required into a partially analytical approach [5, 63] as, in the analytical case, one of the surfaces is evaluated in a continuous manner. By evaluating on surface analytically, this type of singularity is reduced, or may be eliminated entirely. Additionally, the solution will likely be less resource intensive. In the next section, a semi-analytical solution to Eqn. 4.1.10 will be presented.

4.3 Integral of the First Kernel

In this section, the weakly singular integration, as presented in Eqn. 4.1.12, is evaluated. The singularity is solved through a partial semi-analytical solution, as presented by Masserey et al. [5]. The inner surface integral, presented in Eqn. 4.1.14 analytically, was solved analytically.

In reference to Figure 4.1, the integration from a point in the triangle T_y, defined to be M_y, over the triangle T_x is performed. In Masserey's paper [5], a solution is found for 3 different cases: the first is when the point M_y does not belong to the plane of triangle T_x. The second case is when M_y belongs to the plane of triangle T_x, and finally, the third case is when the triangles T_x and T_y overlap. The cases mentioned here are discussed at length by Masserey but are not repeated in this dissertation, as it is well explained in the original work. In this dissertation, only the second case is discussed and implemented as this encompasses both the first and second case, the third case where the triangles overlap will not have to be accounted for, as in that case, only the $\boldsymbol{B}$ matrix is evaluated. Some additional variables are defined in the context of Figure 4.1:

$$\beta = \overrightarrow{M_y A_0} \cdot \overrightarrow{n}_x \tag{4.3.1}$$

$$d = \overline{A_0 A_1}^2 \tag{4.3.2}$$

$$e = 2\overrightarrow{A_0 A_1} \cdot \overrightarrow{M_y A_0} \tag{4.3.3}$$

$$g = 2\overrightarrow{A_0 A_2} \cdot \overrightarrow{A_0 A_1} \tag{4.3.4}$$

$$h = \overline{M_y A_0}^2 \tag{4.3.5}$$

$$j = 2\overrightarrow{A_0 A_2} \cdot \overrightarrow{M_y A_0} \tag{4.3.6}$$

$$k = \overline{A_0 A_2}^2 \tag{4.3.7}$$

The first integration of the surface integral in Eqn. 4.1.14 can be solved analytically:

$$\int_0^{1-\eta_x} f(\xi_x, \eta_x, \xi_y, \eta_y) d\xi = \frac{\ln\left((g-2d)\eta_x + e + 2d + 2\sqrt{\kappa(\eta_x)}\sqrt{d}\right) - \ln\left(g\eta_x + e + 2\sqrt{h + j\eta_x + k\eta_x^2}\sqrt{d}\right)}{\sqrt{d}} \tag{4.3.8}$$

In this equation, κ is as defined:

$$\kappa(\eta_x) = (h + d + e) + (j + g - e_2 d)\eta_x + (d + k - g)\eta_x^2 \tag{4.3.9}$$

The second integration over η_x is performed by integrating over two continuous functions of the form:

$$w(\eta_x) = \ln\left(A\eta_x + B + K\sqrt{C\eta_x^2 + D\eta_1 + E}\right) \tag{4.3.10}$$

Defining $\Delta = D^2 - 4CE$ and then applying two changes of variables:

1. : $t = \eta_x + \frac{D}{2C}$

2. : $t = \sqrt{-\frac{\Delta}{4C^2}}\sinh(u)$

The following equation is found:

$$\begin{aligned}\int_0^1 w(\eta_x)d\xi_x =& \sqrt{-\frac{\Delta}{4C^2}} \int_{\operatorname{arcsinh}\left(\left(\frac{D}{2C}\right)\sqrt{-\frac{4C^2}{\Delta}}\right)}^{\operatorname{arcsinh}\left(\left(1+\frac{D}{2C}\right)\sqrt{-\frac{4C^2}{\Delta}}\right)} \\ & \ln\left(A\sqrt{-\frac{\Delta}{4C^2}}\sinh(u) - \frac{AD}{2C} + B + K\sqrt{-\frac{\Delta}{4C^2}}\cosh(u)\right)\cosh(u)du\end{aligned} \tag{4.3.11}$$

The integral in Eqn. 4.3.11 is of the form $ln\left(Ucosh(u) + Vsinh(u) + Z\right)cosh(u)$. The primitive of a function of this form can be found analytically:

$$\begin{aligned}\int \tilde{w}(u)du =& \frac{\left(VZ - U\sqrt{Z^2+V^2-U^2}\right)ln\left(e^u + \frac{\sqrt{Z^2+V^2-U^2}+Z}{V+U}\right)}{V^2-U^2} \\ & + \frac{\left(VZ + U\sqrt{Z^2+V^2-U^2}\right)ln\left(e^u - \frac{\sqrt{Z^2+V^2-U^2}+Z}{V+U}\right)}{V^2-U^2} - \frac{Zu}{V-U} \\ & + \sinh(u)\left(\ln\left(U\cosh(u) + V\sinh(u) + Z\right) - 1\right)\end{aligned} \tag{4.3.12}$$

This concludes the analytical solution to the first surface integral as found by Masserey. As previously mentioned, these derivations are well elaborated on in the original manuscript[5] and only briefly summarized here. An important assumption here is made that the expression of Eqn. 4.3.8 is always well-defined.

After applying the analytical solution to the first integral, as shown in Eqn. 4.1.12, what remains is the integration over the outer surface integral. The outer surface integral is performed through three different numerical methods, as presented in Section 4.2: (I) the Gaussian quadrature [59] algorithm; (II) Rathod's quadrature [64]; and

(III) the HMS quadrature [65]. To evaluate the accuracy and speed of the algorithms, two triangles, as shown in Figure 4.1, are considered with $a = 0.05$ and h as a variable. The value of I_1 is then shown as a function of the ratio of h/a. When the triangular surfaces, as shown in Figure 4.1, overlap. The distance h is zero, and the exact solution for I_1 is $3.5611 \cdot 10^{-7}$ [5].

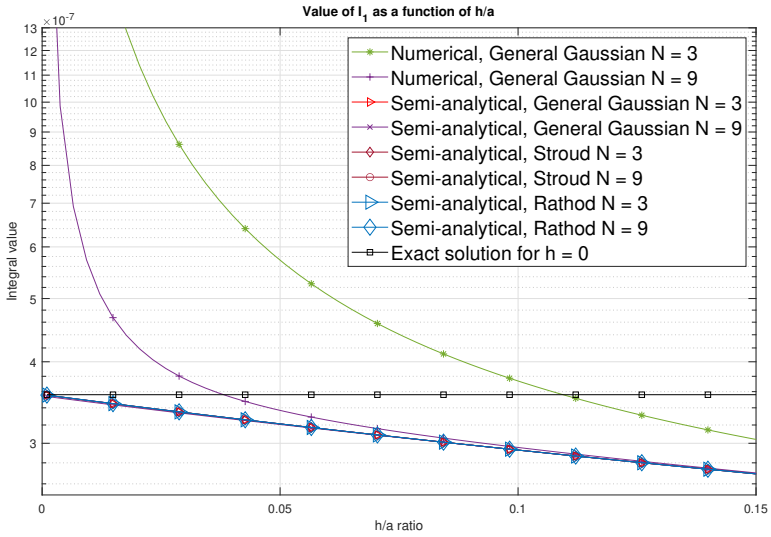

Figure 4.4: Value of the integral as a function of the height ratio $\frac{h}{a}$.

From the graphs in Figure 4.4, a few conclusions can be made. The obvious is that a fully numerical solution does not converge and goes to infinity as the h/a ratio becomes smaller, as predicted in the previous section. The semi-analytical solution proposed by Masserey removes the singularity. The semi-analytical algorithms provide very similar results, regardless of the numerical integration scheme used for the outer integrals. To illustrate this, an expanded plot is presented in Figure 4.5 where the purely numerical integration schemes have been excluded.

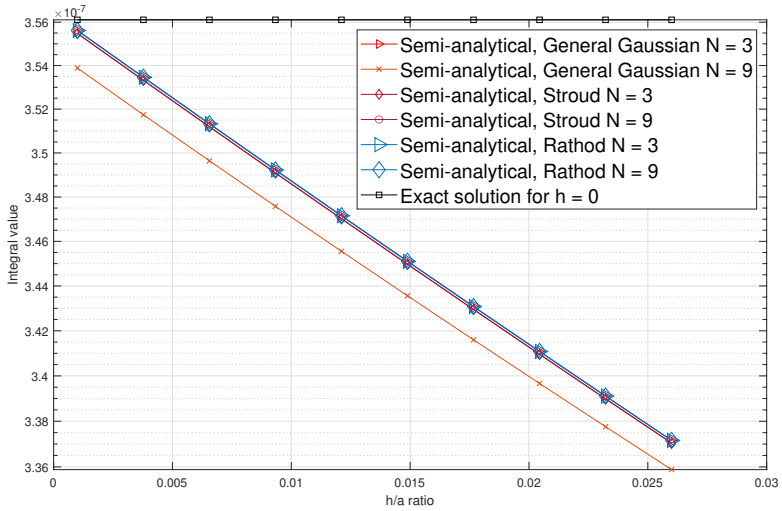

Figure 4.5: Value of the integral as a function of the height ratio $\frac{h}{a}$ with the semi-analytical solutions.

Based on the results in Figure 4.4 and Figure 4.5, the semi-analytical solutions are within 1% of one another. To make an informed decision on which numerical integration scheme is most appropriate for the problem, the problem is evaluated at $h = \frac{a}{10.000.000}$. The error as a percentage of the exact solution and the computational time are shown in Table 4.1 for the three different numerical methods with a single integration point.

Table 4.1: The error and computational time of different numerical integration schemes with 1 integration point

n=1	SA-Gauss	SA-Rathod	SA-HMS
Time [s]	0.003616	0.003846	0.003601
Percentage time	100 %	106 %	99.6 %
Percentage error	17.6 %	13.6 %	19.5 %

For two integration points, the results are shown in Table 4.2, and the result of the evaluation for three integration points is presented in Table 4.3. In these tables, the term "semi-analytical" was abbreviated to SA.

Based on the results presented in Tables 4.1, 4.2, the integration schemes with one

Table 4.2: The error and computational time of different numerical integration schemes with 2 integration points

n=2	SA-Gauss	SA-Rathod	SA-HMS
Time [s]	0.06639	0.06628	0.0588
Percentage time	100 %	99.8 %	88.7 %
Percentage error	1.55 %	2.22 %	1.12 %

Table 4.3: The error and computational time of different numerical integration schemes with 3 integration points

n=3	SA-Gauss	SA-Rathod	SA-HMS
Time [s]	0.223	0.218	0.207
Percentage time	100 %	97.9 %	88.7 %
Percentage error	0.038 %	0.136 %	0.0046 %

and two integration points do not provide sufficient accuracy as they are more than 1% off the expected analytical value. In Table 4.3, the results for the evaluation with the three-node integration scheme is presented. The semi-analytical HMS method appears to not only be the most accurate, but also the most efficient with this number of integration points.

4.4 Integral of the Second Kernel

The integral with the second kernel was presented in Eqn. 4.1.13. To evaluate the integral with the discontinuity, the inner surface integral can be solved analytically. This surface integral was defined as k_2.

$$k_2 = \int_{\Gamma_O} \frac{n_x \cdot |\vec{y} - \vec{x}|}{|\vec{y} - \vec{x}|^3} d\vec{x} \tag{4.4.1}$$

The surface integral, as presented in Eqn. 4.4.1, is solved analytically by Masserey [5] by finding the primitive of the kernel and has a total of two subcases and two parts, for a total of 4 different solutions. Cases 1 through 4 are defined in the next subsections, and evaluated for speed and convergence.

The solution to an integral of the form described in Eqn. 4.4.1, has a solution of the form:

$$\int_0^1 \int_0^{1-\eta_x} \frac{\beta}{\left(d\xi_x^2 + e\xi_x + g\xi_x\eta_x + h + j\eta_x + k\eta_x^2\right)^{\frac{3}{2}}} d\xi_x d\eta_x \tag{4.4.2}$$

In this equation, the variables are as described in Eqns. 4.3.1 through to 4.3.7. First, consider the inner integral

$$\int_0^{1-\eta_x} \frac{\beta}{\left(d\xi_x^2 + e\xi_x + g\xi_x\eta_x + h + j\eta_1 + k\eta_x^2\right)^{\frac{3}{2}}} d\xi_x = Q_1 + Q_2 \tag{4.4.3}$$

The integral is split into two parts Q_1 and Q_2:

$$Q_1 = \frac{2\left(\beta\left(2d - g\right)\eta_x - \beta\left(2d + e\right)\right)}{z\left(\eta_x\right)\sqrt{\left(d + k - g\right)\eta_x^2 + \left(g + j - e - 2d\right)\eta_x + h + e + d}} \tag{4.4.4}$$

$$Q_2 = \frac{\beta g\eta_x + \beta e}{z\left(\eta_x\right)\sqrt{k\eta_x^2 + j\eta_x + h}} \tag{4.4.5}$$

In Eqns 4.4.4 and 4.4.5, the term $z\left(\eta_1\right)$ is:

$$z\left(\eta_x\right) = \left(g^2 - 4dk\right)\eta_x^2 + \left(-4dj + 2eg\right)\eta_x + e^2 - 4dh \tag{4.4.6}$$

The second integration of Eqn 4.4.2 can be performed, the function in this case is of the form:

$$w\left(\eta_x\right) = \frac{b\eta_x + c}{\left(n\eta_x^2 + l\eta_x + m\right)\sqrt{r\eta_x^2 + s\eta_x + t}} \tag{4.4.7}$$

In Eqn. 4.4.4 and 4.4.5, there are occurrences for which the denominator will be 0[5]. The solution to Eqn. 4.4.7 depends on $\left(n\eta_x^2 + l\eta_x + m\right)$ and $\sqrt{r\eta_x^2 + s\eta_x + t}$. To do so, the roots of $\left(n\eta_x^2 + l\eta_x + m\right)$ are defined as:

$$\zeta = \frac{-l - \sqrt{l^2 - 4nm}}{2n} \tag{4.4.8}$$

$$\rho = \frac{-l + \sqrt{l^2 - 4nm}}{2n} \tag{4.4.9}$$

Additionally, ϕ and ψ are defined as:

$$\phi = \sqrt{2\left(r\rho^2 + s\rho + t\right)} \tag{4.4.10}$$

$$\psi = \sqrt{2\left(r\zeta^2 + s\zeta + t\right)} \tag{4.4.11}$$

A total of 2 subcases occur when solving Eqn. 4.4.7, which needs to be solved twice for Eqns. 4.4.4 and 4.4.5:

1. $l^2 - 4nm = 0$, $\phi \neq 0$ and $\psi \neq 0$
2. $l^2 - 4nm = 0$, $\phi = 0$ and $\psi = 0$

When $l^2 - 4nm = 0$, $\phi \neq 0$ and $\psi \neq 0$:

$$\int w\left(\eta_x\right) d\eta_x = \sqrt{2}\frac{\ln\left(\frac{\psi^2 + (s+2r\zeta)(\eta_x - \zeta) + \sqrt{2}\psi\sqrt{r\eta_x^2 + s\eta_x + t}}{\eta_x - \zeta}\right)(b\zeta + c)}{n\left(\rho - \zeta\right)\psi} - \sqrt{2}\frac{\ln\left(\frac{\rho^2 + (s+2r\rho)(\eta_x - \rho) + \sqrt{2}\rho\sqrt{r\eta_x^2 + s\eta_x + t}}{\eta_x - \rho}\right)(b\rho + c)}{n\left(\rho - \zeta\right)\phi} \tag{4.4.12}$$

For $l^2 - 4nm = 0$, $\phi = 0$ and $\psi = 0$:

$$\int w\left(\eta_x\right) d\eta_x = \frac{2}{n\sqrt{r}} \frac{-\left(bS + 2c\right)\eta_x + cS + 2bP}{\left(S^2 - 4P\right)\sqrt{\eta_x^2 - S\eta_x + P}} \tag{4.4.13}$$

As this needs to be considered for both Q_1 and Q_2, a total of 4 cases are defined to solve the integral k_2, as presented in Eqn. 4.1.15.

1. Neither denominator is 0: both Q_1 and Q_2 can be solved for with Eqn. 4.4.12.
2. The denominator in both Eqn. 4.4.4 and 4.4.5 is 0, and need to be solved using Eqn. 4.4.13
3. The denominator in Eqn. 4.4.4 is not 0 but the denominator in Eqn. 4.4.5 is. Therefore, Eqn. 4.4.4 is solved with Eqn. 4.4.12 and Eqn. 4.4.5 is solved with Eqn. 4.4.13
4. The denominator in Eqn. 4.4.4 is 0 but the denominator in Eqn. 4.4.5 is not. Therefore, Eqn. 4.4.4 is solved with Eqn. 4.4.13 and Eqn. 4.4.5 is solved with Eqn. 4.4.12

These cases are individually implemented, and the implementation is evaluated for speed and accuracy in the subsections 4.4.1 through 4.4.4.

4.4.1 Integral of I_2 case 1

Case 1 was defined as the case for which Eqn. 4.4.4 and 4.4.5 have no zero denominators. The solution in this case is presented in Masserey [5]. In Figure 4.6, a plot presented for case 1, is evaluated using the same surfaces presented in Figure 4.1. This is similar to the plots for I_1, the x-axis contains the ratio of h/a and the value of the integral is on the y-axis. The inner surface integral is solved with the analytical solution as presented by Masserey [5] and the outer surface integral is approximated with numerical integration. The numerical integration methods applied are the three methods as presented before: the Gaussian, HMS and Rathod integration schemes.

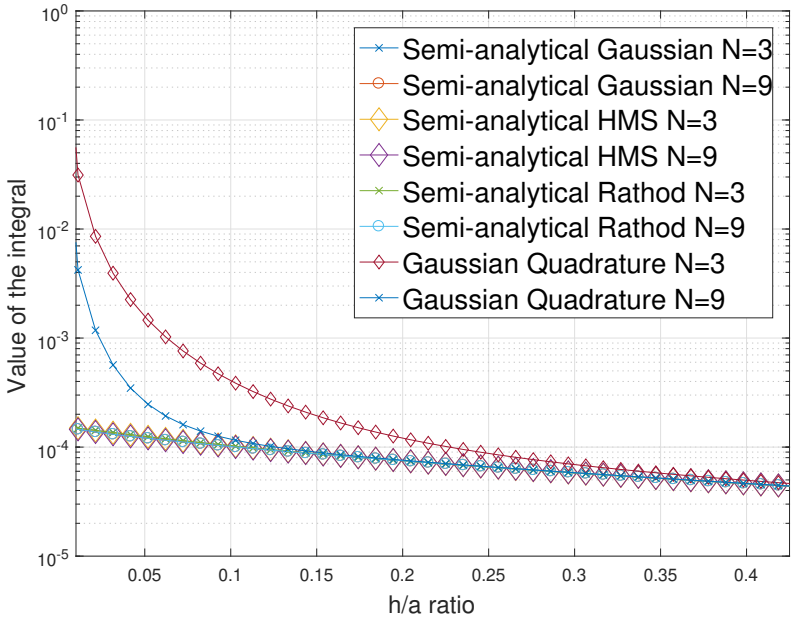

Figure 4.6: Value of the second integral as a function of the height ratio $\frac{h}{a}$.

From the plot shown in Figure 4.6, the conclusion can be drawn that the purely numerical methods go to infinity as the ratio of h/a goes to 0. The numerical methods prove to be divergent, as in the previous kernel. All semi-analytical methods provide a converging solution, and approximate the value of the integral. The difference between a 3-node and 9-node integration scheme is not visible from the figure.

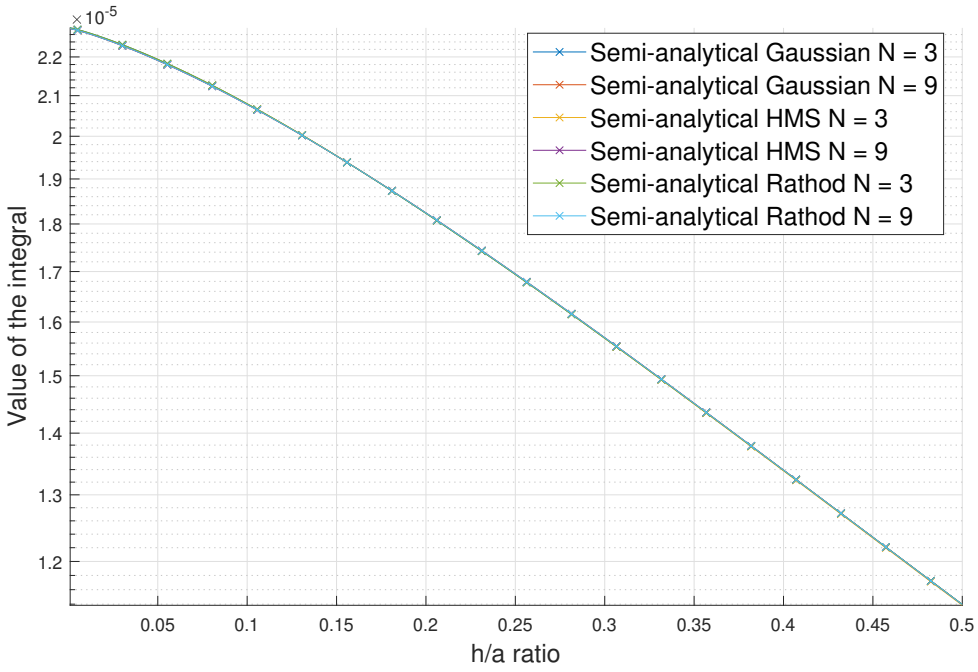

Figure 4.7: Comparison of the semi-analytical solutions for the second kernel.

In Figure 4.7, the purely numerical solutions are omitted and only the semi-analytical results are presented. The semi-analytical methods are evaluated with the three different numerical integration schemes for the second surface integral. The 3-node and 9-node integration schemes are presented. The difference between the value of the integral for the three and nine node numerical integration is generally less than 1% therefore, the computational efficiency of the integration is chosen to be the deciding factor in the selection of which algorithm to implement.

To trade off accuracy and speed, the semi-analytical solution is numerically integrated with the 3 methods. The numerical integration is done with 1 through 5 nodes, which yields 15 functions. The functions are first evaluated at an h/a ratio of 100. At these high ratios, the purely numerical solution should be identical to the semi-analytical solution if the semi-analytical solution is correctly implemented. The results are presented in Table 4.4 and Table 4.5.

When the second kernel is evaluated with a 5-node numerical integration scheme,

Table 4.4: Value of integration for I_2 case 1 for numerical integration

n	1	2	3	6	9
Numerical Rathod	6.250E-10	8.333E-10	8.333E-10	8.333E-10	8.333E-10
Numerical HMS	8.333E-10	8.333E-10	8.333E-10	8.333E-10	8.333E-10

Table 4.5: Value of integration for I_2 case 1 for semi-analytical integration

n	1	2	3	4	5
SA-Rathod	6.250E-10	8.333E-10	8.333E-10	8.333E-10	8.333E-10
SA-Gauss	6.250E-10	8.333E-10	8.333E-10	8.333E-10	8.333E-10
SA-HMS	8.333E-10	8.333E-10	8.333E-10	8.333E-10	8.333E-10

using the semi-analytical solution, as shown in Table 4.5, the results agree with the evaluation of the purely numerical solution, as shown in Table 4.4, confirming that the results of the symbolic integration of the function is correct. The speed of the semi-analytical methods is shown in Table 4.6.

Table 4.6: Time required in seconds for one iteration of case 1 for different number of nodes

n	1	2	3	4	5
SA-Rathod	1.45E-05	1.55E-04	8.24E-04	2.10E-03	4.70E-03
SA-Gauss	1.44E-05	1.47E-04	6.66E-04	2.10E-03	4.20E-03
SA-HMS	1.37E-05	1.39E-04	5.58E-04	1.70E-03	4.10E-03

In Table 4.6 the time required to run one iteration of the integration function is shown in seconds. The three different semi-analytical functions are evaluated for one through five nodes. Based on this table, the HMS semi-analytical method is consistently the fastest by 5 to 10 percent. Next is to assess the accuracy of the function at the lower bound h/a ratio of 1×10^{-3}, as discussed in Section 4.1. When employing a 15 point numerical integration scheme, the semi-analytical solution yields a value of 2.45713×10^{-5}. In Table 4.7, the result of evaluating the function and the error with respect to the integration with 15 integration points is presented. In this table, the numbers are truncated for the sake of brevity, however the displayed

percentage error is calculated with the non-truncated values.

Table 4.7: Value and error of the integration for case 1 for different integration schemes and nodes

n	1	2	3	4	5
SA-Rathod	1.89E-05	2.49E-05	2.47E-05	2.46E-05	2.46E-05
Error w.r.t. n=15 as %	22.941	1.439	0.503	0.220	0.128
SA-Gauss	1.76E-05	2.48E-05	2.47E-05	2.46E-05	2.46E-05
Error w.r.t. n=15 as %	40.000	1.071	0.369	0.188	0.118
SA-HMS	2.48E-05	2.48E-05	2.47E-05	2.46E-05	2.46E-05
Error w.r.t. n=15 as %	1.037	0.914	0.357	0.182	0.116

With the results of Table 4.7 in mind, the choice is made to implement the semi-analytical HMS with a 2-node numerical integration. The function performs the fastest out of the functions with 2 integration nodes, and the error with respect to a 15-node numerical scheme is less than 1%.

4.4.2 Integral of I_2 case 2

In the second case, the general solution contains a division by zero. As discussed in Section 4.4. The same analysis that was performed for case 1 is performed for case 2. Comparison to the numerical computation is impossible, instead convergence of the numerical scheme is verified by running a semi-analytical case for a 15-node numerical integration scheme over the analytical solution. In Table 4.8, the accuracy of the integration is quantified by comparing the 15-node solution of the semi-analytical solution to the result of the lower fidelity semi-analytical solution.

In Table 4.9, the time required in seconds to run one iteration of the function is presented.

For the second kernel, a two node HMS solution provides the fastest solution at an accuracy of less than 1% with respect to the solution that is considered converged, which is when the semi-analytical solution is numerically integrated with the HMS conical integration methodology with just a single node. The other two numerical

Table 4.8: Value and error of the integration for case 2 for different integration schemes and nodes

n	1	2	3	4	5
SA-Rathod	-8.83E-03	-1.18E-02	-1.18E-02	-1.18E-02	-1.18E-02
Error w.r.t. n=15 %	-25.170	-0.227	-0.227	-0.227	-0.227
SA-Gauss	-8.83E-03	-1.18E-02	-1.18E-02	-1.18E-02	-1.18E-02
Error w.r.t. n=15 %	-25.170	-0.227	-0.227	-0.227	-0.227
SA-HMS	-1.18E-02	-1.18E-02	-1.18E-02	-1.18E-02	-1.18E-02
Error w.r.t. n=15 %	-0.227	-0.227	-0.227	-0.227	-0.227

Table 4.9: Time required in seconds for one iteration of case 2 for different number of nodes

n	1	2	3	4	5
SA-Rathod	8.16E-06	2.79E-04	1.97E-04	4.87E-04	1.30E-03
SA-Gauss	2.02E-05	1.01E-04	2.51E-04	1.20E-03	1.60E-03
SA-HMS	8.12E-06	4.52E-05	4.34E-04	7.90E-04	1.70E-03

integration methods are off significantly at a single node integration. To ensure robustness, the higher fidelity 2-node integration is chosen.

4.4.3 Integral of I_2 case 3

The third case occurs when the denominator in Eqn. 4.4.4 is 0 while Eqn. 4.4.5 can be solved without a 0 in the denominator. In Table 4.10, the results of the integration methods and the error are shown. In all three cases, the 2-node integration schemes are sufficiently accurate.

Table 4.10: Value and error of the integration for case 3 for different integration schemes and nodes

n	1	2	3	4	5
Semi Rathod	-5.53E-03	-4.43E-03	-4.43E-03	-4.43E-03	-4.43E-03
Error w.r.t. n=5 %	24.921	-0.001	0.000	0.000	0.000
Semi Gauss	-4.42E-03	-4.43E-03	-4.43E-03	-4.43E-03	-4.43E-03
Error w.r.t. n=5 %	-0.053	0.001	0.000	0.000	0.000
Semi HMS	-5.90E-03	-4.43E-03	-4.43E-03	-4.43E-03	-4.43E-03
Error w.r.t. n=5 %	33.279	0.000	0.000	0.000	0.000

In Table 4.11, the time required in seconds to run one iteration of the function is displayed.

Table 4.11: Time required in seconds for one iteration of case 3 for different number of nodes

n	1	2	3	4	5
Semi Rathod	5.63E-05	2.90E-04	3.25E-04	6.09E-04	2.00E-03
Semi Gauss	2.15E-05	8.78E-05	2.14E-04	1.30E-03	2.80E-03
Semi HMS	1.84E-05	7.88E-05	4.88E-04	1.10E-03	2.50E-03

Based on these results, the HMS 2-node numerical integration is considered sufficiently converged, and the fastest of the 3 numerical integration methodologies.

4.4.4 Integral of I_2 case 4

The fourth and final case occurs when the denominator in Eqn. 4.4.4 is not 0, however, the denominator of Eqn. 4.4.5 is 0. The results of the functions and the error with respect to the 15-node integration scheme are presented in Table 4.12.

Table 4.12: Value and error of the integration for case 4 for different integration schemes and nodes

n	1	2	3	4	5
Semi Rathod	-3.32E-03	-7.37E-03	-7.37E-03	-7.37E-03	-7.37E-03
Error w.r.t. n=15 %	-24.996	0.005	0.002	0.001	0.000
Semi Gauss	-4.42E-03	-7.37E-03	-7.37E-03	-7.37E-03	-7.37E-03
Error w.r.t. n=15 %	-39.991	0.003	0.001	0.001	0.000
Semi HMS	-5.90E-03	-7.37E-03	-7.37E-03	-7.37E-03	-7.37E-03
Error w.r.t. n=15 %	-19.978	0.003	0.001	0.000	0.000

In Table 4.13, the time required in seconds to run one iteration of the function is displayed.

Based on these results, the HMS 2-node numerical integration is considered sufficiently converged and the fastest of the 3 numerical integration methodologies. The algorithms, as described above, are for triangular elements. For these to be suit-

Table 4.13: Time required in seconds for one iteration of case 4 for different number of nodes

n	1	2	3	4	5
Semi Rathod	9.56E-06	2.66E-04	2.78E-04	5.90E-04	2.90E-03
Semi Gauss	1.76E-05	8.88E-05	2.03E-04	1.30E-03	1.30E-03
Semi HMS	1.37E-05	8.99E-05	4.71E-04	9.30E-04	2.40E-03

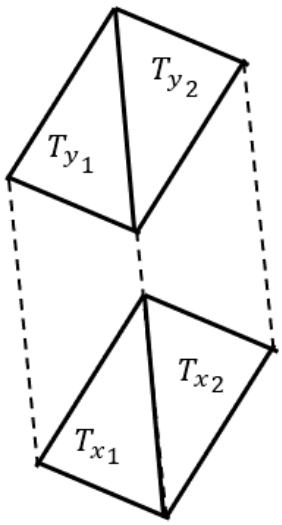

Figure 4.8: Transforming triangular solution to quadrilateral solution

able with the already existing code, which uses quadrilateral/hexahedral elements to discretize the problem volume, some additional steps are required.

4.5 Expanding the Solution to Quadrilateral Elements

In the current iteration of the code only square and quadrilateral surfaces are available, as such a solution for quadrilateral elements is required. The difference in the value of the integral for the triangular solution can be found by splitting the quadrilateral problem into four triangular problems, as shown in Figure 4.8.

This yields the following 4 integrals, that are functions of the triangles T_{x1}, T_{x2}, T_{y1} and T_{y2}. Summing the integrals yields the equivalent integral of both quadrilateral

surfaces.

$$\iint_{Q_x}\iint_{Q_y} f = \iint_{T_{x1}}\iint_{T_{y1}} f + \iint_{T_{x1}}\iint_{T_{y2}} f + \iint_{T_{x2}}\iint_{T_{y1}} f + \iint_{T_{x2}}\iint_{T_{y2}} f \qquad (4.5.1)$$

In this manner, the triangular integrals, as defined in Eqns. 4.1.12 and 4.1.13, can be summed to find the integral over a set of quadrilateral surface elements.

Chapter 5

Numerical validation

In Chapter 3, an 8-node hexahedral element was introduced and the element matrices $\boldsymbol{M}^a$, $\boldsymbol{N}^a$, $\boldsymbol{B}^a$, $\boldsymbol{K}^a$ and $\boldsymbol{H}^a$ were derived. Some initial verification on the individual matrix calculation was performed. In Section 5.1, the 8-node element is validated by comparing it to its baseline brick element, which was integrated symbolically. In Chapter 4, the Dirichlet-to-Neumann operator was presented and a semi-analytical solution was found, implemented and the individual calculations were verified. In addition to the verification already performed, in this chapter, the results of the work done in the previous chapters is demonstrated by simulating a welding case and comparing it to the results from a commercially available code package.

5.1 Verification of 8-node Implementation

In this section, the implementation of the methodologies is verified using a 254 mm (10 inch) by 254 mm (10 inch), 4 ply composite laminate with a total thickness of 0.5 mm. The stacking sequence was chosen to be [90/0/0/90], and the coil was positioned at the center of the laminate plate at a distance of 11 mm above the top surface (see Figure 5.1). The conductivity matrix for the ply in its principal directions is shown in Eqn. 5.1.1, and the magnetic permeability of the air is $1.2566 \cdot 10^{-6} H/m$ and the relative magnetic permeability is $\mu_r = 1$. The coil is representative of a commercially available coil and was sourced from KvE Composites Group, the electric current has a magnitude of 610 Ampere and a frequency of 295 kHz. The x-direction is aligned with the 0^o degree direction of the laminate. The conductivity of a ply is presented

in Eqn. 5.1.1.

$$\sigma = \begin{bmatrix} 9827.72 & 0 & 0 \\ 0 & 1.3 & 0 \\ 0 & 0 & 0.0816 \end{bmatrix} \tag{5.1.1}$$

To verify the discretization of the model, a convergence study is performed. The laminate volume is discretized in the thickness, with one element for each ply. In the length and width direction, the same number of elements are used. The dimensions of the width and length of one element is varied from 25.4 mm (1 inch) to 6.35 mm (0.25 inch). The model is discretized with the 6.35 mm (0.25 inch) elements, as shown in Figure 5.1.

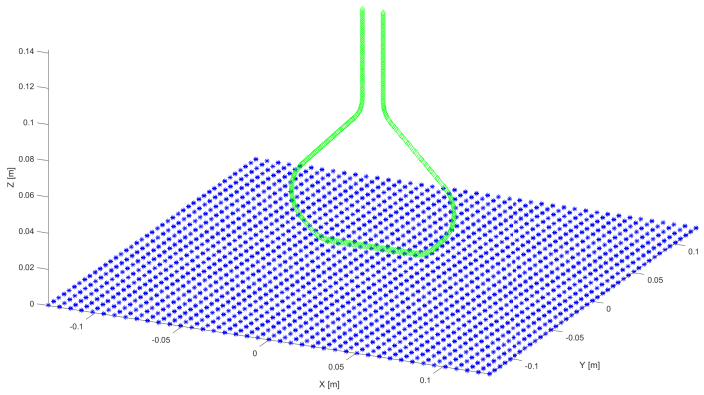

Figure 5.1: Validation model with a 6.35 mm (0.25 inch) element size.

The total volumetric heat generation (in Joules per second) for the convergence study is shown in Table 5.1. As expected, the volumetric heat generated converges when the number of elements is increased, as is shown in Table 5.1 and is visually represented in Figure 5.2. Note, convergence was obtained at 0.375 inch mesh element, since the difference between 0.375 and 0.25 mesh element is about 1%.

Table 5.1: Convergence of the brick and hexahedral element models for the total heat generated $[J/s]$

Element size	brick element	hexahedral element
1 inch	73.37	73.37
0.75 inch	28.58	28.58
0.5 inch	8.33	8.33
0.375 inch	6.26	6.26
0.25 inch	6.34	6.34

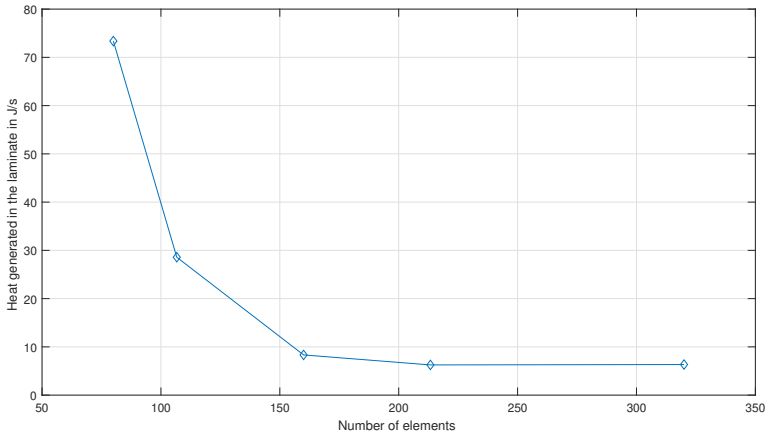

Figure 5.2: Convergence study for the plate for both elements

In Table 5.1 the difference between the models with the different elements is shown, the untruncated values show that the error is in the order of machine precision. To add an extra case, the coil is rotated from the x-direction to the y-direction. The expectation is that the heat generated is lower when the coil is in the x-direction, as the 90 plies are on the outside. The maximum temperature is expected to be higher as the heated 0 layers in this configuration are located next to one another.

The difference in the heat generated with the coil in the y-direction and x-direction is small, as expected. The coil in the x-direction generates a heat of 6.34 J/s while the coil in the y-direction generated is 6.59 J/s. The body losses from the solution of the electromagnetic problem are imported into ABAQUS and a thermal analysis is performed, where the simulation is set up such that it represents enabling the coil

current over the center of the laminate for 10 seconds. The results of this simulation for the mesh containing 0.25 inch elements in the width and length are presented in Figure 5.3.

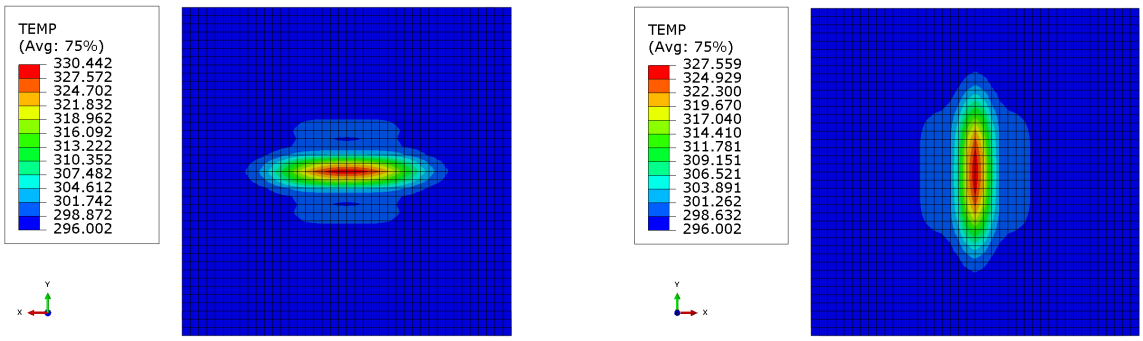

(a) Temperature distribution of the top ply for coil aligned with the x-direction

(b) Temperature of the top ply for coil aligned with the y-direction

Figure 5.3: Temperature distribution plot of the top ply for the x-aligned and y-aligned coil

The maximum temperature in the x-direction aligned coil, as presented in Figure 5.3a, is higher than the maximum temperature in the y-direction coil configuration shown in Figure 5.3b. This effect occurs due to the heat being focused in the middle two plies, which are oriented in the same direction as the coil. This explanation is confirmed by the heat generated per ply. The more focused generation of heat results in a higher peak temperature.

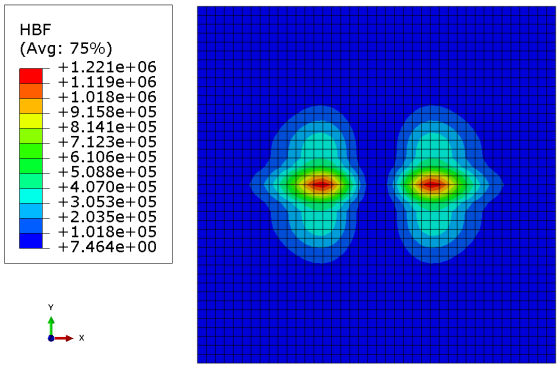

(a) The heat generated in the top ply, ply 1

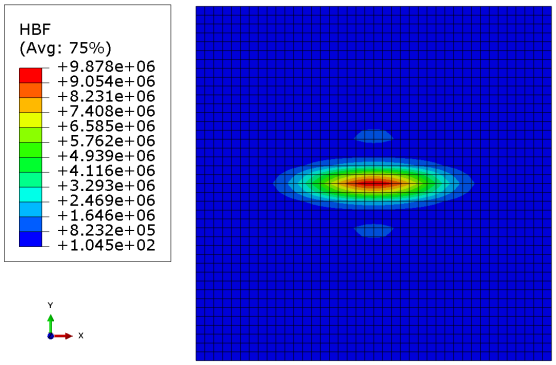

(b) The heat generated in ply 2

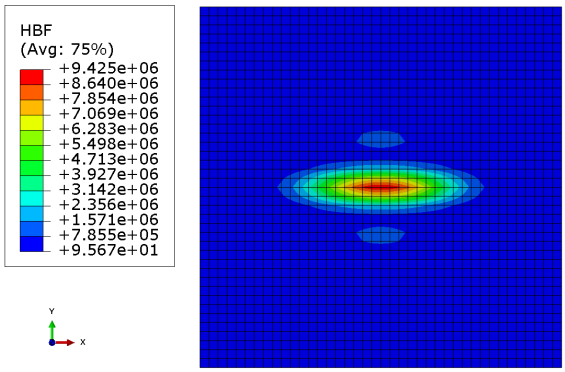

(c) The heat generated in ply 3

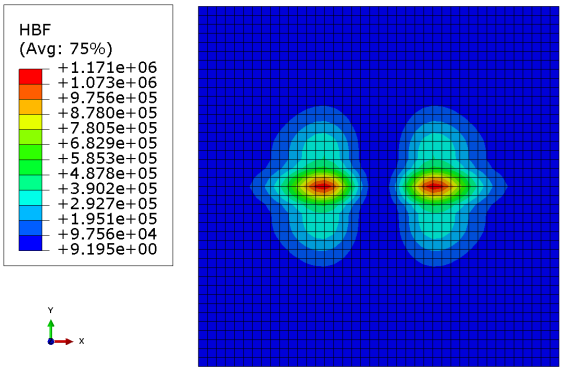

(d) The heat generated in ply 4

Figure 5.4: The heat generated in the validation plate with the coil in the x-direction in WelDone

The heating per ply in J/s is shown in Figure 5.4. In Figure 5.4a, the heating in the top ply is presented. This is low in comparison to the heating in the plies oriented in the x-direction (or the 0^o orientation), which are shown in Figures 5.4b and 5.4c, as the coil is positioned perpendicular to the fiber direction and the conductivity of the ply in this direction is relatively low. The model with the coil rotated to be in the y-direction is shown in Figure 5.5.

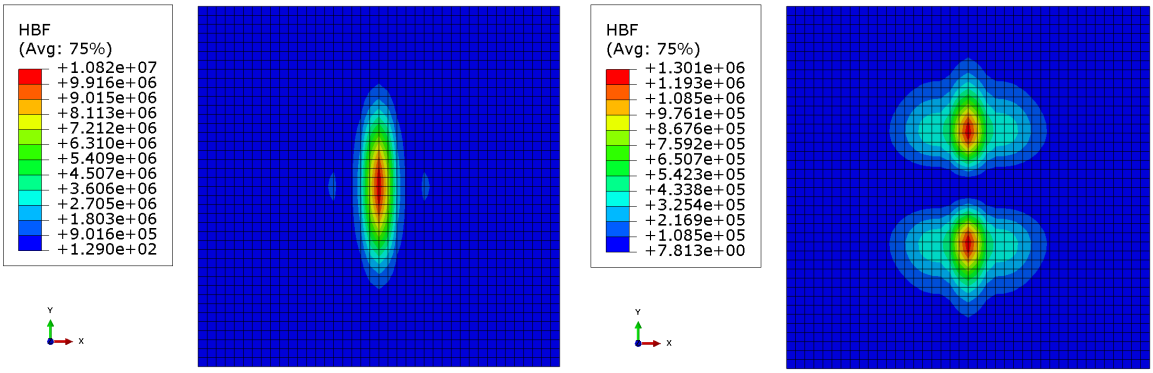

(a) The heat generated in the top ply, ply 1

(b) The heat generated in ply 2

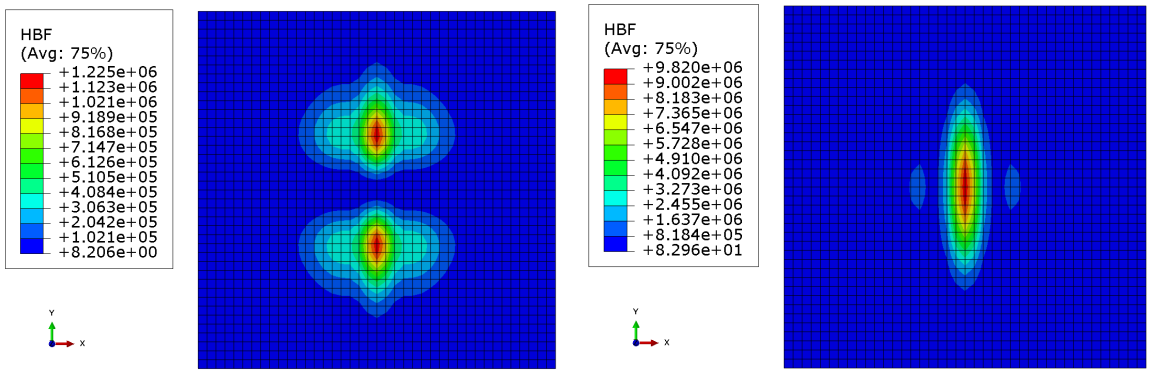

(c) The heat generated in ply 3

(d) The heat generated in ply 4

Figure 5.5: The heat generated in the validation laminate with the coil in the y-direction in WelDone and ABAQUS

The heat distributions presented in Figure 5.5 look akin but rotated when compared to Figure 5.4, which is expected. The outer plies of Figure 5.5 are similar to the inner plies of Figure 5.4 and vice versa. This is important, as this shows that the coil geometry and location is successfully decoupled from the global matrices and no unexpected phenomenon occur. In Figure 5.6 the same model is evaluated in COMSOL.

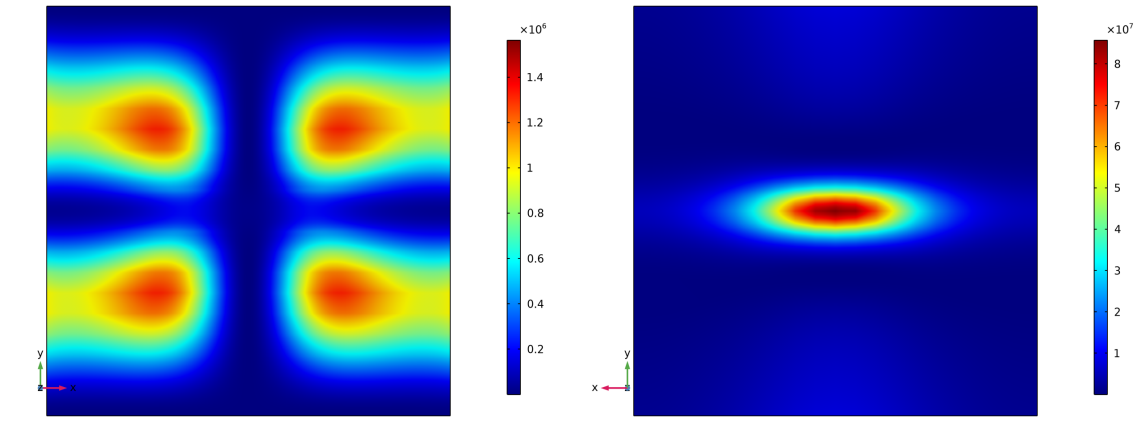

(a) The heat generated in the top ply, ply 1

(b) The heat generated in ply 2

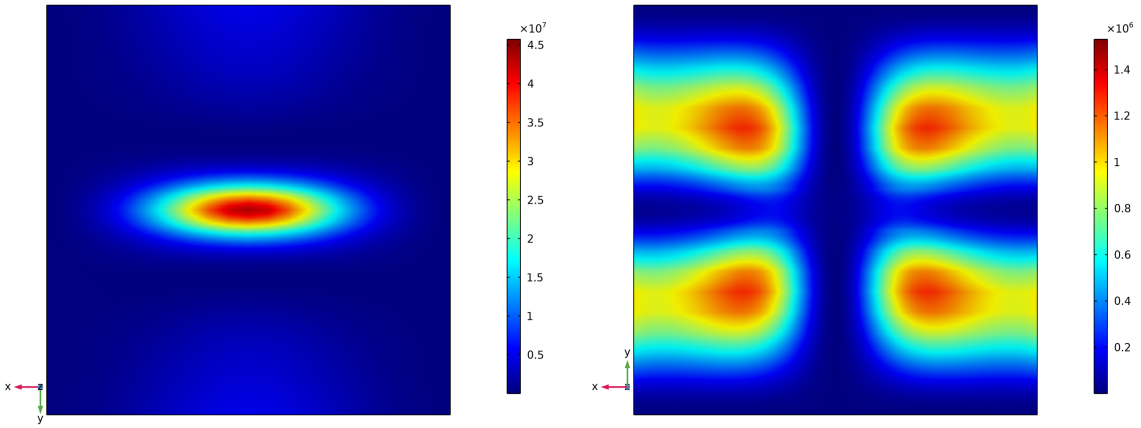

(c) The heat generated in ply 3

(d) The heat generated in ply 4

Figure 5.6: The heat generated in the validation plate with the coil in the x-direction in COMSOL

The heating patterns in the 0 plies, as shown in Figures 5.6b and 5.6c, look akin to the heat patterns shown in Figures 5.4b and 5.4c. The heating patterns in the 90 plies, as shown in Figures 5.4a and 5.4d, when compared to the heating pattern in Figures 5.6a and 5.6d can be observed to have significant differences. The former shows a singular hot spot located below where the coil ends, while the latter shows two hot spots perpendicularly offset from where the coil ends.

5.2 Validation on curved geometries

To validate the software on curved laminates, the same geometry, lay up and coil parameters, as presented in the previous section, Section 5.1, are used. The element definition for the 8-node hexahedral is used, as the 2-node brick elements cannot mesh the curved geometry. A curvature with a radius of 10 inches is introduced, as shown in Figure 5.7. In Figure 5.9 the coil is placed vertically, in the y-direction. In Figure 5.12 the coil is placed horizontally, in the x-direction. For reference, the same model was evaluated in COMSOL with the same parameters, the results are presented in 5.10.

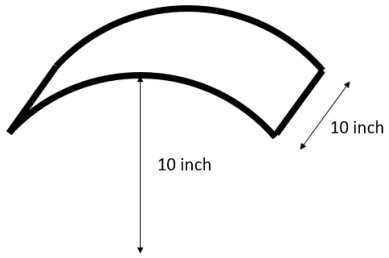

Figure 5.7: The curved plate model with coil

When examining Figure 5.9a, it is likely that the mesh is not fully converged. Examining at the middle of the plate and progressing outwards horizontally, the red area situated below the coil rapidly changes to an area where very low heating is observed, after which an area where more heating is observed. This happens in the span of one to two elements, these large changes over short distances in the magnetic field are not captured well by the elements unless the mesh density is increased. The rapid change in the magnetic field here is shown in Figure 5.8. In this figure, the large downward pointing arrows under the coil represent the large magnetic field, which quickly change when moving away from the coil, as can be seen by the changes in magnitude and direction of the arrows around the large downward pointing arrows under the coil. The heating distribution phenomenon is expected, as the conductivity is more in the plane perpendicular to the coil, and therefore more current is induced.

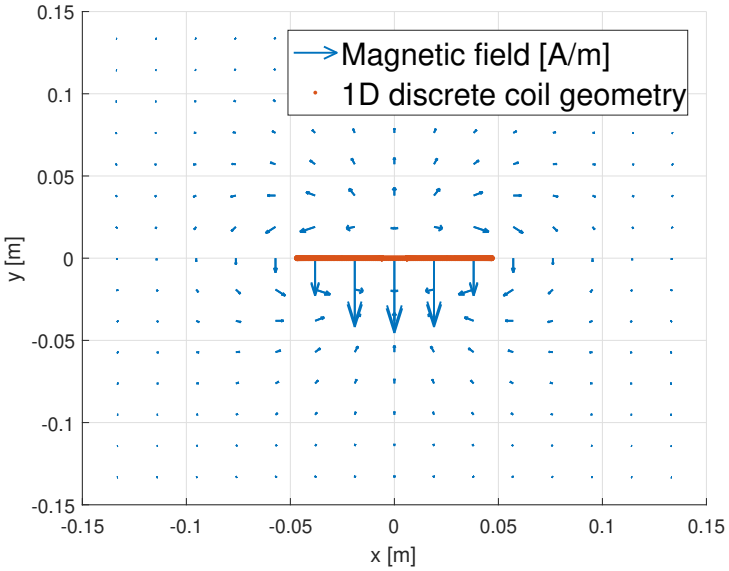

Figure 5.8: Rapid magnetic field change under the coil

In the next ply, Figure 5.9b shows a comparable trend to the heating trends as shown in Figures 5.10a and 5.10d. The heat patterns are rotated 90 degrees, which is expected, as in this simulation as ran in COMSOL the coil is in horizontal, or in the x-direction, whereas the Figure 5.9 is modeled with a vertical coil, or in the y-direction. In Figure 5.9b, the hot spot is more smeared out which is likely due to the same phenomenon as before, the conductivity is higher in the plane perpendicular to the magnetic field.

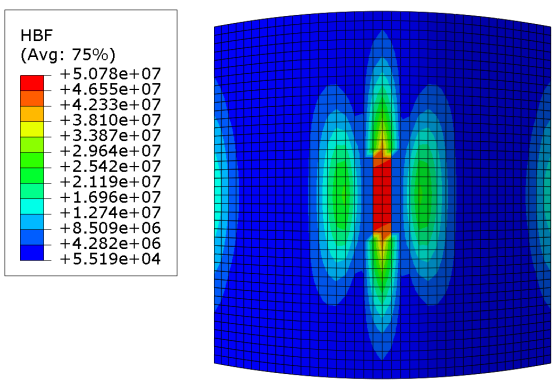

(a) The heat generated in the top ply, ply 1

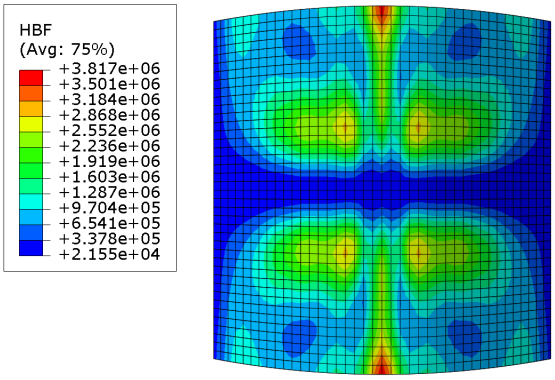

(b) The heat generated in ply 2

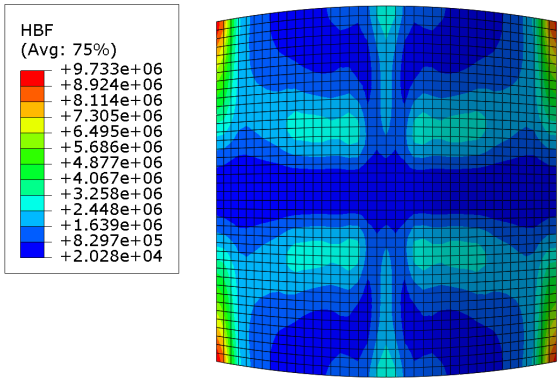

(c) The heat generated in ply 3

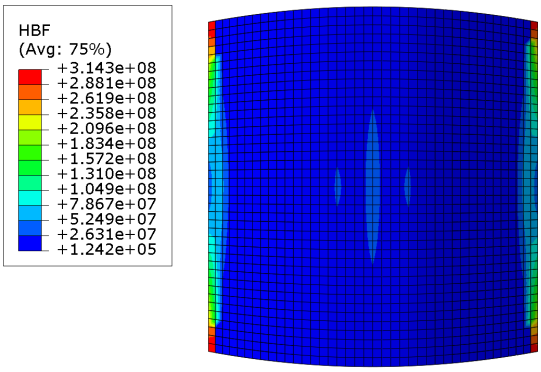

(d) The heat generated in ply 4

Figure 5.9: The heat generated in the validation plate with the coil in the y-direction in WelDone

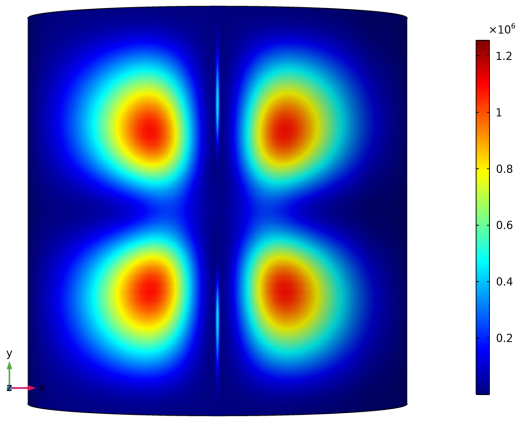

(a) The heat generated in the top ply, ply 1

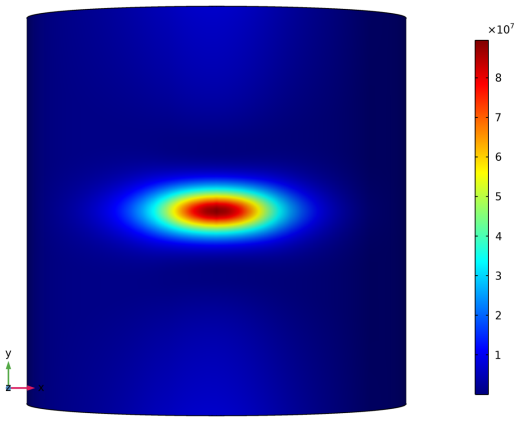

(b) The heat generated in ply 2

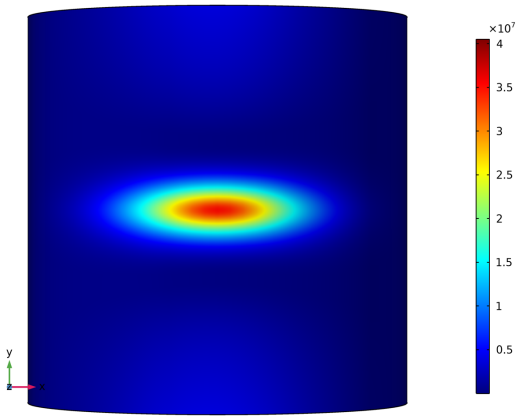

(c) The heat generated in ply 3

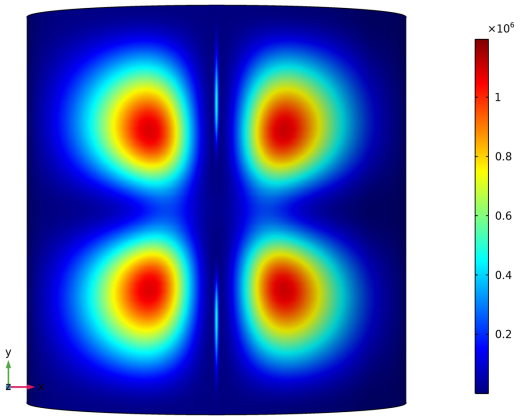

(d) The heat generated in ply 4

Figure 5.10: The heat generated in the validation plate with the coil in the x-direction in COMSOL

In Figures 5.9b, 5.9c and 5.9d the edges and corners to exhibit some unrealistic heating phenomenon. In Figure 5.9b, these phenomena do not interfere with the heat distribution pattern, however in the other plies shown in Figure 5.9c it does. To be able to interpret the heating patterns of Figures 5.9c and 5.9d, the unrealistic heating phenomena near the edges are removed, and the result is presented in Figure 5.11.

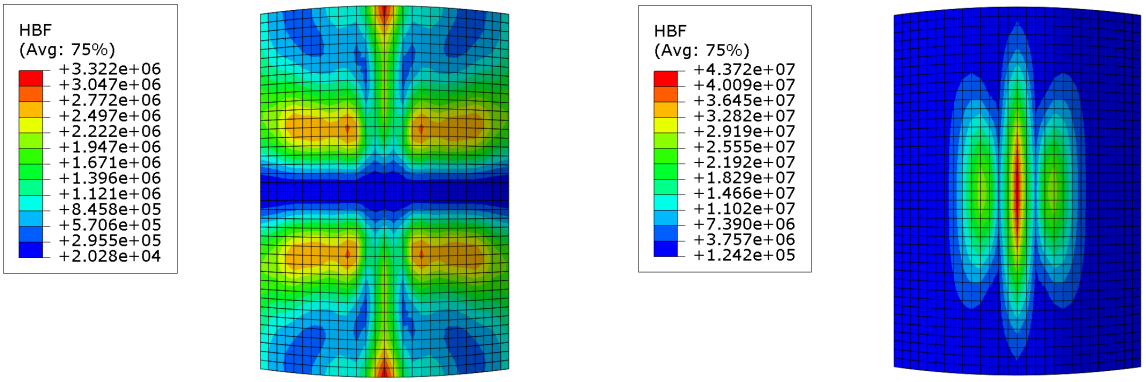

(a) The filtered heat generated in ply 4 (b) The filtered heat generated in ply 4

Figure 5.11: The filtered heat generated in the validation plate with the coil in the y-direction in WelDone and ABAQUS

After removing the excessive and unrealistic heating occurring at the edges and corners, in Figure 5.11a the heating pattern in the third ply is shown, which resembles the heating pattern in Figure 5.9b. Similarly, the heat pattern in Figure 5.11 approximates the heat pattern in Figure 5.9d. In this layer, the mesh is refined enough to accurately capture the modeled problem. This is likely because the bottom layer is exposed to a less intense magnetic field and thus the spatial gradient of the magnetic field is reduced, thus not requiring as dense a mesh as the first ply requires.

In Figure 5.12, the heat body losses are shown for the four different plies with the coil horizontal, along the x-axis. The last ply, ply 4, once more shows some effects in the corner, but these were filtered out in Figure 5.13. The two plies with the fiber direction parallel to the coil, ply 2 and 3, experience the most heating as expected, and the heating patterns remain the same. The perpendicular plies, ply 1 and 4, exhibit a clover-like heating pattern, similar to Figures 5.10a and 5.10d.

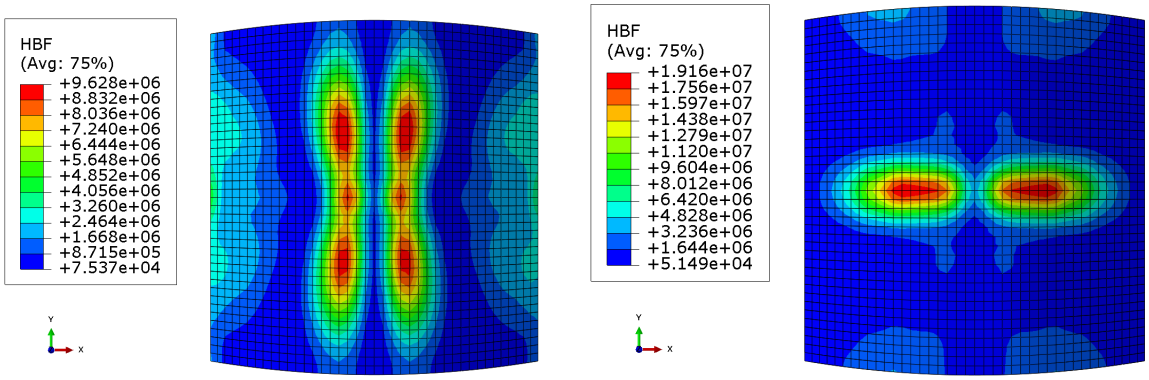

(a) The heat generated in the top ply, ply 1

(b) The heat generated in ply 2

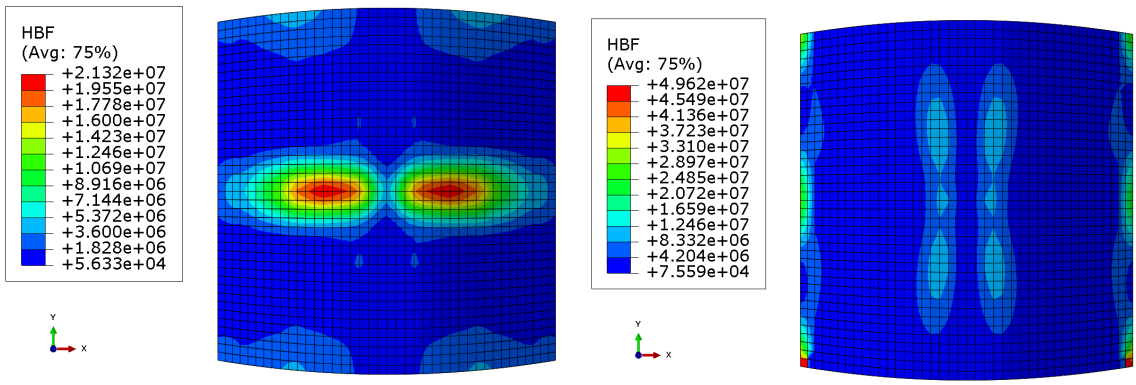

(c) The heat generated in ply 3

(d) The heat generated in ply 4

Figure 5.12: The heat generated in the validation plate with the coil in the x-direction in WelDone

These figures do not show the phenomenon observed in Figure 5.9a, likely due to the change in the heating being less significant in the first ply, and the gradient in the second ply is lower. From this, the conclusion can be drawn that, if the first ply of a simulation is expected to show significant heating, then the meshing density may need to be increased to accurately capture the heating behavior.

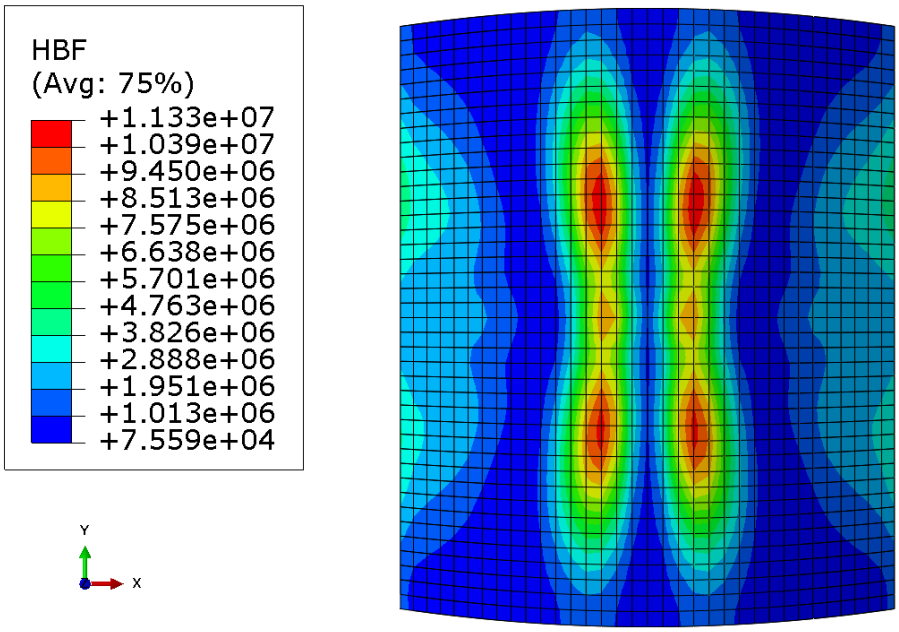

Figure 5.13: Heat generated in validation plate ply 4, see Figure 5.12, with the edges removed

Bibliography

[1] M. Holland, M. van Tooren, D. Barazanchy, and J. Pandher, "Modeling of induction heating of thermoplastic composites," *Journal of Thermoplastic Composite Materials*, 2020.

[2] U. A. Khashaba, T. A. Sebaey, F. F. Mahmoud, A. I. Selmy, and R. M. Hamouda, "Experimental and numerical analysis of pinned-joints composite laminates: Effects of stacking sequences," *Journal of Composite Materials*, vol. 47, pp. 3353–3366, 12 2013.

[3] Various, "Ampere Maxwell," 2022.

[4] W. Pilkey, *Mechanics of structures : variational and computational methods*. 2000 Corporate Blvd., N.W., Boca Raton, Florida: CRC Press, 1994.

[5] A. Masserey, J. Rappaz, R. Rozsnyo, and M. Swierkosz, "Numerical integration of the three-dimensional Green kernel for an electromagnetic problem," *Journal of Computational Physics*, vol. 205, no. 1, pp. 48–71, 2005.

[6] D. Brosius, "Thermosets vs. thermoplastics: Is the battle over? : CompositesWorld."

[7] J. Sloan, "Composites 2020: A multitude of markets: CompositesWorld."

[8] I. Chang and J. Lees, "Recent Development in Thermoplastic Composites: A Review of Matrix Systems and Processing Methods," tech. rep., du Pont de Nemours and Company, Inc., Wilmington, 1988.

[9] K. Mason, "Thermoplastic primary aerostructures take another step forward: CompositesWorld."

[10] A. Bossavit, *Computational electromagnetism : variational formulations, complementarity, edge elements*. San Diego: Academic Press, 1998.

[11] A. Bossavit and J. Vérité, "The "TRIFOU" code: Solving the 3-D eddy-currents problem by using H as state variable," *IEEE Transactions on Magnetics*, vol. 19, no. 6, pp. 2465–2470, 1983.

[12] M. Mori and M. Sugihara, "The double-exponential transformation in numerical analysis," *Journal of Computational and Applied Mathematics*, vol. 127, no. 1-2, pp. 287–296, 2001.

[13] O. Zienkiewicz and K. Morgan, *Finite Elements and Approximation*. A Wiley-Interscience publication, Wiley, 1983.

[14] M. Troughton, *Handbook of plastics joining : a practical guide*. Norwich, NY Cambridge, UK: William Andrew TWI/The Welding Institute, 2008.

[15] S. Mazumdar, *Composites manufacturing : materials, product, and process engineering*. CRC Press, 2002.

[16] M. Song, J. Kweon, J. Choi, J. Byun, M. Song, S. Shin, and T. Lee, "Effect of manufacturing methods on the shear strength of composite single-lap bonded joints," *Composite Structures*, vol. 92, no. 9, pp. 2194–2202, 2010.

[17] J. Mohan, A. Ivanković, and N. Murphy, "Effect of prepreg storage humidity on the mixed-mode fracture toughness of a co-cured composite joint," *Composites Part A: Applied Science and Manufacturing*, vol. 45, pp. 23–34, 2013.

[18] N. Encinas, B. R. Oakley, M. A. Belcher, K. Y. Blohowiak, R. G. Dillingham, J. Abenojar, and M. A. Martínez, "Surface modification of aircraft used composites for adhesive bonding," *International Journal of Adhesion and Adhesives*, vol. 50, pp. 157–163, 2014.

[19] L. F. da Silva, R. J. Carbas, G. W. Critchlow, M. A. Figueiredo, and K. Brown, "Effect of material, geometry, surface treatment and environment on the shear strength of single lap joints," *International Journal of Adhesion and Adhesives*, vol. 29, no. 6, pp. 621–632, 2009.

[20] M. Kanerva and O. Saarela, "The peel ply surface treatment for adhesive bonding of composites: A review," *International Journal of Adhesion and Adhesives*, vol. 43, pp. 60–69, 2013.

[21] S. Azari, M. Papini, and J. K. Spelt, "Effect of surface roughness on the performance of adhesive joints under static and cyclic loading," *Journal of Adhesion*, vol. 86, no. 7, pp. 742–764, 2010.

[22] S. Budhe, M. Banea, S. de Barros, and L. da Silva, "An updated review of adhesively bonded joints in composite materials," *International Journal of Adhesion and Adhesives*, vol. 72, no. October 2016, pp. 30–42, 2017.

[23] M. D. Banea, F. S. De Sousa, L. F. Da Silva, R. D. Campilho, and A. M. De Pereira, "Effects of temperature and loading rate on the mechanical properties of a high temperature epoxy adhesive," *Journal of Adhesion Science and Technology*, vol. 25, no. 18, pp. 2461–2474, 2011.

[24] P. Hu, X. Han, W. D. Li, L. Li, and Q. Shao, "Research on the static strength performance of adhesive single lap joints subjected to extreme temperature environment for automotive industry," *International Journal of Adhesion and Adhesives*, vol. 41, pp. 119–126, 2013.

[25] D. Gleich, M. van Tooren, and A. Beukers, "Analysis and evaluation of bondline thickness effects on failure load in adhesively bonded structures," *Journal of Adhesion Science and Technology*, vol. 15, pp. 1091–1101, 01 2001.

[26] L. Silva, T. Rodrigues, M. de Figueiredo, M. De Moura, and J. Chousal, "Effect of adhesive type and thickness on the lap shear strength," *The Journal of Adhesion*, vol. 82, pp. 1091–1115, 11 2006.

[27] A. Benatar and T. Gutowski, "Method for fusion bonding thermoplastic composites," *SAMPE Q.; (United States)*, vol. 18:1, 10 1986.

[28] A. Wedgewood and P. Hardy, "Induction welding of thermoset composite adherends using thermoplastic interlayers and susceptors," *Technology Transfer in a Global Community*, pp. 850–861, 1996.

[29] Y. Pleshivtseva and E. Rapoport, *Optimal control of induction heating processes*. Boca Raton, Florida: CRC/Taylor & Francis, 2007.

[30] C. Ageorges, L. Ye, and M. Hou, "Advances in fusion bonding techniques for joining thermoplastic matrix composites: A review," *Composites - Part A: Applied Science and Manufacturing*, vol. 32, no. 6, pp. 839–857, 2001.

[31] T. J. Ahmed, D. Stavrov, H. E. Bersee, and A. Beukers, "Induction welding of thermoplastic composites-an overview," *Composites Part A: Applied Science and Manufacturing*, vol. 37, no. 10, pp. 1638–1651, 2006.

[32] A. Yousefpour, M. Hojjati, and J. Immarigeon, "Fusion bonding/welding of thermoplastic composites," *Journal of Thermoplastic Composite Materials*, vol. 17, no. 4, pp. 303–341, 2004.

[33] T. Bayerl, M. Duhovic, P. Mitschang, and D. Bhattacharyya, "The heating of polymer composites by electromagnetic induction - A review," *Composites Part A: Applied Science and Manufacturing*, vol. 57, no. 2014, pp. 27–40, 2014.

[34] F. Lionetto, S. Pappadà, G. Buccoliero, and A. Maffezzoli, "Finite element modeling of continuous induction welding of thermoplastic matrix composites," *Materials and Design*, vol. 120, pp. 212–221, 2017.

[35] J. Maxwell, "A Treatise on Electricity and Magnetism," *Nature*, vol. 7, pp. 478–480, Apr. 1873.

[36] V. Rudnev, D. Loveless, R. Cook, and M. Black, "Handbook of Induction Heating," *Handbook of Induction Heating*, 2002.

[37] H. Kim, S. Yarlagadda, J. Gillespie, N. Shevchenko, and B. Fink, "A study on the induction heating of carbon fiber reinforced thermoplastic composites," *Advanced Composite Materials*, vol. 11, no. 1, pp. 71–80, 2002.

[38] D. Rodger and J. Eastham, "A formulation for low frequency eddy current solutions," *IEEE Transactions on Magnetics*, vol. 19, no. 6, pp. 2443–2446, 1983.

[39] J. S. van Welij, "Calculation of eddy currents in terms of H on hexahedra," *IEEE Transactions on Magnetics*, vol. 21, no. 6, pp. 2239–2241, 1985.

[40] R. Hiptmair, "Symmetric coupling for eddy current problems," *SIAM Journal on Numerical Analysis*, vol. 40, no. 1, pp. 41–65, 2002.

[41] C. J. Carpenter, "Comparison of Alternative Formulations of 3-Dimensional Magnetic-Field and Eddy-Current Problems At Power Frequencies.," *Proceedings of the Institution of Electrical Engineers*, vol. 124, no. 11, pp. 1026–1034, 1977.

[42] T. Morisue, "Magnetic vector potential and electric scalar potential in three-dimensional eddy current problem," *IEEE TRANSACTIONS ON MAGNETIC*, vol. 18, no. 3, pp. 531–535, 1982.

[43] F. Matsuoka and A. Kameari, "Calculation of three dimensional eddy current by fem-bem coupling method," *IEEE Transactions on Magnetics*, vol. 24, no. 1, pp. 182–185, 1988.

[44] A. Bossavit and J. Vérité, "A mixed FEM-BIEM method to solve 3-D eddy-current problems," *IEEE Transactions on Magnetics*, vol. 18, no. 2, pp. 431–435, 1982.

[45] A. Rodriguez and A. Valli, *Eddy current approximation of Maxwell Equations : theory, algorithms and applications*. Milan London: Springer, 2010.

[46] J. Stewart, *Stewart's Calculus - 8th edition*. Cengage Learning, 8th ed., 2016.

[47] G. Korn and T. Korn, *Mathematical handbook for scientists and engineers definitions, theorems, and formulas for reference and review*. New York: McGraw-Hill, 1968.

[48] R. Rodríguez, *Numerical Approximation of Maxwell Equations in Low-Frequency Regime*, vol. 2148. Springer, 2015.

[49] H. M. Schey, *Div, Grad, Curl, and All That. An Informal Text on Vector Calculus*. W. W. Norton & Company, fourth edi ed., 2005.

[50] J. N. Reddy, "An Introduction to the Finite Element Method," *Journal of Pressure Vessel Technology*, vol. 111, pp. 348–349, aug 1989.

[51] G. Chen and J. Zhou, *Boundary Element Methods with Applications to Nonlinear Problems*, vol. 7. Atlantis Studies in Mathematics for Engineering and Science, 2010.

[52] Z. Ren, F. Bouillault, A. Razek, and J. C. Verite, "An efficient semi-analytical integration procedure in three-dimensional boundary integral method," *COMPEL - The international journal for computation and mathematics in electrical and electronic engineering*, vol. 7, no. 4, pp. 195–205, 1988.

[53] J. Nedelec, "Mixed finite elements in R3," *Numerische Mathematik*, vol. 35, no. 3, pp. 315–341, 1980.

[54] K. Miyata, "Magnetic Field Analysis by the Edge Element FEM," *IEEJ Transactions on Electronics, Information and Systems*, vol. 124, no. 7, pp. 1404–1409, 2004.

[55] O. C. Zienkiewicz, R. L. Taylor, and J. Z. Zhu, *The Finite Element Method Volume 1 : Its Basis & Fundamentals (sixth edition)*. Butterworth-Heinemann, 2005.

[56] A. E. Yilmaz and M. Kuzuoglu, "Comparison of linear and quadratic hexahedral edge elements in electromagnetic scattering problems," *AEU - International Journal of Electronics and Communications*, vol. 62, no. 8, pp. 582–587, 2008.

[57] J. Jin, "The Finite Element Method in Electromagnetics, 3rd edition," *Journal of Chemical Information and Modeling*, p. 380, 2014.

[58] A. Bossavit, "Whitney forms: A class of finite elements for three-dimensional computations in electromagnetism," *IEE Proceedings A: Physical Science. Measurement and Instrumentation. Management and Education. Reviews*, vol. 135 pt A, no. 8, pp. 493–500, 1988.

[59] R. Burden and J. Faires, *Numerical Analysis*. Boston: Brooks/Cole, Cengage Learning, 2011.

[60] S. Balac and G. Caloz, "Induced magnetic field computations using a boundary integral formulation," *Applied Numerical Mathematics*, vol. 41, pp. 345–367, jun 2002.

[61] G. Xie, F. Zhou, J. Zhang, X. Zheng, and C. Huang, "New variable transformations for evaluating nearly singular integrals in 3D boundary element method," *Engineering Analysis with Boundary Elements*, vol. 37, no. 9, pp. 1169–1178, 2013.

[62] H. Ma and N. Kamiya, "Distance transformation for the numerical evaluation of near singular boundary integrals with various kernels in boundary element method," *Engineering Analysis with Boundary Elements*, vol. 26, pp. 329–339, 2002.

[63] Z. Ren, F. Bouillault, A. Razek, and J. C. Verite, "Comparison of different boundary integral formulations when coupled with finite elements in three dimensions," *IEE Proceedings A: Physical Science. Measurement and Instrumentation. Management and Education. Reviews*, vol. 135 pt A, no. 8, pp. 501–507, 1988.

[64] H. T. Rathod, K. V. Nagaraja, B. Venkatesudu, and N. L. Ramesh, "Gauss Legendre quadrature over a triangle," *Journal of the Indian Institute of Science*, vol. 84, no. 5, pp. 183–188, 2004.

[65] P. C. Hammer, O. J. Marlowe, and A. H. Stroud, "Numerical integration over simplexes and cones," *Mathematics of Computation*, vol. 10, pp. 130–130, sep 1956.

[66] A. H. Stroud and D. Secrest, "Gaussian Quadrature Formulas," *Zeitschrift fur angewandte Mathematik und Mechanik*, vol. 47, no. 2, pp. 138–139, 1967.

[67] A. Eddib and D. Chung, "Electric permittivity of carbon fiber," *Carbon*, vol. 143, pp. 475–480, 2019.

[68] J. Alsalaet, "Processing of near singular integrals in 3d boundary elements method," 2018.

Appendix A

2D derivation of the gradient matrix

The gradient of the shape functions N is required for the $\boldsymbol{M}$ matrices, as shown in Eqn. 2.3.58. The gradient is defined as:

$$\vec{\nabla}\vec{N} = \begin{bmatrix} \frac{\partial N_1}{\partial x} & \frac{\partial N_2}{\partial x} \\ \frac{\partial N_1}{\partial y} & \frac{\partial N_2}{\partial y} \end{bmatrix} \tag{A.0.1}$$

The shape functions are functions of the natural coordinate system. In the case of a hexahedron ξ and η, for a tetrahedral it is λ_1 and λ_2. Additionally, we have mapping functions relating the natural coordinate to the global coordinates, $\xi(x, y)$ and $\eta(x, y)$. Therefore, the derivative of the shape functions ξ and η to x and y can be found, also known as the Jacobian [55].

$$\boldsymbol{J} = \begin{bmatrix} \frac{\partial x}{\partial \xi} & \frac{\partial y}{\partial \xi} \\ \frac{\partial x}{\partial \eta} & \frac{\partial y}{\partial \eta} \end{bmatrix} \tag{A.0.2}$$

In Eqn. A.0.2, the variables x and y are defined by:

$$\begin{aligned} x &= \sum N_i x_i \\ y &= \sum N_i y_i \end{aligned} \tag{A.0.3}$$

In this equation, the N_i are defined by the element type and order of the element. The terms as described in Eqn. A.0.2 can now be found.

Multiplying the matrix J as defined in Eqn. A.0.2 with the derivatives of the

shape functions N_1 and N_2, the gradient of the N_1 and N_2 as shown in Eqn. A.0.1 can be found. The matrix to achieve that is found to be:

$$\begin{bmatrix} \frac{\partial N_1}{\partial \xi} & \frac{\partial N_2}{\partial \xi} \\ \frac{\partial N_1}{\partial \eta} & \frac{\partial N_2}{\partial \eta} \end{bmatrix} \tag{A.0.4}$$

an undefined matrix $\boldsymbol{G}$ is defined such that:

$$\vec{\nabla}\vec{N} = \boldsymbol{G} \begin{bmatrix} \frac{\partial N_1}{\partial \xi} & \frac{\partial N_2}{\partial \xi} \\ \frac{\partial N_1}{\partial \eta} & \frac{\partial N_2}{\partial \eta} \end{bmatrix} \tag{A.0.5}$$

Evidently, from the equation above, the following can be found:

$$\boldsymbol{G} = \begin{bmatrix} \frac{\partial \xi}{\partial x} & \frac{\partial \eta}{\partial x} \\ \frac{\partial \xi}{\partial y} & \frac{\partial \eta}{\partial y} \end{bmatrix} \tag{A.0.6}$$

Comparing Eqn. A.0.2 with Eqn. A.0.6 yields a way to find $\boldsymbol{G}$:

$$\boldsymbol{G} = (\boldsymbol{J})^{-1} \tag{A.0.7}$$

Appendix B

Proof for neglecting the displacement current

The displacement current is neglected during the induction process, this is based on the assumption that the excitation frequency does not exceed 500 kHz. This assumption is known as the magneto-quasistationary limit [42], when the frequency is low enough, the dielectric contribution or the contribution of displacement currents $\frac{\partial \boldsymbol{D}}{\partial t}$ is significantly smaller than the contribution of the current density $\boldsymbol{J}$.

This can be proven through the following reasoning:

As per Amperes Law, Eqn. 2.3.6, the curl of the $\boldsymbol{H}$ field is equal to the current J added to the displacement current: $\nabla \times H = J + i\omega D$. Here, the harmonic assumption is already applied, the time derivative is rewritten as the $i\omega D$ term where w is the angular frequency. Now substituting in Ohm's law $J = J_S + \sigma E$, where J_S is the source current and σ is the conductivity. The material equation relating the electric intensity field $\boldsymbol{E}$ to the electric flux field $\boldsymbol{D}$ through ϵ the electric permittivity: $\boldsymbol{D} = \epsilon \boldsymbol{E}$. The resulting equation is: $rot(H) = J_S + \sigma \boldsymbol{E} + i\omega\epsilon \boldsymbol{E}$.

- In air, the conductivity is 0, therefore, the displacement current ($iw\epsilon E$) is negligible if the source current J_S is significantly larger than the displacement current.

- In the conductive domain, the opposite is true: there is no source current, and the displacement current is negligible if $\sigma \boldsymbol{E}$ is significantly larger than the displacement current $i\omega\epsilon \boldsymbol{E}$. In the conductive domain, the ratio $\frac{\epsilon w}{\sigma}$ will dictate the validity of the assumption. The assumption can be made that the magnitude

of the source current J_S is in the same order of magnitude as the electric field, and thus, if the displacement current can be neglected in the conductive domain, it can also be neglected in the non-conductive domain (and vice-versa). The epsilon here is around the order of the permittivity of free space: $1/(36{\cdot}10^9{\cdot}3.14)$. For PEEK, the relative permittivity is around 3-4 and for carbon fibers it can reach up to 5000 [67]. Finally, the electrical conductivity is around $10,000$ S/m. This yields: $(\epsilon f)\,\sigma = f \cdot 2.778 \cdot 10^{-11}$. In conclusion, this means that, as a first estimate, the contribution of the displacement current is $277,778$ times smaller than the contribution of the contribution of the source current/electricity field at 1 MHz. Therefore, the displacement field can be neglected. At a frequency of $360Mhz$, the contribution of the displacement current is 1% with respect to the term $\boldsymbol{\sigma E}$, at which point neglecting the displacement current may become questionable.

Appendix C

8 node integration results

In this appendix, the numerical integration of the $\boldsymbol{M}$ matrix is explored. The equations for the matrix, as presented in Section 2.3.6, and repeated in Eqn. C.0.1:

$$\begin{aligned} M^a_{ee} &= \iiint_{\Omega_a} \mu_a \vec{N}_k \cdot \vec{N}_l \; dV \\ M^a_{ne} = M^a_{en} &= \iiint_{\Omega_a} \mu_a \left(\vec{\nabla} N_i\right) \cdot \vec{N}_k \; dV \\ M^a_{nn} &= \iiint_{\Omega_a} \mu_a \left(\vec{\nabla} N_i\right) \cdot \left(\vec{\nabla} N_i\right) \; dV \end{aligned} \tag{C.0.1}$$

For the 8-node hexahedral element, these equations are numerically integrated with the Gaussian quadrature rule and the Simpsons rule. The results of the numerical models are presented in Table C.1, this table contains the error per element of the M_{ee} matrix for the 1-node Gaussian quadrature with respect to the cubic solution in %. The relative errors range from 12.5 % to 125 %, thus the 1-node Gaussian quadrature rule is insufficient.

Similarly, the results for the 2-node Gaussian quadrature are presented in Table C.2. The 2-node quadrature is clearly sufficiently accurate, as the maximum error is less than $1e-13$ %. The downside of this numerical integration method is that the resulting functions are relatively large and cumbersome, the computational time was increased significantly. To compare this to a similar but less resource intensive numerical integration method, Simpson's quadrature is also applied.

The accuracy of Simpson's quadrature is shown in Table C.3, the maximum error

Table C.1: Relative error of the numerical integration with a 1-node Gaussian quadrature rule with respect to the cubic symbolically integrated solution

43.75	12.5	125	12.5	-	-	-	-	-	-	-	-
12.5	43.75	12.5	125	-	-	-	-	-	-	-	-
125	12.5	43.75	12.5	-	-	-	-	-	-	-	-
12.5	125	12.5	43.75	-	-	-	-	-	-	-	-
-	-	-	-	43.75	12.5	125	12.5	-	-	-	-
-	-	-	-	12.5	43.75	12.5	125	-	-	-	-
-	-	-	-	125	12.5	43.75	12.5	-	-	-	-
-	-	-	-	12.5	125	12.5	43.75	-	-	-	-
-	-	-	-	-	-	-	-	43.75	12.5	125	12.5
-	-	-	-	-	-	-	-	12.5	43.75	12.5	125
-	-	-	-	-	-	-	-	125	12.5	43.75	12.5
-	-	-	-	-	-	-	-	12.5	125	12.5	43.75

Table C.2: Relative error of the numerical integration with a 2-node Gaussian quadrature rule with respect to the cubic symbolically integrated solution

0.0381e-12	0.1016e-12	0.1525e-12	0.1016e-12	-	-	-	-	-	-	-	-
0.1016e-12	0.1779e-12	0.1525e-12	0.1525e-12	-	-	-	-	-	-	-	-
0.1525e-12	0.1525e-12	0.1016e-12	0.1398e-12	-	-	-	-	-	-	-	-
0.1016e-12	0.1525e-12	0.1398e-12	0.1906e-12	-	-	-	-	-	-	-	-
-	-	-	-	0.0732e-12	0.0366e-12	0.0549e-12	0.0183e-12	-	-	-	-
-	-	-	-	0.0366e-12	0.0549e-12	0.0915e-12	0.0549e-12	-	-	-	-
-	-	-	-	0.0549e-12	0.0915e-12	0.1830e-12	0.1281e-12	-	-	-	-
-	-	-	-	0.0183e-12	0.0549e-12	0.1281e-12	0.0549e-12	-	-	-	-
-	-	-	-	-	-	-	-	0.0133e-12	0	0.0400e-12	0
-	-	-	-	-	-	-	-	0	0.0133e-12	0.0533e-12	0.0400e-12
-	-	-	-	-	-	-	-	0.0400e-12	0.0533e-12	0.1332e-12	0.0533e-12
-	-	-	-	-	-	-	-	0	0.0400e-12	0.0533e-12	0.0133e-12

found with respect to the cubic symbolically integrated M_{ee} matrix of the 2-node element is less than $1e-13$ %. The quadrature rule is as precise as a 2-node Gaussian quadrature rule, however the computational resources required are significantly less.

Table C.3: Relative error of the numerical integration with the Simpson quadrature rule with respect to the cubic symbolically integrated solution

0.0508e-12	0.0381e-12	0.0508e-12	0.0508e-12	-	-	-	-	-	-	-	-
0.0381e-12	0.0508e-12	0.0635e-12	0.0508e-12	-	-	-	-	-	-	-	-
0.0508e-12	0.0635e-12	0.1016e-12	0.1525e-12	-	-	-	-	-	-	-	-
0.0508e-12	0.0508e-12	0.1525e-12	0.1271e-12	-	-	-	-	-	-	-	-
-	-	-	-	0.0183e-12	0.0366e-12	0.0366e-12	0.0366e-12	-	-	-	-
-	-	-	-	0.0366e-12	0.0366e-12	0	0.0366e-12	-	-	-	-
-	-	-	-	0.0366e-12	0	0.0183e-12	0.0732e-12	-	-	-	-
-	-	-	-	0.0366e-12	0.0366e-12	0.0732e-12	0.0366e-12	-	-	-	-
-	-	-	-	-	-	-	-	0.0133e-12	0.0400e-12	0.0533e-12	0.0533e-12
-	-	-	-	-	-	-	-	0.0400e-12	0.0133e-12	0.0133e-12	0.0533e-12
-	-	-	-	-	-	-	-	0.0533e-12	0.0133e-12	0	0.0400e-12
-	-	-	-	-	-	-	-	0.0533e-12	0.0533e-12	0.0400e-12	0.0266e-12

Appendix D

Notes on the directionality of tetrahedral shape functions

The edge shape functions, as defined in Section 3.2, are directional. In the hexahedral element, this does not pose a problem, however, when evaluating the tetrahedral elements, it is possible that the local and global orientation of the edge oppose one another. In this appendix, an example in 2D is presented in Figure D.1

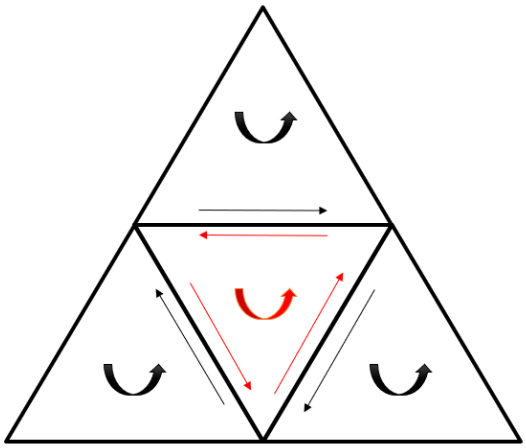

Figure D.1: 2D example of conflicting edge orientations

In Figure D.1 triangular surface elements are presented; in these elements the edge functions are all in the same direction, i.e. counterclockwise positive. If the middle (red) triangle drives the global orientation of the edges in that element. When adding to the global matrices the contribution of the adjacent triangular elements, the contribution will be in the opposite direction. This problem can be solved by implementing a matrix relating the local edge orientation to the global edge orientation. The ma-

trix element is -1 if the global and local edge are defined in the opposite direction, otherwise the element is 1.

Appendix E

Generating the element matrices $\boldsymbol{M}^a$ and $\boldsymbol{N}^a$ in MATLAB

In this appendix, the derivation of the element matrices $\boldsymbol{M}^a$ and $\boldsymbol{N}^a$ for the 8-node element were created. The exact implementation depends heavily on the type of element and the method of integration.

```
1
2  %% Define symbol variables
3  % Define the inputs as symbols
4  syms x1 x2 x3 x4 x5 x6 x7 x8
5  syms y1 y2 y3 y4 y5 y6 y7 y8
6  syms z1 z2 z3 z4 z5 z6 z7 z8
7  % Define the symbols of integration
8  syms xi eta zeta
9
10 % Optional define dependencies of node locations, here the 8-20 ...
       node is created.
11 XN = [x1 x2 x3 x4 x5 x6 x7 x8 (x1+x2)/2 (x2+x3)/2 (x3+x4)/2 ...
       (x4+x1)/2 (x5+x6)/2 (x6+x7)/2 (x7+x8)/2 (x8+x5)/2 (x1+x5)/2 ...
       (x2+x6)/2 (x3+x7)/2 (x4+x8)/2 ;
12         y1 y2 y3 y4 y5 y6 y7 y8 (y1+y2)/2 (y2+y3)/2 (y3+y4)/2 ...
               (y4+y1)/2 (y5+y6)/2 (y6+y7)/2 (y7+y8)/2 (y8+y5)/2 ...
               (y1+y5)/2 (y2+y6)/2 (y3+y7)/2 (y4+y8)/2 ;
13         z1 z2 z3 z4 z5 z6 z7 z8 (z1+z2)/2 (z2+z3)/2 (z3+z4)/2 ...
```

```
            (z4+z1)/2 (z5+z6)/2 (z6+z7)/2 (z7+z8)/2 (z8+z5)/2 ...
            (z1+z5)/2 (z2+z6)/2 (z3+z7)/2 (z4+z8)/2 ];


%% Hard code the geometry of the element
% Define the locations of the nodes in the iso-parametric space
xiN=   [-1,  1,  1, -1, -1,  1, 1, -1,  0,  1,  0, -1,  0, 1, 0, ...
    -1, -1,  1, 1, -1];
etaN=  [-1, -1,  1,  1, -1, -1, 1,  1, -1,  0,  1,  0, -1, 0, 1,  ...
    0, -1, -1, 1,  1];
zetaN= [-1, -1, -1, -1,  1,  1, 1,  1, -1, -1, -1, -1,  1, 1, 1,  ...
    1,  0,  0, 0,  0];

% Define the edge mapping in each direction
edge_map_xi = [1 9; 9 2; 4 11; 11 3; 5 13; 13 6; 8 15; 15 7;      ...
    12 10; 17 18; 20 19; 16 14];
edge_map_eta = [1 12; 12 4; 2 10; 10 3; 5 16; 16 8; 6 14; 14 7; ...
        9 11; 17 20; 18 19; 13 15];
edge_map_zeta = [1 17; 17 5; 2 18; 18 6; 3 19; 19 7; 4 20; 20 8; ...
       9 13; 12 16; 10 14; 11 15];
% Concatenate the edge mapping
edge_map = [edge_map_xi; edge_map_eta; edge_map_zeta];
% Define the total number of edges
numberofedges = length(edge_map(:,1));

% For each edge find the mid point of the edge
for i = 1:numberofedges
    % The two nodes associated with the edge
    i1 = edge_map(i,1);
    i2 = edge_map(i,2);

    % finding the xi eta zeta-coordinates of the mid points of ...
        the edge
```

```
38      xiE(i) = (xiN(i1) + xiN(i2)) / 2;
39      etaE(i) = (etaN(i1) + etaN(i2)) / 2;
40      zetaE(i) = (zetaN(i1) + zetaN(i2)) / 2;
41  end
42
43  %% Define the nodal shape functions of the element
44  for i = 1:8
45      N_node(i) = 1/8 * (1 + xiN(i)*xi)*(1 + etaN(i)*eta)*(1 + ...
            zetaN(i)*zeta) * (xiN(i)*xi + etaN(i)*eta + zetaN(i)*zeta ...
            - 2);
46  end
47
48  for i = 9:2:15
49      N_node(i) = 1/4 * (1 - xi^2)*(1 + etaN(i)*eta)*(1 + ...
            zetaN(i)*zeta);
50  end
51
52  for i = 10:2:16
53      N_node(i) = 1/4 * (1 + xiN(i)*xi)*(1 - eta^2)*(1 + ...
            zetaN(i)*zeta);
54  end
55
56  for i = 17:1:20
57      N_node(i) = 1/4 * (1 + xiN(i)*xi)*(1 + etaN(i)*eta)*(1 - zeta^2);
58  end
59
60
61  %% Calculating the J and G matrices
62  dN_node_xi = diff(N_node, xi);
63  dN_node_eta = diff(N_node, eta);
64  dN_node_zeta = diff(N_node, zeta);
65
66  J = [dN_node_xi; dN_node_eta; dN_node_zeta]*XN.';
```

```
67 J = simplify(J);
68 fprintf("J found\n")
69 toc
70
71 toc
72 detJ = det(J);
73 fprintf("detJ found \n")
74
75 Jinv = inv(J);
76 fprintf("Jinv found \n")
77
78 % Calculate the gradient of the transformation action
79 G = (Jinv).';
80 % G = simplify(G);
81
82 % Calculate the gradient of the shape functions
83 gradNN=G*[dN_node_xi;dN_node_eta;dN_node_zeta];
84 % implementation of 8.108 through 8.110 for p = 2
85
86 GXi = G*[1; 0; 0];
87 GEta = G*[0; 1; 0];
88 GZeta = G*[0; 0; 1];
89
90
91
92 %% Define the edge shape function
93 % https://www.sciencedirect.com/science/article/
94 % pii/S1434841107001501#bib2
95 % "Comparison of linear and quadratic hexahedral edge elements in
96 % electromagnetic scattering problems"
97
98 % In xi direction
99 for i = 1:8
```

```
100     N_edge(:,i) = 1/8 * (1 + etaE(i) * eta) * (1 + zetaE(i) * ...
            zeta) * (xiE(i)*xi + etaE(i)*eta + zetaE(i)*zeta - 1) * GXi;
101 end
102
103 for i = 9:3:12
104     N_edge(:,i) = 1/4 * (1 + zetaE(i) * zeta) * (1 - eta^2) * GXi;
105 end
106
107 for i = 10:11
108     N_edge(:,i) = 1/4 * (1 + etaE(i) * eta) * (1 - zeta^2) * GXi;
109 end
110
111
112 % In eta direction
113 for i=13:20
114     N_edge(:,i) = 1/8 * (1 + xiE(i) * xi) * (1 + zetaE(i) * zeta) ...
            * (xiE(i)*xi + etaE(i)*eta + zetaE(i)*zeta - 1) * GEta;
115 end
116
117 for i=21:3:24
118     N_edge(:,i) = 1/4 * (1 + zetaE(i) * zeta) * (1 - xi^2) * GEta;
119 end
120
121 for i=22:23
122     N_edge(:,i) = 1/4 * (1 + xiE(i) * xi) * (1 - zeta^2) * GEta;
123 end
124
125
126
127 % In zeta direction
128 for i = 25:32
129     N_edge(:,i) = 1/8 * (1 + xiE(i) * xi) * (1 + etaE(i) * eta) * ...
            (xiE(i)*xi + etaE(i)*eta + zetaE(i)*zeta - 1) * GZeta;
```

```
130 end
131
132 for i = 33:3:36
133     N_edge(:,i) = 1/4 * (1 - xi^2) * (1 + etaE(i) * eta) * GZeta;
134 end
135
136 for i = 34:35
137     N_edge(:,i) = 1/4 * (1 - eta^2) * (1 + xiE(i) * xi) * GZeta;
138 end
139
140
141 %% Computation of the curl of the edge functions
142
143 size_NE = size(NE);
144 for i=1:size_NE(2)
145     curl_NE_xi(i) = diff(NE(3,i), eta) - diff(NE(2,i), zeta);
146     curl_NE_eta(i) = diff(NE(1,i), zeta) - diff(NE(3,i), xi);
147     curl_NE_zeta(i) = diff(NE(2,i), xi) - diff(NE(1,i), eta);
148 end
149 % assembling the matrix
150 curlNE=J/(8*detJ)*[curl_NE_xi; curl_NE_eta; curl_NE_zeta]; ...
       %Remark 07/13/2018: The signs in curlNE are questionable. ...
       However, since N=curlN*sigma*curlN that does not affect the ...
       result.
151
152
153 numberofgausspoints = 5;
154
155 %% Computation of N-matrix
156
157 %% Computation of Nee
158 Nee0=curlNE.'*inv(sigma)*curlNE.*abs(detJ);
159
```

```
160 % Simpson quadrature through a custom function
161 Nee = TripleSimpsonsSymbolic(Nee0,-1, 1);
162
163 % Numerically evaluating the first integral
164 Nee1 = GaussInt(Nee0, xi, numberofgausspoints);
165 % Numerically evaluating  the second integral
166 Nee2 = GaussInt(Nee1, eta, numberofgausspoints);
167 % Numerically evaluating  the third integral
168 Nee = GaussInt(Nee2, zeta, numberofgausspoints);
169
170 savstr = sprintf("Nee_%d_Gauss.mat", numberofgausspoints);
171 save(savstr, 'Nee')
172 PrintMatrixToTxt(Nee,'Nee','TrifouNeeQuadLin.txt');
173
174
175
176 %% Computation of M matrix
177
178 %% Computation of Mee ("edge-edge part")
179 Mee0=mu*NE.'*NE.*abs(detJ);
180
181 % Simpson quadrature through a custom function
182 Mee = TripleSimpsonsSymbolic(Mee0,-1, 1);
183
184 % Gaussian quadrature
185 Mee1 = GaussInt(Mee0, xi, numberofgausspoints);
186 Mee2 = GaussInt(Mee1, eta, numberofgausspoints);
187 Mee = GaussInt(Mee2, zeta, numberofgausspoints);
188
189 savstr = sprintf("Mee_%d_Gauss.mat", numberofgausspoints);
190 save(savstr, 'Mee')
191 % Writing the equation with the custom writer
192 PrintMatrixToTxt(Mee,'Mee','TrifouMeeQuadLin.txt');
```

```
% Generating the matlab function through a built in matlab function
matlabFunction(Mee)


%% Computation of Mne ("node-edge part")
Mne0 = mu*NE.'*gradNN.*abs(detJ);

% Simpson quadrature through a custom function
Mne = TripleSimpsonsSymbolic(Mne0,-1, 1);

% Gaussian quadrature
Mne1 = GaussInt(Mne0, xi, numberofgausspoints);
Mne2 = GaussInt(Mne1, eta, numberofgausspoints);
Mne = GaussInt(Mne2, zeta, numberofgausspoints);

savstr = sprintf("Mne_%d_Gauss.mat", numberofgausspoints);
save(savstr, 'Mne');

% Writing the equation with the custom writer
PrintMatrixToTxt(Mne,'Mne','TrifouMneQuadLin.txt');
% Generating the matlab function through a built in matlab function
matlabFunction(Mne)

%% Computation of Mnn ("node-node part")
display('Mnn')
Mnn0 = mu*gradNN.'*gradNN.*abs(detJ);

% Simpson quadrature through a custom function
Mnn = TripleSimpsonsSymbolic(Mnn0,-1, 1);

% Gaussian quadrature
Mnn1 = GaussInt(Mnn0, xi, numberofgausspoints);
Mnn2 = GaussInt(Mnn1, eta, numberofgausspoints);
```

```
226 Mnn = GaussInt(Mnn2, zeta, numberofgausspoints);
227
228 savstr = sprintf("Mnn_%d_Gauss.mat", numberofgausspoints);
229 save(savstr, 'Mnn')
230
231 % Writing the equation with the custom writer
232 PrintMatrixToTxt(Mnn,'Mnn','TrifouMnnQuadLin.txt');
233 % Generating the matlab function through a built in matlab function
234 matlabFunction(Mnn)
```

Appendix F

The inner-product, in the H-matrix

In this appendix, the author will attempt to explain under what conditions the term containing the inner product in Eqn. F.0.1 is zero. Although this is established in many sources attempting to find a solution for this singular integration [5, 63, 61, 62, 68], it can also be reasoned from the equations.

$$H_e^a = \frac{1}{4\pi} \int_\Gamma \left(\int_\Gamma \frac{n_{\Omega_O}(\vec{x}) \cdot (\vec{y} - \vec{x})\, \zeta_a(\vec{y}) \vec{N}_e(\vec{x})}{||\vec{y} - \vec{x}||^3} \, d\vec{x} \right) d\vec{y} \tag{F.0.1}$$

From here on out, only the inside of the integral shall be considered. For the sake of simplicity, the $\zeta_a(\vec{y})\vec{N}_e(\vec{x})$ term is omitted, see Eqn. F.0.2. The normal vector is rewritten as $\hat{n}_b$

$$H_{int} = \frac{(\hat{n}_b \cdot (\vec{y} - \vec{x}))}{\vec{r}_{xy}^3} \tag{F.0.2}$$

There seems to be a misconception that the numerator is zero when the two discretized surfaces over which the integrals are evaluated are parallel. This is false since, by definition of the dot product, the dot product is zero if and only if the vectors over which the dot product is taken are orthogonal. Instead, the numerator is zero when the surfaces are co-planar. To illustrate, let us assume that the two surfaces are parallel, as in Figure F.1.

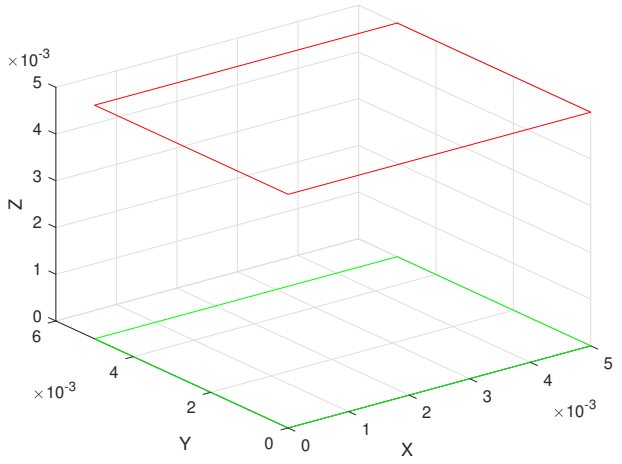

Figure F.1: The example two quadrilateral surfaces

In this case, the vector $\hat{n}_b$, describing the unit normal vector of one of the surfaces, can not possibly be orthogonal to the vector $(\vec{y} - \vec{x})$. The normal vector of the above surface is aligned with the z-axis, see the blue arrow in Figure F.2.

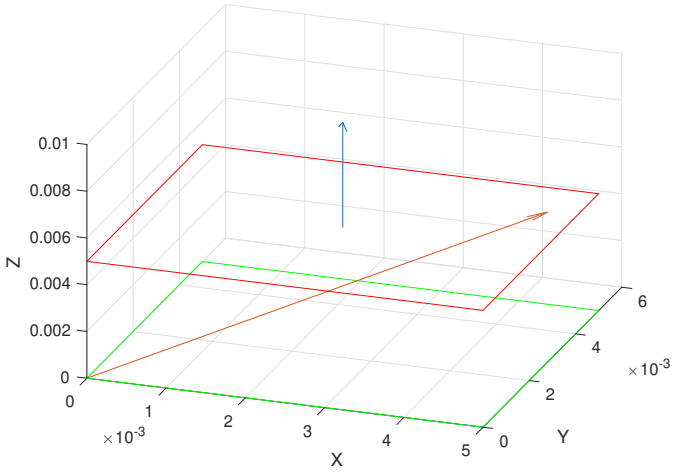

Figure F.2: Two quadrilateral surfaces with the vectors of the numerator

The vector $(\vec{y} - \vec{x})$, is from any point in the top surface to any point in the bottom surface. An example vector is depicted by the orange arrow in Figure F.2. In the current configuration of the surfaces, the two vectors can never become orthogonal.

The vectors can only be orthogonal if and only if the two surface elements are in the same plane, see Figure F.3.

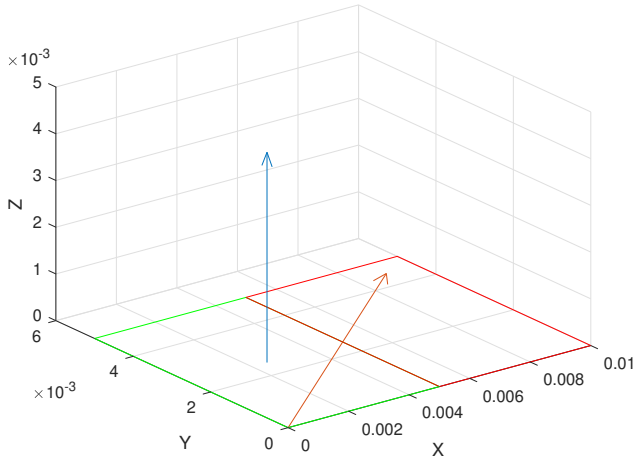

Figure F.3: The two quadrilateral surfaces

If the two surface elements are in the same plane, the vector $\hat{n}_b$ and vector $(\vec{y} - \vec{x})$ are always orthogonal. Hence, the correct way to check if the term $\hat{n}_b \cdot (\vec{y} - \vec{x})$ is zero is by checking if the two surface elements are co-planar. This can be done by calculating the volume of a tetrahedral made of three nodes of the first quadrilateral and one node of the second quadrilateral. If the volume of the described tetrahedral is zero, then the two surfaces are co-planar, thus the two vectors $\hat{n}_b$ and $(\vec{y} - \vec{x})$ are orthogonal and thus the term $\hat{n}_b \cdot (\vec{y} - \vec{x})$ is zero.